ACTIVE FLUTTER SUPPRESSION OF A SMART FIN

A THESIS SUBMITTED TO
THE GRADUATE SCHOOL OF NATURAL AND APPLIED SCIENCES
OF
MIDDLE EAST TECHNICAL UNIVERSITY

BY

FATİH MUTLU KARADAL

IN PARTIAL FULFILLMENT OF THE REQUIREMENTS
FOR
THE DEGREE OF MASTER OF SCIENCE
IN
AEROSPACE ENGINEERING

SEPTEMBER 2008

Approval of the thesis:

ACTIVE FLUTTER SUPPRESSION OF A SMART FIN

submitted by **FATİH MUTLU KARADAL** in partial fulfillment of the requirements for the degree of **Master of Science in Aerospace Engineering Department, Middle East Technical University** by,

Prof. Dr. Canan Özgen _____
Dean, Graduate School of **Natural and Applied Sciences**

Prof. Dr. İsmail Hakkı Tuncer _____
Head of Department, **Aerospace Engineering**

Prof. Dr. Yavuz Yaman
Supervisor, **Aerospace Engineering Dept., METU** _____

Examining Committee Members:

Assist. Prof. Dr. Melin Şahin _____
Aerospace Engineering Dept., METU

Prof. Dr. Yavuz Yaman _____
Aerospace Engineering Dept., METU

Dr. Güçlü Seber _____
Aerospace Engineering Dept., METU

Dr. Volkan Nalbantoğlu _____
Design Leader, ASELSAN

Assoc. Prof. Dr. Metin U. Salamcı _____
Mechanical Engineering Dept., Gazi University

Date: 01.09.2008

I hereby declare that all information in this document has been obtained and presented in accordance with academic rules and ethical conduct. I also declare that, as required by these rules and conduct, I have fully cited and referenced all material and results that are not original to this work.

Name, Last name : Fatih Mutlu Karadal

Signature :

ABSTRACT

ACTIVE FLUTTER SUPPRESSION OF A SMART FIN

Karadal, Fatih Mutlu
M.S., Department of Aerospace Engineering
Supervisor: Prof. Dr. Yavuz Yaman

September 2008, 112 pages

This study presents the theoretical analysis of an active flutter suppression methodology applied to a smart fin. The smart fin consists of a cantilever aluminum plate-like structure with surface bonded piezoelectric (PZT, Lead- Zirconate-Titanate) patches.

A thermal analogy method for the purpose of modeling of piezoelectric actuators in MSC®/NASTRAN based on the analogy between thermal strains and piezoelectric strains was presented. The results obtained by the thermal analogy were compared with the reference results and very good agreement was observed.

The unsteady aerodynamic loads acting on the structure were calculated by using a linear two-dimensional Doublet-Lattice Method available in MSC®/NASTRAN. These aerodynamic loads were approximated as rational functions of the Laplace variable by using one of the aerodynamic approximation schemes, Roger's approximation, with least-squares method. These approximated aerodynamic loads together with the structural matrices obtained by the finite element method were used to develop the aeroelastic equations of motion of the smart fin in state-space form.

The H_∞ robust controllers were then designed for the state-space aeroelastic model of the smart fin by considering both SISO (Single-Input Single-Output) and MIMO (Multi-Input Multi-Output) system models. The verification studies of the controllers showed satisfactory flutter suppression performance around the flutter point and a significant improvement in the flutter speed of the smart fin was also observed.

Keywords: Flutter suppression, thermal analogy method, unsteady aerodynamic modeling, H_∞ controller design, smart structures.

ÖZ

AKILLI BİR FİNİN AKTİF ÇIRPINMA KONTROLÜ

Karadal, Fatih Mutlu
Yüksek Lisans, Havacılık ve Uzay Mühendisliği Bölümü
Tez Yöneticisi: Prof. Dr. Yavuz Yaman

Eylül 2008, 112 sayfa

Bu çalışmada, aktif kontrol ile akıllı bir fin için çırpınmanın bastırılmasının teorik incelenmesi sunulmuştur. Akıllı fin, bir ucu tutturulmuş, diğer ucu serbest pasif alüminyum fin ve bunun her iki yüzeyine simetrik olarak yapıştırılmış piezoelektrik (PZT, Lead-Zirconate-Titanatee) yamalardan oluşmaktadır.

Piezoelektrik uyarıcıları MSC®/NASTRAN' da modellemek amacıyla, termal gerinimlerle piezoelektrik gerinimler arasında benzetim kurmaya dayanan termal benzetim yöntemi sunulmuştur. Termal benzetimle elde edilen sonuçlar, referans sonuçları ile karşılaştırılmış ve sonuçların birbirleriyle son derece uyumlu olduğu gözlemlenmiştir.

Akıllı fin üzerine etkiyen düzensiz aerodinamik yükler, MSC®/NASTRAN programı ile doğrusal iki boyutlu Doublet-Lattice metodu kullanılarak hesaplanmıştır. Bu yükler Roger yaklaşımı ve en küçük kareler metodu ile Laplace tabanlı fonksiyonlar olarak ifade edilmiştir. Yaklaşık düzensiz aerodinamik yükler ve sonlu elemanlar metodu ile

elde edilen yapısal matrisler kullanılarak akıllı finin aeroelastik modelinin durum-uzay şeklinde ifadesi oluşturulmuştur.

Akıllı finin tek-girdili tek-çıktılı ve çok-girdili çok-çıktılı sistem modelleri için H_∞ tipi gürbüz kontrolcüler tasarlanmıştır. Tasarlanan kontrolcüler başarılı bir şekilde çırpınmayı bastırmışlar ve çırpınma zarfını önemli ölçüde iyileştirmişlerdir.

Anahtar kelimeler: Çırpınmanın bastırılması, termal benzetim metodu, düzensiz aerodinamik modellemesi, H_∞ denetçi tasarımı, akıllı yapılar.

To my mother.

ACKNOWLEDGEMENTS

I would like to express my deepest thanks and gratitude to my supervisor Prof. Dr. Yavuz Yaman, for his support, criticism and guidance throughout the study.

I also would like to thank Dr. Volkan Nalbantoğlu, Dr. Güçlü Seber and Dr. Melin Şahin for their continuous support, and helpful discussions. Their enlightening advices and suggestions have motivated me to introduce this study.

My grateful thanks are for all my friends, the academic and the administrative staff in the department, for their help, understandings and motivations throughout this study. I am also thankful to my colleagues and my chief Dr. Muvaffak Hasan in TAI for their support and understandings.

TÜBİTAK who partially supported this work is also gratefully acknowledged.

Finally, the greatest thanks go to my mother who supported and encouraged me throughout my whole life. It would never be possible without her patience and understanding.

TABLE OF CONTENTS

LIST OF TABLES

LIST OF FIGURES

LIST OF SYMBOLS

σ	Stress
ε	Strain
c	Elastic stiffness coefficient
e	Piezoelectric stress constant
$\overline{E}$	Electric field
d	Piezoelectric strain constant
V_i	Voltage applied to the inner electrodes of piezoelectric actuators
V_o	Voltage applied to the outer electrodes of piezoelectric actuators
α	Thermal expansion coefficient
ΔT	Temperature difference
ΔV	Voltage difference
E	Young modulus
G	Shear modulus
ν	Poisson's ratio
ρ	Density
$[M]$	Mass matrix
$[D]$	Damping matrix
$[K]$	Stiffness matrix
$\{x(t)\}$	Structural displacement vector
$\lfloor F_p \rfloor$	Unit piezoelectric voltage force transformation matrix
$\{u(t)\}$	Piezoelectric actuation voltage vector
L	Number of piezoelectric actuators
ξ	Structural damping ratio
$\{F_a(x(t))\}$	Aerodynamic force vector

ω	Oscillation frequency
q_∞	Free stream dynamic pressure
k	Reduced frequency
V_∞	Free stream velocity
M_∞	Free stream Mach number
b	Reference chord length
$[Q(ik)]$	Aerodynamic influence coefficient matrix
$[\phi]$	Modal matrix
$\{\zeta(i\omega)\}$	Modal displacement vector
$[\overline{M}]$	Modal mass matrix
$[\overline{D}]$	Modal damping matrix
$[\overline{K}]$	Modal stiffness matrix
$[\overline{Q}(ik)]$	Modal aerodynamic influence coefficient matrix
$[\overline{F}_p]$	Modal piezoelectric voltage force matrix
s	Laplace variable
$[\overline{Q}_{app}(ik)]$	Roger's approximation of the modal aerodynamic influence coefficient matrix
$[\overline{Q}_R(ik)]$	Real part of the modal aerodynamic influence coefficient matrix
$[\overline{Q}_I(ik)]$	Imaginary part of the modal aerodynamic influence coefficient matrix
n	Number of modes contributing the response
R	Number of sensors on the smart structure
$[A]$	System matrix
$[B]$	Input matrix
$[C]$	Output matrix
$\{y(t)\}$	Output vector
$[C_q]$	Displacement output matrix
$[C_v]$	Velocity output matrix

m	Density ratio
F_l	Lower linear fractional transformation
F_u	Upper linear fractional transformation
$\overline{\sigma}$	Largest singular value
δ	Scalar uncertainty
Δ	Full complex uncertainty
P	Nominal plant
$\widetilde{P}$	Perturbed plant
μ	Structured singular value
W_{per}	Performance weight
W_{add}	Additive uncertainty weight
W_{act}	Actuator weight
W_{noise}	Noise weight

Other parameters are clearly defined wherever applicable.

CHAPTER 1

INTRODUCTION

1.1 Background to the Study

There have been intensive efforts to understand the aeroelastic behavior of structures more accurately in order to avoid catastrophic structural failure due to excessive vibrations. Since current aircraft designs move toward lighter structures to improve the fuel efficiency and aircraft agility, various aeroelastic problems are likely to occur more frequently. In recent years, extensive research has been carried out to develop methodologies for controlling the aeroelastic behavior of structures.

Flutter suppression is one of the main objectives of the aeroelastic control. Flutter is a self-excited oscillation of a structure caused by the interaction of the aerodynamic, inertial and elastic characteristics of the components involved. At speeds below the flutter speed, oscillations will be damped. At the flutter speed, oscillations will persist with constant amplitude (zero damping). At speeds above the flutter speed, oscillations will cause the damage or destruction of the structure.

Active and passive control methods have been developed in the last three decades and applied to suppress flutter. Passive solutions such as increasing the structural stiffness, mass balancing or modifying geometry resulted in increased weight and cost, and decreased performance. Therefore, there is a considerable interest in developing active control methods that can be used in place of, or in combination with, the traditional passive methods. Active methods are proved to be more robust and can conveniently and effectively take uncertainties into account.

During the past 30 years, there has been considerable research to develop active flutter suppression concepts that use conventional leading and trailing edge aerodynamic control surfaces. Flutter is generally of a catastrophic nature; therefore a failure of the system could seriously affect flight safety. As a result, system redundancy, reliability, and maintainability are critical issues to be addressed. To a lesser extent, the control surface authority available to maneuver the aircraft with the simultaneous implementation of active flutter suppression is also a concern. To alleviate these concerns, alternatives to utilizing the aerodynamic control surfaces for active flutter suppression are being studied.

The application of smart structures in conjunction with the advance control techniques is one such concept. The smart structure can be defined as the one which can sense the external disturbance and respond to that with active control in real time to maintain the mission requirements. Smart structures consist of highly distributed active devices called smart materials and controller units. The smart materials are used as sensors and/or actuators which are either embedded in or attached to an existing passive structure. Such materials include piezoelectric materials, shape memory alloys, electro/magneto-strictive materials and electro/magneto-rheological fluids.

The most widely used smart materials are piezoelectric materials. Piezoelectricity is a property of materials that generate an electrical charge when the materials are subject to material strain, and conversely, piezoelectric materials deform when they are subjected to an electric field. The development of mechanical strain when subjected to the electric field can be utilized to actuate a structure. A local strain is produced in the structure, which induces forces and moments. By judicious arrangement of piezoelectric actuators, the correct reaction of the structure required to inhibit flutter can be produced.

1.2 Scope and Contents of the Study

The purpose of this thesis is to present the theoretical analysis of an active flutter suppression methodology applied to a smart fin. The smart fin consists of a cantilever aluminum plate-like structure with surface bonded piezoelectric (PZT, Lead- Zirconate-Titanate) patches. Since its shape looks like the typical vertical tail of an aircraft, it is called smart fin in the study. Fluttering vibrations of the smart fin are attenuated and the system is stabilized over a wide range of operating conditions.

Chapter 2 gives a literature survey about the smart structures and active aeroelastic control. Recent developments in the field of piezoelectric materials are explained and the work done on the structural modeling of smart structures is described. The work on unsteady aerodynamic modeling and the applications of smart structures in active aeroelastic control are also given.

Chapter 3 is devoted to the structural modeling of smart structures by using finite element method. MSC®/PATRAN and MSC®/NASTRAN package programs are used in the modeling and analysis. Different finite element based structural modeling techniques for smart structures are proposed. To simulate piezoelectric actuation in MSC®/NASTRAN, the thermal analogy method, which is based on the analogy between piezoelectric strain and thermally induced strain, is described and some validation results are presented to demonstrate the accuracy of this method. Finally, the structural model of the smart fin is given.

Chapter 4 describes the state-space representation of the aeroelastic model of the smart fin. Rational approximation of the unsteady aerodynamic loads in the Laplace domain is described. A state-space model for the smart structures under unsteady aerodynamic loading is constructed, and the open loop characteristics of the smart fin are investigated.

Chapter 5 is devoted to the design of H_∞-synthesized controllers for the active flutter suppression of the smart fin. In the design of the controllers, SISO (Single-Input Single-

Output) and MIMO (Multi-Input Multi-Output) system models are considered. This chapter also investigates the performances of the controllers in vibration suppression and the enhancement in the flutter boundary of the smart fin.

The general conclusions drawn from the study and the recommendations for the future work are given in Chapter 6.

1.3 Limitations of the Study

The main limitations of the study can be listed as follows:

- Nonlinear characteristics of piezoelectric actuators and their hysteresis effects are neglected.
- Unsteady aerodynamics are calculated by Doublet Lattice Method in MSC®/NASTRAN, and they are approximated by Roger's method.
- H_∞ controller design method is considered for control applications.

CHAPTER 2

LITERATURE SURVEY

2.1 Introduction

This chapter presents a literature survey on the use of smart structures in active aeroelastic control. The survey first details the advances and trends for the smart structures with piezoelectric materials. Then the work done on the structural modeling of smart structures is described. Finally the recent developments in the field of unsteady aerodynamic modeling and active aeroelastic control are explained.

2.2 Smart Structures with Piezoelectric Materials

Recent developments in the field of piezoelectric materials have encouraged many researchers to work in the field of smart structures. The piezoelectric materials can be used as sensors that recognize and measure the intensity of physical quantities such as strain in the structure and as such can be used as a structural health monitor to detect the possible damage. They can also be used as actuators, where be responding to an applied voltage, they strain, and cause the smart structure to deform, or in the dynamic case cause it to excite or dampen vibration oscillations [1].

Piezoelectricity was first demonstrated by Pierre and Jacques Curie in 1880. Their experiments led them to elaborate the early theory of piezoelectricity [2]. In 1894 Voigt rigorously stated the relationship between the material structure and the piezoelectric effects, namely that when a voltage is placed across a piezoelectric material, it generates

a geometric change known as a converse piezoelectric effect [1]. Depending on the material orientation and the poling direction, the material may elongate or shrink in different directions, or an angular distortion. The converse piezoelectric effect has been applied in actuators design. Also, with the same material if the material is stressed due to a tensile, compressive or shear load, an electrical current results, and this is called the direct piezoelectric effect. The direct piezoelectric effect has been widely used in transducers design (accelerometers, force and pressure transducers, etc.).

The primary piezoelectric materials in use are piezopolymers (e.g. Polyvinylidene Fluoride - PVDF) and piezoceramics (e.g. Lead Zirconate Titanate - PZT). However, since PVDF actuators and sensors have very low passive stiffness values and extreme sensitivities to environmental conditions such as humidity and temperature, they are not attractive for most of the engineering applications [3]. PZTs are widely used as actuator and sensor for a wide range of frequencies, including ultrasonic applications and they are well suited for high precision applications [2].

2.3 Structural Modeling of Smart Structures

Numerous studies have been completed on the structural modeling of smart structures with piezoelectric active devices. Considerable interest was focused on the modeling of smart structures using Euler-Bernoulli beam theory and Timoshenko beam theory with integrated piezoelectric layers in the past. Aldraihem *et al.* [4] was developed models for laminated beam-like components of smart structures using these two theories. In this work, comparison between the models was also presented to show the advantages and the limitations of each of the theories. Abramovich [5] was presented analytical formulation and closed form solutions of composite beams with piezoelectric actuators, which was based on Timoshenko beam theory. He also studied the effects of actuator location and number of patches on the actuator's performance for various configurations of the piezoelectric patches and boundary conditions under mechanical and/or electric loads. In addition to beam theories, in References [6,7], a scheme to model static and

dynamic responses of plates containing distributed piezoelectric elements utilizing the Kirchhoff thin plate theory was presented.

Since the early 1970s, many finite element models have been proposed for the analysis of piezoelectric structural elements. They were mainly devoted to the design of ultrasonic transducers [8,9]. By the late 1980s, interests have been directed towards applications in smart materials and smart structures. Tzou and Tseng [10] developed a finite element code incorporated with feedback control design to study the vibration suppression of a flexible shell structure with piezoelectric sensors and actuators. Ha *et al.* [11] established a finite element formulation based on an 8-node three-dimensional brick element for analyzing fiber reinforced laminated composites containing distributed piezoelectric ceramics. A finite-element model based on the classical laminated plate theory was developed for the active vibration control of a composite plate containing distributed piezoelectric sensors and actuators by Lam *et al.* [12]. Koko *et al.* [13] presented a 20-node piezoelectric element code, capable of designing independent modal-space control and state feedback control.

Due to the increasing interest in the design of complex smart structures with piezoelectric actuators and the need for fast and simple implementation of piezoelectric control systems, technology developers provide the tools to model smart structures. Some piezoelectric elements have become available in the commercial finite element programs such as ANSYS® and ABAQUS®. Yaman *et al.* [14] worked on the effectiveness of the finite element code ANSYS in the modeling of the smart structures. Hauch [15] investigated using ABAQUS electromechanical coupled finite elements and superelement capabilities for modeling structures with piezoelectric actuators.

For modeling piezoceramics, Freed and Babuska [16] described a simple thermal analogy approach, in which temperature-induced expansion is used to simulate voltage actuation. They also presented the integration of the approach into MSC®/NASTRAN, which offers no piezoelectric coupled-field elements. Dong and Meng [17] were investigated the dynamic response of a smart beam by using the thermal analogy with

MSC/NASTRAN and validated the thermal analogy method by comparing the results to the ones observed by experimentally and computed by the finite element method based on a piezoelectric formulation.

2.4 Unsteady Aerodynamic Modeling

The main difficulty in modeling an aeroelastic system lies in the representation of the unsteady aerodynamic loads. An important feature of these forces is the lag associated with the circulatory wake, where disturbances shed to the flow by the wing motion continue to affect the loads at a later time [18]. Theodorsen [19] employed a lift deficiency function in the reduced frequency domain to represent this effect for the oscillatory flow over an airfoil. R.T. Jones [20] first considered the aerodynamic forces on finite wings of elliptic planform in non-uniform motion in incompressible flow. The lift on rectangular and tapered wings for impulsive motion in incompressible flow was calculated by W.P. Jones [21].

Several techniques have been presented in the past for the calculation of unsteady aerodynamic loads for simple harmonically oscillating airfoils and lifting surfaces. Techniques of treating the singularities of the kernel function and obtaining solutions were given by Watkins *et al*. [22], and have been extended to wings with control surfaces by Cunningham [23]. Another calculation process, analogous to the finite element method of structures, is the doublet-lattice technique of Albano and Rodden [24].

In order to construct an aeroelastic model in state-space form, the air loads in the frequency domain have to be approximated in the Laplace domain using rational function approximations. There are several methods in the literature in order to approximate the unsteady generalized forces. The most widely used methods are those based on the least-squares method of Roger [25], the Matrix Pade method of Vepa [26] and the minimum state method of Karpel [27]. The resulting state-space equations from

these techniques include augmented states that represent the aerodynamic lags. The number of aerodynamic augmented states resulting from Vepa's and Roger's methods is equal to the number of the approximating denominator roots, multiplied by the number of vibration modes. In the minimum-state method, higher number of denominator roots is required and computationally heavier, iterative, nonlinear least-square solutions are used. However, the number of augmenting states resulting from this method is equal to the number of denominator roots, regardless of the number of modes. Thus, the resulting approximation yields a state-space model which has a relatively low number of states.

2.4 Active Aeroelastic Control

In recent years, applications of active control to aeroelastic systems have been studied in order to favorably modify the flutter, gust, buffet and maneuver load behavior of aeroelastic systems.

Control surfaces such as spoilers and flaps have been generally used to generate auxiliary aerodynamic lift and moment. The active flexible wing (AFW) program demonstrated flutter suppression of a fighter-type scaled model in various maneuver modes by utilizing control surfaces and active control technology at NASA Langley Research Center [28,29]. Vipperman *et al.* [30] developed a wind tunnel model of a typical section airfoil with a trailing edge flap and applied H_2- and μ–synthesized controls for active flutter suppression. They reported that μ–synthesized control provided significantly better disturbance rejection than H_2 controller, particularly when the aeroelastic pole migration is dominant. Barker *et al.* [31] introduced a control theory based on gain-scheduled Linear Fractional Transformation (LFT) for a wind tunnel wing model with a trailing edge flap and upper and lower surface spoilers. The control concept was implemented successfully for a wide range of operating conditions to achieve vibration attenuation. A comparative study was also made on an optimized linear controller with LFT based control scheme and it was seen that the gain-scheduled controller outperforms the linear controller throughout the operating region.

Recent development of smart structures gives us another alternative for active aeroelastic control. The augmentation or replacement of conventional aerodynamic control surfaces with strain actuation for aeroelastic control was the focus of an analytical investigation of a typical section by Lazarus *et al.* [32]. They found that strain actuation by means of piezoelectric elements may provide a viable and effective alternative to articulated control surfaces for controlling aeroelastic response.

As part of the Actively Controlled Response of Buffet-Affected Tails (ACROBAT) program at NASA Langley Research Center, Moses [33,34] conducted wind tunnel experiments on a 1/6 scale model of the F/A-18 aircraft. The starboard vertical tail was equipped with an active rudder and the port vertical tail was equipped with piezoelectric actuators. By using single-input-single-output control law, the power spectral density of the root strains at the frequency of the first bending mode of the vertical tail was reduced by up to 60%. In another study, an active smart material control system, using distributed piezoelectric actuators, was presented for buffet alleviation by Sheta et al. [35]. In this work, a computational investigation of active control of the vertical tail buffeting of full-scale model of the F/A-18 aircraft over wide range of angles of attack was conducted and presented. These studies had shown that the actively controlled piezoelectric actuators are effective for buffet alleviation.

Suleman *et al.* [36] proposed the effectiveness of the piezoceramic sensor and actuators on the suppression of vibrations on an experimental wing due to the gust loading. They showed, experimentally, the feasibility of the application of the smart structures in the suppression of vibrations due to the gust loading on the smart wing. Fazelzadeh *et al.* [37] successfully applied an active optimal integral/feedforward control for a supersonic panel under gust disturbance effects with piezoelectric actuators. The effectiveness of the designed optimal controller for different piezoelectric actuator configurations was also demonstrated.

An analytical and experimental investigation of flutter suppression of a fixed wing by piezoelectric actuators was performed by Heeg [38] with the corresponding

experimental studies performed at NASA Langley Research Center under the Piezoceramic Aeroelastic Response Tailoring Investigation (PARTI) program. Experimental results indicated significant flutter suppression was achieved. Döngi *et al.* [39] presented a finite element method based on numerical solution for flutter suppression of adaptive panel with self-sensing piezoelectric actuators in high supersonic flow. A control approach based on output feedback using collocated piezoelectric actuators was introduced with a simple analog circuit.

In one of the recent studies, Han *et al.* [40] presented a numerical and experimental investigation on active flutter suppression of a swept-back lifting surface using piezoelectric actuation. They constructed the aeroelastic model by using a finite element method, a panel aerodynamic method and the minimum state-space realization, and grouped the piezoelectric actuators optimally by using genetic algorithms to enhance controllability. H_2- and μ–synthesized robust control laws were designed for flutter suppression and the performances of the two control methods were compared. They reported that μ–synthesized controller showed improved behavior over a wide flow speed range.

CHAPTER 3

STRUCTURAL MODELING OF SMART STRUCTURES

3.1 Introduction

This chapter is devoted to the details of the structural modeling of smart structures by using finite element method. MSC®/PATRAN and MSC®/NASTRAN package programs are used in the modeling and analysis. Firstly, theory of piezoelectricity is introduced and governing equations of motion for smart structures are given. Then, in order to represent the different finite element based structural modeling techniques for smart structures, three finite element models are proposed for a smart beam and the influences of different finite element types are investigated.

Since MSC®/NASTRAN offers no piezoelectric coupled-field elements capability to model the smart structures directly; the analogy between piezoelectric strain and thermally induced strain, called thermal analogy method, is used to allow temperature changes to model piezoelectric voltage actuation. An overview of the governing equations applied to the thermal analogy and ways to implement it into MSC®/NASTRAN are described. Thereafter, some validation results are presented to demonstrate the accuracy of the thermal analogy method and the method is then used to predict the static response of the smart beam. Finally, structural model of the smart fin, which is the model used for the active flutter suppression in this thesis, is given.

3.2 Theory of Piezoelectricity

Inverse piezoelectricity effect is the property exhibited by anisotropic crystals which develops mechanical strains proportional to the electrical charges when subjected to an external electrical field. Figure 3.1 shows the material and the principal axes (x, y, z) and (1, 2, 3), respectively, and also the direction of polarization (z-axis) for a piezoelectric material. Actuation voltages applied to inner and outer electrodes of the piezoelectric material are represented by V_i and V_o, respectively.

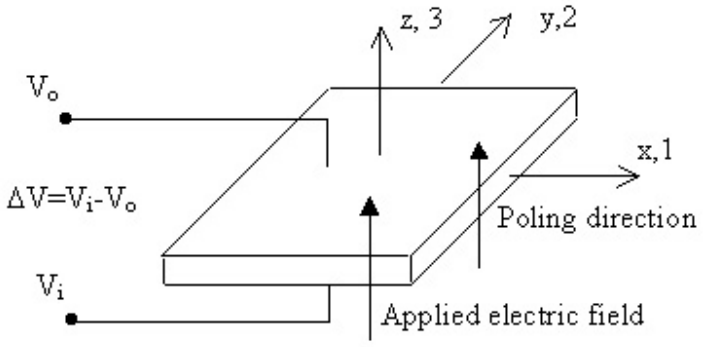

Figure 3.1 A typical piezoelectric patch

The three-dimensional linear piezoelectric equations for the inverse piezoelectric effect can be expressed by the following equation [41]:

$$\{\sigma\} = \left[c^E\right]\{\varepsilon\} - [e]^T \{\overline{E}\} \tag{3.1}$$

where $\{\sigma\}$ is the 6×1 stress vector, $\{\varepsilon\}$ is the 6×1 strain vector, $\{\overline{E}\}$ is the 3×1 electric field vector, $\left[c^E\right]$ is the 6×6 elastic stiffness coefficient matrix in constant electric field and $[e]$ is the 3×6 piezoelectric stress constant matrix. The superscript "*T*" denotes the transpose of a matrix. Equation (3.1) characterizes the inverse piezoelectric effect that enables piezoelectric materials to function as actuators.

Piezoelectric material manufacturers usually provide the strain-charge form of the 3×6 piezoelectric strain matrix $[d]$. This matrix accounts for the piezoelectric effect, *i.e.*, the coupling between mechanical and electric field. The relation between $[e]$ and $[d]$ can be given as follows:

$$[e]^T = [c^E][d]^T \tag{3.2}$$

For many piezoelectric material types, the polarization axis is aligned with the z-axis, or 3-axis. This provides symmetric hexagonal crystallographic structure and the elastic stiffness coefficient matrix and the piezoelectric strain coefficient matrix can be written as:

$$[c^E] = \begin{bmatrix} c_{11}^E & c_{12}^E & c_{13}^E & 0 & 0 & 0 \\ c_{12}^E & c_{11}^E & c_{13}^E & 0 & 0 & 0 \\ c_{13}^E & c_{13}^E & c_{33}^E & 0 & 0 & 0 \\ 0 & 0 & 0 & c_{44}^E & 0 & 0 \\ 0 & 0 & 0 & 0 & c_{44}^E & 0 \\ 0 & 0 & 0 & 0 & 0 & c_{66}^E \end{bmatrix} \tag{3.3}$$

$$[d] = \begin{bmatrix} 0 & 0 & 0 & 0 & d_{15} & 0 \\ 0 & 0 & 0 & d_{24} & 0 & 0 \\ d_{31} & d_{32} & d_{33} & 0 & 0 & 0 \end{bmatrix} \tag{3.4}$$

3.3 Governing Equation of Motion for Smart Structures

The finite element method can effectively be used in the modeling of smart structures. By applying the finite element procedure, the governing equation of motion for a smart structure subjected to the piezoelectric actuation can be represented as [42,43]

$$[M]\{\ddot{x}(t)\}+[D]\{\dot{x}(t)\}+[K]\{x(t)\}=\lfloor F_p \rfloor\{u(t)\} \tag{3.5}$$

here, by defining *Ndof* as the total number of degrees of freedom of the finite element model, $[M]$, $[D]$ and $[K]$ denote $Ndof \times Ndof$ global mass, damping and stiffness matrices, respectively. $\{x(t)\}$ is the structural displacement vector of size $Ndof \times 1$. Defining L as the number of piezoelectric actuators, $\lfloor F_p \rfloor_{Ndof \times j}$ is the unit piezoelectric voltage force transformation matrix from jth (j=1 to L) actuator and $\{u(t)\}_{j\times 1}$ is the piezoelectric actuation voltage vector associated with the jth piezoelectric actuator. $\lfloor F_p \rfloor$ specifies the actuation characteristics of PZT actuators and depends on the types of actuators, their location on the structure and their electromechanical properties. It should be noted that aerodynamic and other disturbance forces are not included in Equation (3.5).

3.4 Different Finite Element Based Structural Modeling Techniques for Smart Structures

This section presents structural modeling techniques for smart structures using finite element method with MSC®/PATRAN. Different finite element models of a smart beam are proposed and the influences of finite element types are investigated. The smart beam considered in this study is composed of an aluminum beam modeled in cantilevered configuration with eight surface bonded SensorTech BM500 type [44] piezoelectric patches. The smart beam model is given in Figure 3.2. The material properties of the

aluminum beam are: E = 69 GPa, $\nu = 0.33$ and $\rho = 2710$ kg/m^3. The electromechanical properties of the BM500 are given in Appendix A.

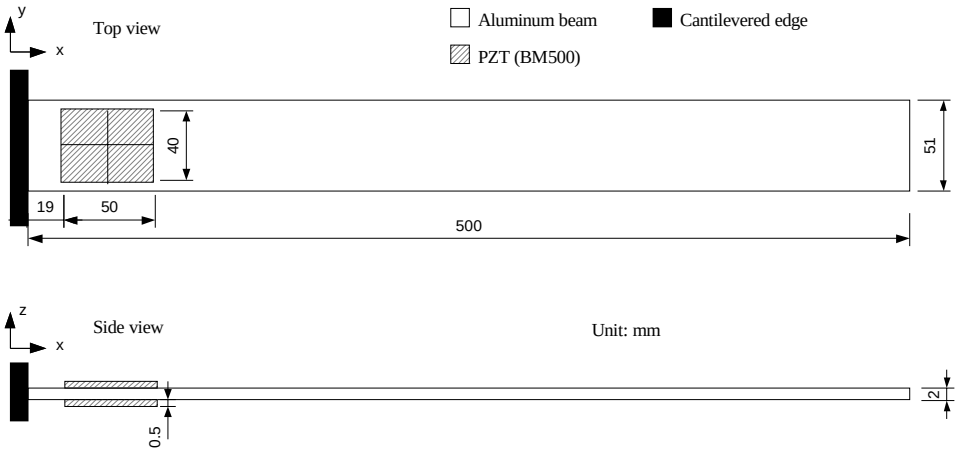

Figure 3.2 The smart beam used in the study

The smart beam is modeled by considering three approaches and natural frequencies of the models are examined and compared with the experimental results.

In the first approach, both piezoelectric patches and aluminum beam are modeled by CHEXA type solid elements. This model is called ‘solid-solid model’ and shown in Figure 3.3. The model consists of 1628 nodes and 808 CHEXA solid elements with eight grid points.

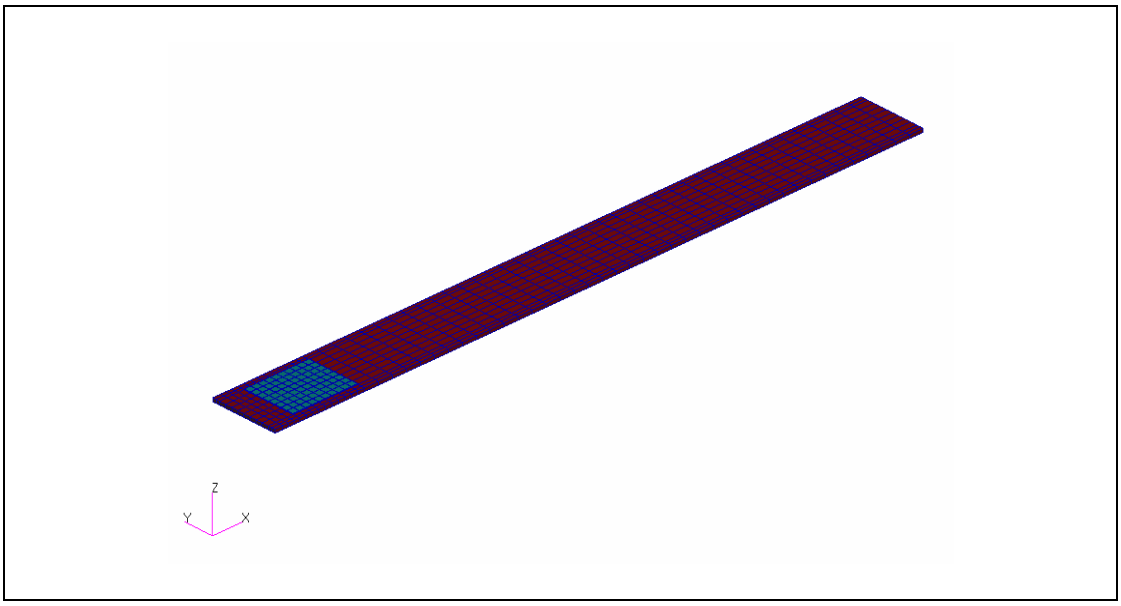

Figure 3.3 Solid-solid finite element model of the smart beam with 1628 nodes and 808 CHEXA elements

In order to improve the computational efficiency and alleviate the stiff behavior of ordinary three-dimensional solid elements, the plate structures are usually modeled by flat-shell elements. For this reason, as a second approach, the piezoelectric patches and the part of the aluminum beam between the patches are modeled by 100 eight-node CHEXA type solid elements; the remaining part of the beam is modeled by 132 four-node CQUAD4 type shell elements. This model is denoted by 'solid-shell' model and is given in Figure 3.4. In this model, solid and shell elements are connected to each other by MSC®/NASTRAN multipoint constraint type shell-to-solid element connector, RSSCON. RSSCON connects the three translational degrees of freedom and the two rotational degrees of freedom of the shell node to the three translational degrees of freedom of the upper and lower solid edge nodes [45]. Figure 3.5 shows the detailed modeling near the piezoelectric elements.

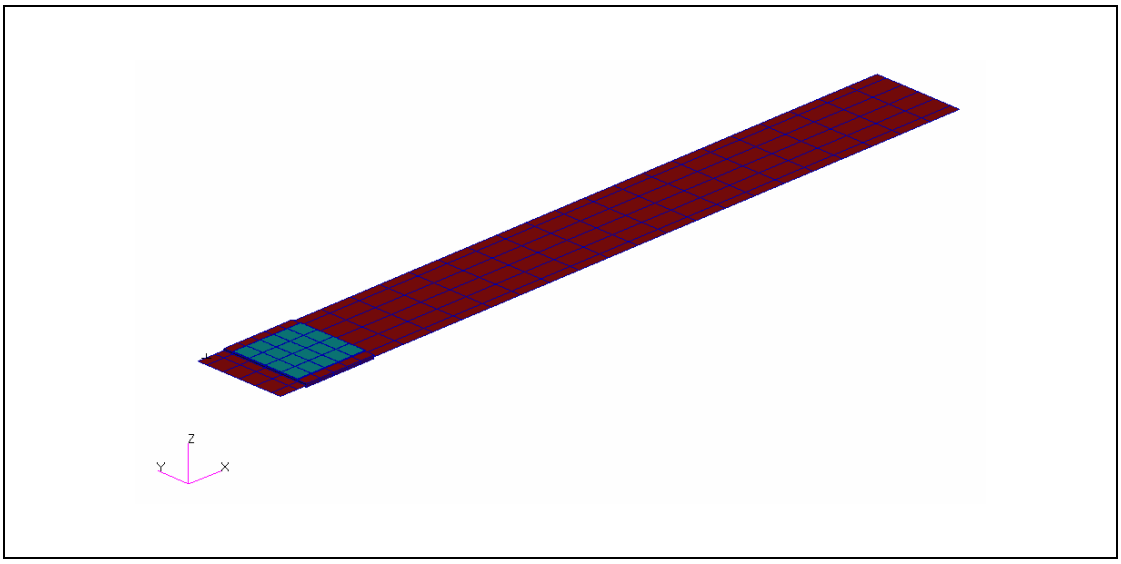

Figure 3.4 Solid-shell finite element model of the smart beam with 340 nodes and 132 CQUAD4 and 100 CHEXA elements

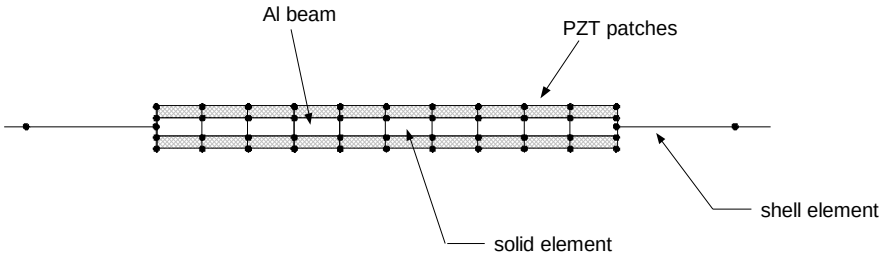

Figure 3.5 The detailed modeling near the piezoelectric patches for the solid-shell model of the smart beam

In the third approach, both piezoelectric patches and aluminum beam are modeled by CQUAD4 type shell elements. The connection between the piezoelectric patches and the aluminum beam shell elements is provided by rigid bar elements, RBAR's. Since RBAR's are connected together, there exist independent and dependent degrees of

freedom on nodes connected by RBAR's. The nodes on the aluminum beam mid-layer have the independent degrees of freedom and all the nodes on the piezoelectric layers have the dependent degrees of freedom. This model can be called 'shell-shell model'. Finite element model of the smart beam and the detailed modeling near the piezoelectric patches can be seen in Figure 3.6 and Figure 3.7, respectively. This modeling technique can be used when the passive portion of the smart structure is composite and/or the piezoelectric patches are composed of several layers; since composite structures are usually modeled by plate-like two dimensional elements in MSC®/NASTRAN.

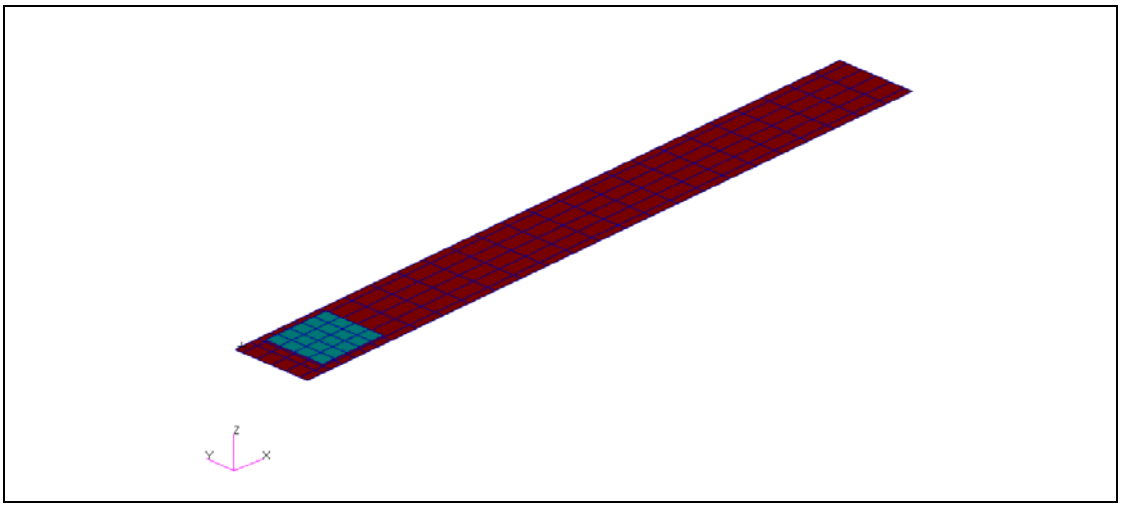

Figure 3.6 Shell-shell finite element model of the smart beam
with 256 nodes and 202 CQUAD4 and 60 RBAR elements

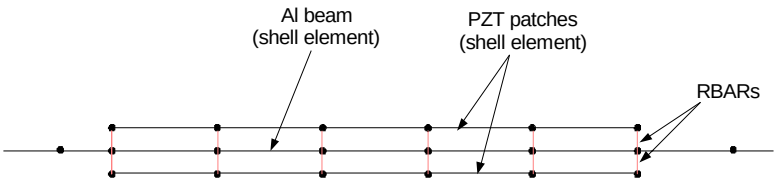

Figure 3.7 The detailed modeling near the piezoelectric patches for the shell-shell model of the smart beam

For the smart beam models developed, the normal modes analyses of MSC®/NASTRAN are performed. The first three natural frequencies for the smart beam models are examined and compared with the available experimental results [43]. Table 3.1 gives the comparison of the natural frequencies. It can be seen from Table 3.1 that, the natural frequency results for the finite element models are close to each other and especially for the first mode, are in a very good agreement with the experimental frequency. The difference between the theoretical and the experimental results is mainly due to the tendency of the finite element analysis to overestimate the natural frequencies and also due to the dispersion error caused by discretization at higher modes; usually more refined meshes are needed to get good accuracy [46].

Table 3.1 Theoretical and experimental frequencies [Hz] of the smart beam

Mode number	Solid-solid model Natural Frequencies	Solid-shell model Natural Frequencies	Shell-shell model Natural Frequencies	Experimental Resonance Frequencies [43]
1	7.31	7.30	7.33	7.29
2	43.55	43.44	43.56	40.07
3	117.12	116.76	116.86	110.62

3.5 Thermal Analogy Method

Thermoelastic constitutive equation with the generalized Hooke's law, taking into account the thermal effect, can be written as follows:

$$\{\sigma\} = [c]\{\varepsilon\} - [c]\{\alpha\}\Delta T \tag{3.6}$$

where $\{\alpha\}$ is a 6×1 thermal expansion coefficient vector and $\Delta T = T - T_0$ is a temperature difference, relative to a reference temperature T_0.

Combining piezoelectric equations (3.1) and (3.2) and comparing with equation (3.6), the piezoelectric strains and thermal strains relationship can be obtained as follows:

$$[d]^T \{\overline{E}\} = \{\alpha\}\Delta T \tag{3.7}$$

For the extension actuation mechanism of piezoelectric materials, the electric field and poling direction are along the piezoelectric layer thickness, hence $\overline{E}_1$ and $\overline{E}_2$ can be taken as zero. Also assuming the variation of electrical potential is to be linear in the thickness of a piezoelectric layer (constant electric field), $\overline{E}_3 = \Delta V_3 / t$, equation (3.7) is reduced to:

$$\begin{bmatrix} d_{31} & d_{32} & d_{33} & 0 & 0 & 0 \end{bmatrix}^T \frac{\Delta V_3}{t} = \begin{bmatrix} \alpha_{11} & \alpha_{22} & \alpha_{33} & 0 & 0 & 0 \end{bmatrix}^T \Delta T \tag{3.8}$$

where ΔV_3 represents the voltage difference between the electrodes and t is the thickness of the piezoelectric actuator.

From equation (3.8) the relation between piezoelectric strains and thermal strains is obtained as:

$$\alpha_{11} = \frac{d_{31}}{t}, \quad \alpha_{22} = \frac{d_{32}}{t}, \quad \alpha_{33} = \frac{d_{33}}{t}$$

$$\Delta T = \Delta V_3 \tag{3.9}$$

To simulate the voltage actuation, thermal expansion coefficients are imposed as piezoelectric strain coefficients divided by thickness and temperature change is imposed equal to the applied voltage. Equation (3.9) indicates that the voltage actuation of a piezoelectric actuator can be simulated exactly by using the conventional three-dimensional elastic elements with the thermal actuation rather than directly utilizing piezoelectric elements, which are not currently available in MSC®/NASTRAN.

It should be noted that since the thermal effect is not reciprocal quantity (*i.e.* temperature produces strains but strains do not produce temperature), only the inverse effect of linear piezoelectricity can be modeled by the thermal analogy method. It means that the piezoelectric element can only act as an actuator but not as a sensor.

3.5.1 Implementation of the Thermal Analogy in MSC®/NASTRAN

Modeling the voltage actuation of a piezoceramic based on the thermal analogy method can easily be performed in MSC®/NASTRAN via the CHEXA element card and the MAT9 material properties card. The MAT9 card describes anisotropic materials for solid elements and allows the application of six different thermal expansion coefficients. The required thermal expansion coefficients can be calculated from equation (3.9).

The voltage actuation can be performed directly by applying a corresponding temperature, as described in the previous section, on the piezoelectric nodes with the TEMP cards. TEMP cards identify the locations at which thermal loads (voltage) are applied. Moreover, TEMPD card must also be used to set the temperature of non-piezoelectric nodes to 0 to ensure thermal loads are generated only at the piezoelectric actuator locations.

3.5.2 Numerical Validation of the Thermal Analogy Modeling Approach

In order to validate the thermal analogy modeling approach in MSC®/NASTRAN, two test cases, developed by three-dimensional piezoelectric finite element formulation, are selected and the static and dynamic results are compared with the MSC®/NASTRAN thermal analogy results. For the purpose of comparing the results under a static loading, a composite plate with PZT actuators placed at the top and bottom surfaces of the plate from Lim et al. [47] is chosen as the test case. The displacement fields obtained from the static analysis by thermal analogy method are compared with this reference model. For the dynamic analysis, a piezoelectric actuator bonded to an elastic beam developed by Cote et al. [48] is chosen as the test case and the velocity results are compared.

Static Analysis:

The model on which static analysis performed is a simply supported composite plate composed of $[0/90/0]_{sym}$ graphite/epoxy layers with PZT actuators placed at the top and bottom surfaces of the plate. Figure 3.8 represents the model. The poling directions of the two PZT wafers are opposite, so that the PZTs can produce a bending moment. Initially, 200 N/m^2 pressure is prescribed over the plate and an electric field is applied such that the plate recovers its original shape.

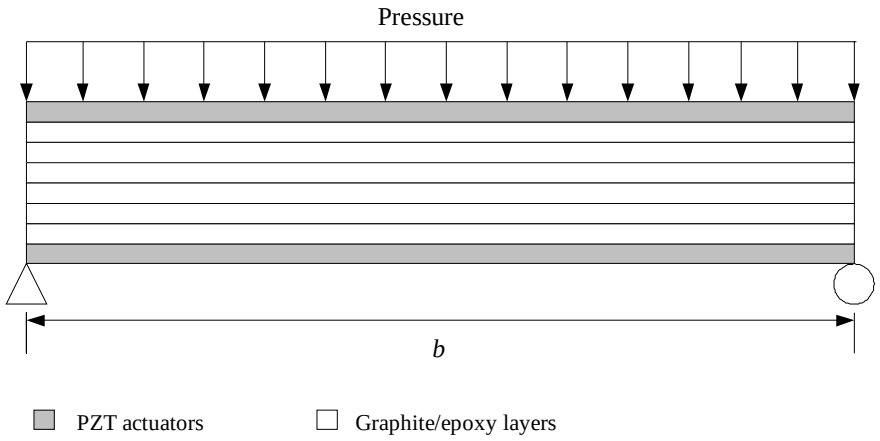

Figure 3.8 Reference model for static analysis: A simply supported composite plate with PZT layers

The thickness of PZT layers is 0.254 mm and the thickness of each graphite/epoxy layer is 0.138 mm. Material properties of the PZT and the graphite/epoxy are summarized in Table 3.2.

Table 3.2 Material properties of PZT G1195 and graphite/epoxy

Properties	PZT G1195 Piezoceramic	T300/976 Graphite/epoxy
E_{11} (GPa)	63	150
E_{22} (GPa)	63	9
ν_{12}	0.3	0.3
G_{12} (GPa)	24.2	7.1
d_{31} (10^{-10} m/V)	2.54	-
d_{32} (10^{-10} m/V)	2.54	-

Finite element model of the composite plate is constructed by shell-shell modeling approach using the package program MSC®/PATRAN. Isotropic material properties are assumed for the piezoelectric layers (MAT9 card is not used) and the equivalent thermal expansion coefficients are calculated from equation (3.9). Finite element model consists of 867 nodes, 768 CQUAD4 plate elements and 578 RBAR rigid elements. PZT actuators and the composite plate are modeled by CQUAD4 elements and the bonding between PZT layers and the plate is provided by RBAR elements. MSC®/NASTRAN linear static solution is performed for 15V and 27V actuations to the PZT layers and 200 $N.m^2$ pressure over the plate. Voltage actuation is simulated by applying temperature differences of $\Delta T = 15^o C$ and $\Delta T = 27^o C$ to the nodes of the piezoelectric layers with TEMP cards. TEMPD card is used in order not to generate thermal loads at the non-piezoelectric nodes.

Figure 3.9 shows the deformed shapes of the plate after applying 200 N/m^2 pressure over the plate and applying 15 or 27V to the PZT layers. Figure 3.10 shows the displacement of the plate along its centerline for 0, 15, and 27V after applying the pressure. In Figure 3.10, MSC®/NASTRAN thermal analogy results are given with the reference model results obtained by three-dimensional piezoelectric finite element formulation consisting of 18-node assumed strain piezo-solid elements [47]. It can be seen that the results obtained by MSC®/NASTRAN with the thermal analogy are very close to the results obtained by three-dimensional piezoelectric finite element formulation. This numerical test confirms that the thermal analogy provides satisfactory results.

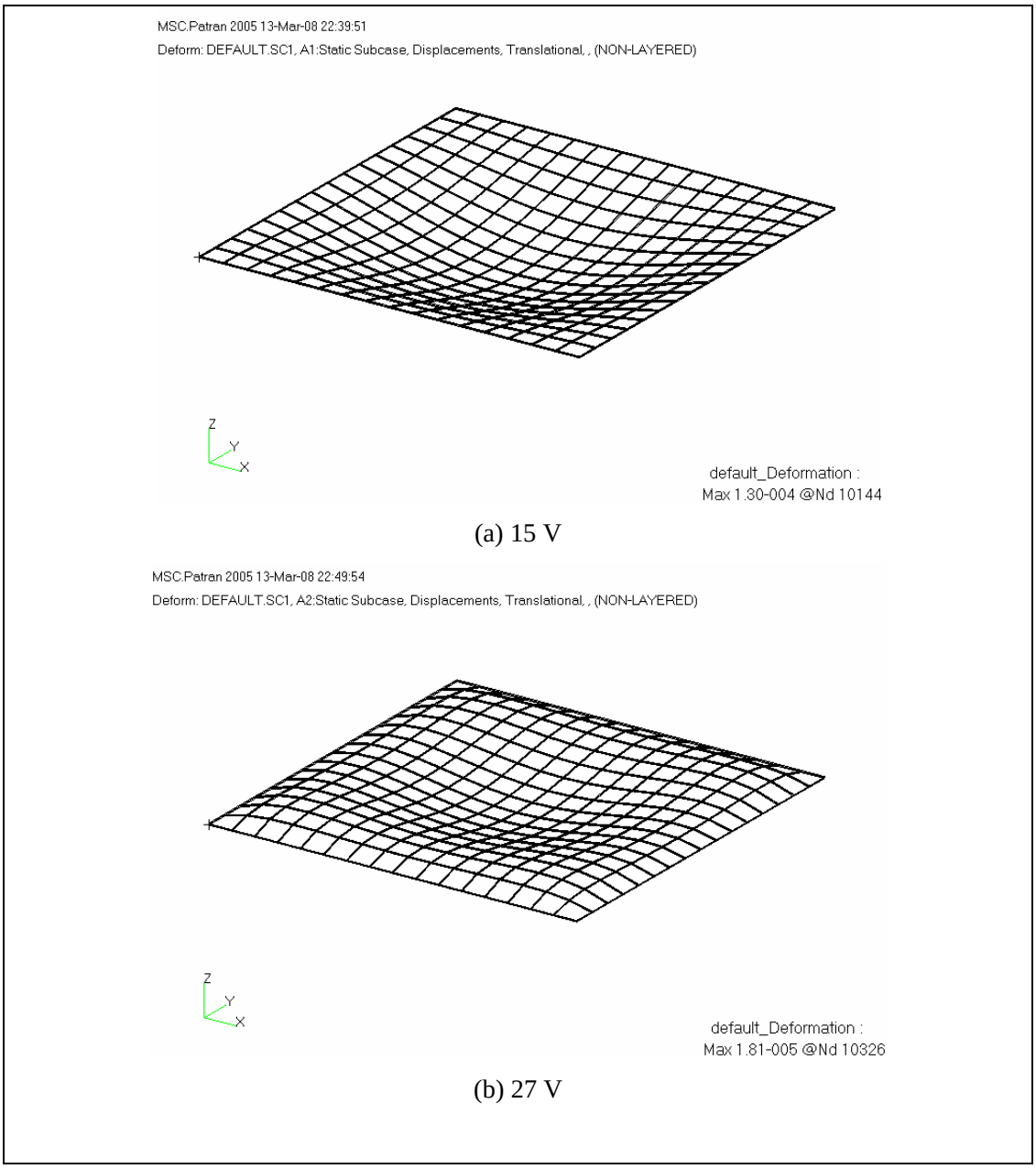

Figure 3.9 Deformed shape of the composite plate with PZT actuators under 200 N/m^2 pressure and piezoelectric actuation of (a) 15 V and (b) 27 V

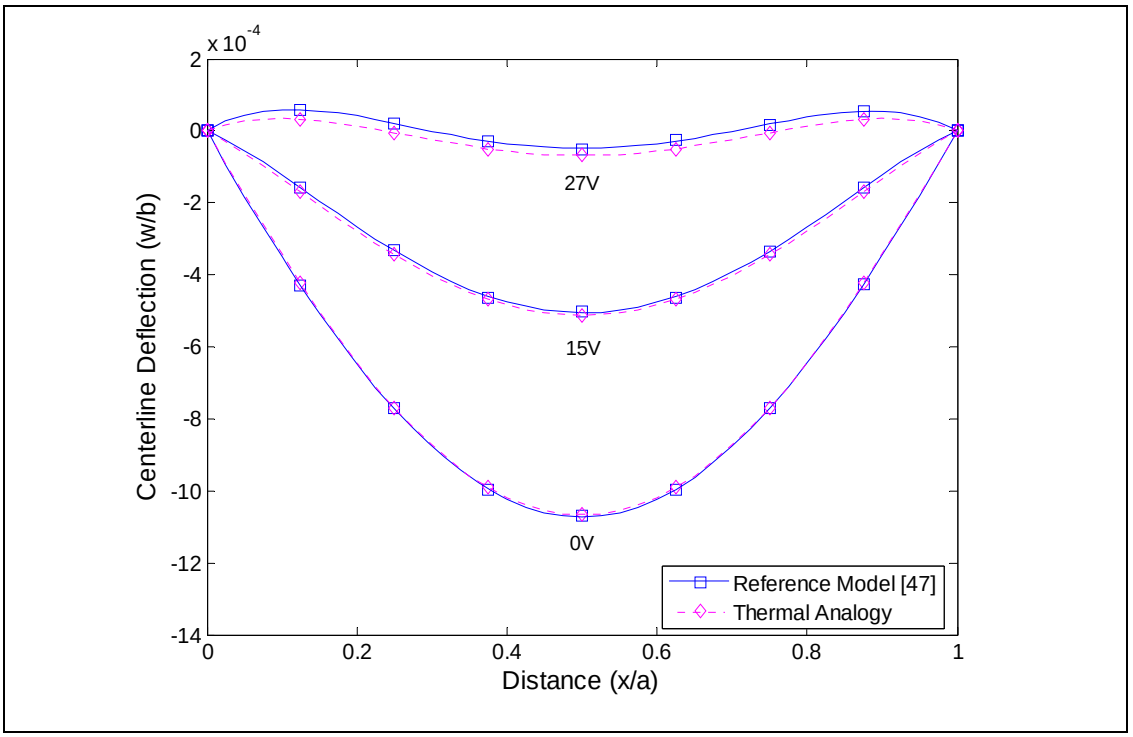

Figure 3.10 Deflection of the composite plate with PZT actuators along the centerline

Dynamic Analysis:

In order to assess the dynamic results obtained with the thermal analogy implemented in MSC®/NASTRAN, a BM500 piezoelectric actuator bonded on an aluminum cantilever beam is chosen as the test case. Figure 3.11 gives the model studied.

Finite element model is constructed by MSC®/PATRAN and is given in Figure 3.12. In the modeling of the smart structure, solid-solid modeling technique is used. The beam and the piezoceramic are modeled by 171 CHEXA solid elements. The material properties of the aluminum beam are: E = 67 GPa, $\nu = 0.33$ and $\rho = 2730$ kg/m^3. The electromechanical properties of the BM500 are given in Appendix A.

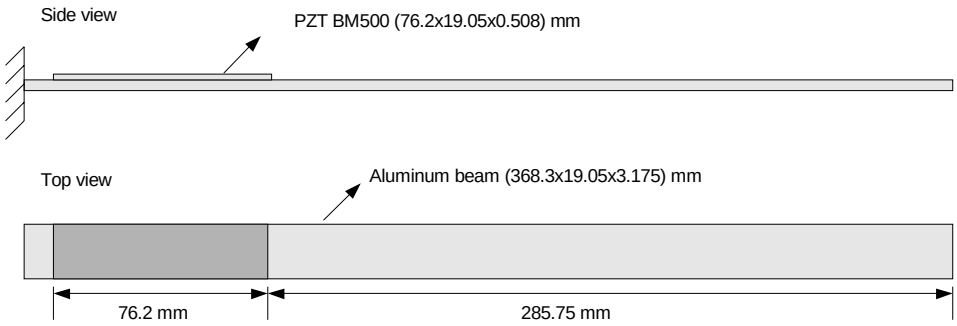

Figure 3.11 Reference model for dynamic analysis: An aluminum cantilever beam with PZT actuator

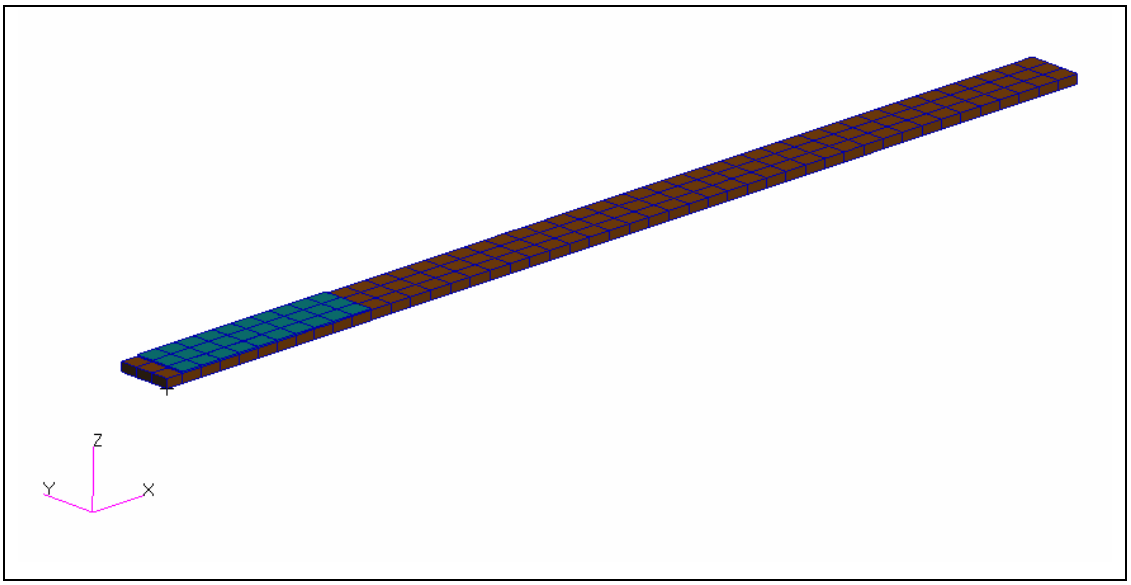

Figure 3.12 Finite element model of the cantilever beam with PZT actuator

Frequency response analysis of the beam is performed by MSC®/NASTRAN for a constant actuation voltage of $\Delta V = 0.2828V$ (*i.e.* $\Delta T = 0.2828^{o}C$ in the TEMP card). The frequency response function (FRF) between the voltage applied to the piezoelectric actuator and the transverse velocity at 211 mm from the clamped end is used to compare

the NASTRAN thermal analogy results with the reference model results obtained by three-dimensional piezoelectric finite element formulation [48]. As shown in Figure 3.13, thermal analogy and reference study results are very close to each other. Therefore, as it was also concluded for the static analysis case, the piezoelectric thermal analogy can be used to simulate a voltage actuation for dynamic analysis.

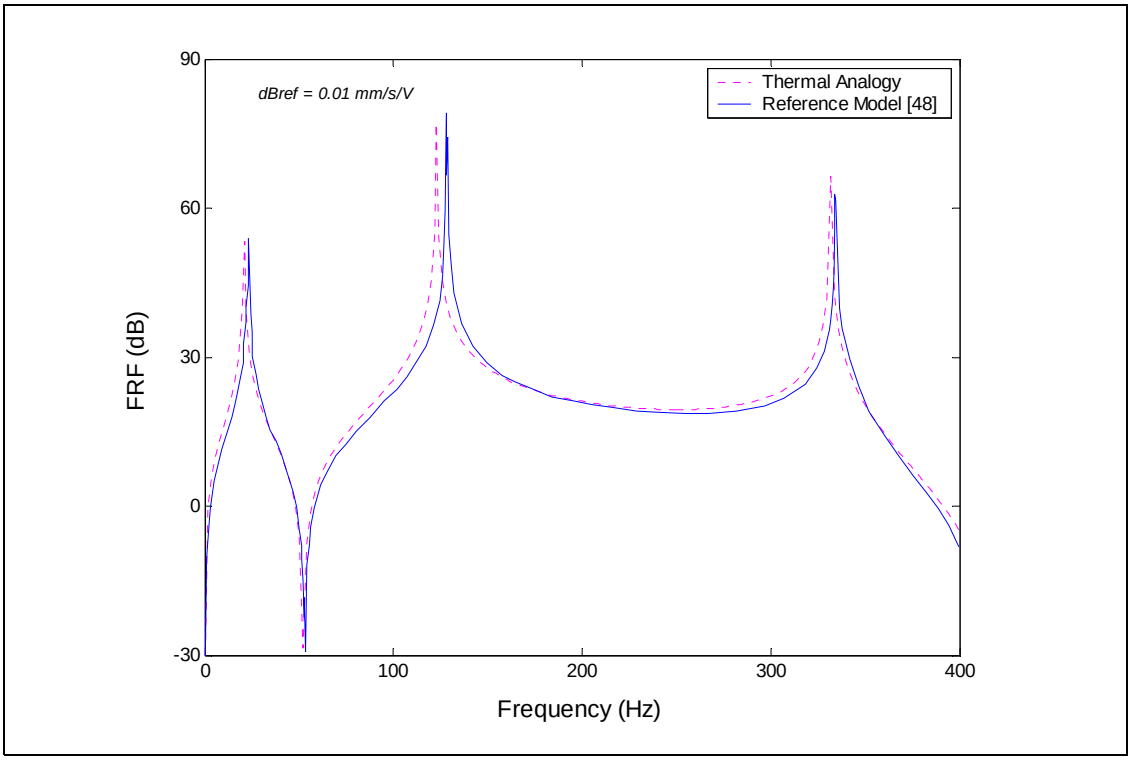

Figure 3.13 Frequency response function of the cantilever beam with PZT actuator

3.5.3 Application of the Thermal Analogy Method to the Smart Beam

The thermal analogy method is also applied to determine the static behavior of the smart beam models developed in Section 3.3. The three smart beam models are subjected to a piezoelectric actuation of 300V via thermal analogy using MSC®/NASTRAN. The deformation results of the three different models are shown in Figure 3.14. It can be seen

from Figure 3.14 that the tip deflection results are very close to each other, and also close to the result of 1.015 mm obtained by ANSYS® using piezoelectric finite elements [43].

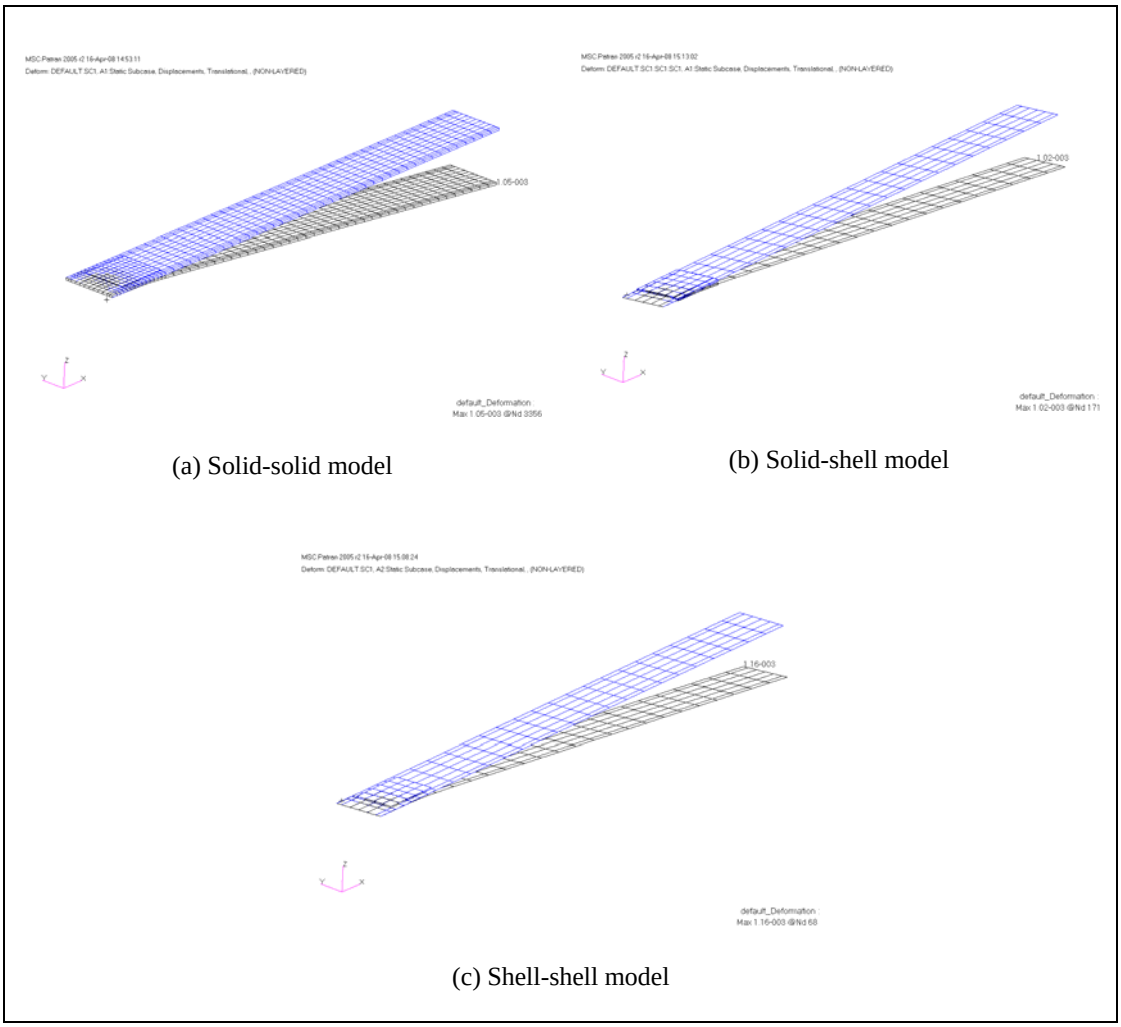

(a) Solid-solid model

(b) Solid-shell model

(c) Shell-shell model

Figure 3.14 Deformation of the smart beam models
for the piezoelectric actuation of 300V

3.6 Structural Modeling of the Smart Fin

In this section, the structural model of the smart fin is constructed. The smart fin consists of a cantilever aluminum passive plate-like structure with symmetrically surface bonded twenty-four piezoelectric actuator patches (25mm x 25mm x 0.5mm, Sensortech BM500 type). The actual system is shown in Figure 3.15 and the schematic of the smart fin showing the placement of the actuators is presented in Figure 3.16. The material properties of the aluminum plate are: E = 69 GPa, $\nu = 0.33$ and $\rho = 2768$ kg/m^3 and the thickness of the plate is 0.93 mm. The electromechanical properties of the piezoelectric patches are given in Appendix A.

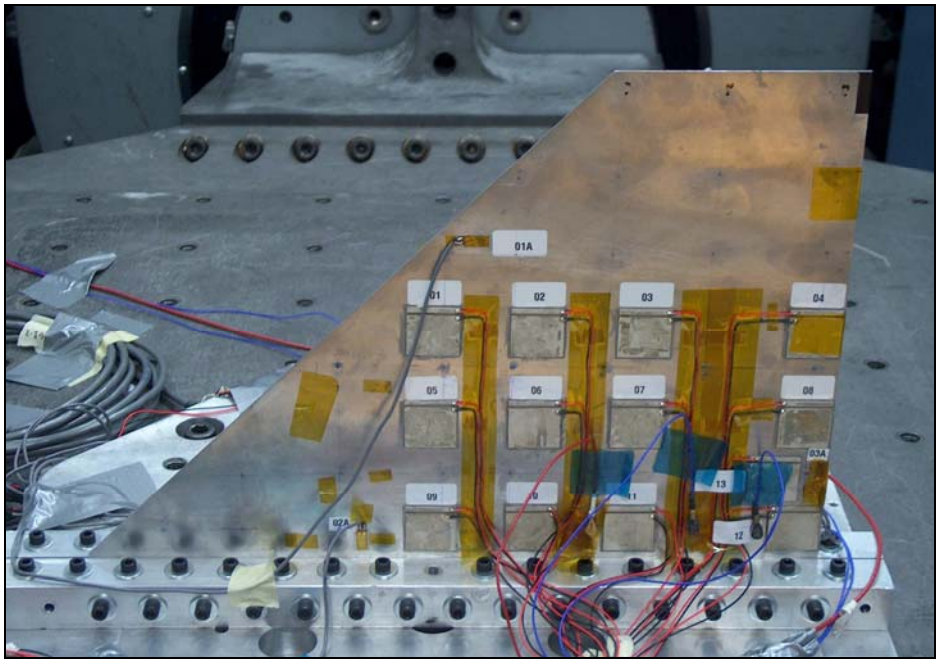

Figure 3.15 The smart fin used in the study

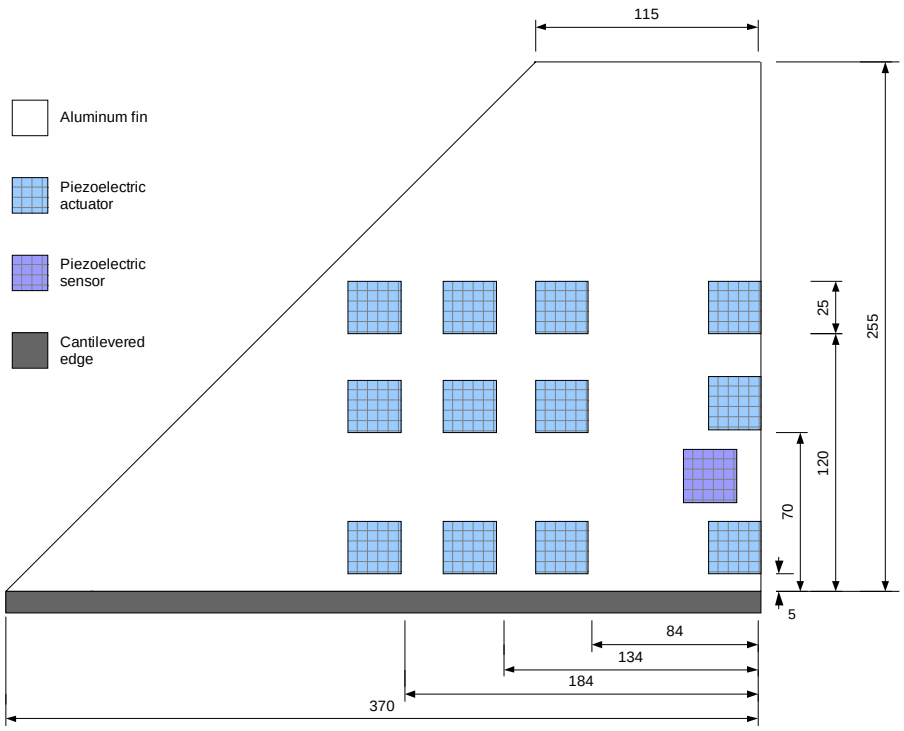

Figure 3.16 Schematic view of the smart fin (all dimensions in mm)

Finite Element Model of the smart fin is constructed with solid-shell modeling approach using MSC®/PATRAN. The piezoelectric patches and the part of the aluminum fin between the patches are modeled by 156 eight-node CHEXA type solid elements; the remaining part of the fin is modeled by 400 quadrilateral CQUAD4 type and 21 triangular CTRIA3 type shell elements. The solid and shell elements of the fin are connected by RSSCON type multipoint constraints. Figure 3.17 shows the finite element model of the smart fin.

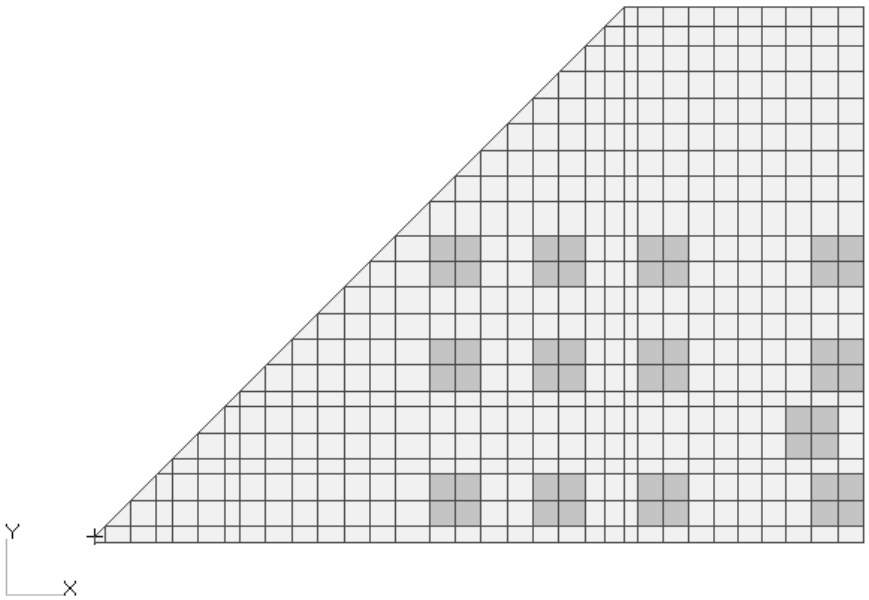

Figure 3.17 Finite element model of the smart fin
(959 nodes and 156 CHEXA, 400 CQUAD4 and 21 CTRIA3 elements)

A normal modes analysis is performed using MSC®/NASTRAN to determine the natural frequencies and mode shapes of the smart fin. Besides the finite element analysis, open loop experiments are also performed for the determination of the structural characteristics of the smart fin. The theoretically determined resonance frequencies of the smart fin are compared with the experimentally measured ones in Table 3.3, resulting in very good coincidence. Modal critical damping ratios extracted from the experimental data are also listed in Table 3.3. Critical damping ratios, ξ at each mode were obtained by the "Half Power Point" method from the following equation:

$$\xi = \frac{\Delta f}{2 \times f_n} \tag{3.10}$$

where Δf is the bandwidth of the response peak at the half-power point (equal to 0.707 times peak amplitude) and f_n is the resonance frequency.

Figure 3.18 shows the first three mode shapes of the smart fin. It can be seen that the first mode can be defined as the first out of plane bending mode, the second mode is predominantly torsional and the third mode is the second out of plane bending mode.

Table 3.3 Theoretically and experimentally obtained natural frequencies and the experimentally determined damping ratios of the smart fin

Mode number	Frequency (Hz)		Experimental Critical Damping Ratio
	FEM	Experimental	
1	16.03	15.0	0.0190
2	47.11	50.75	0.0148
3	72.60	73.75	0.0091

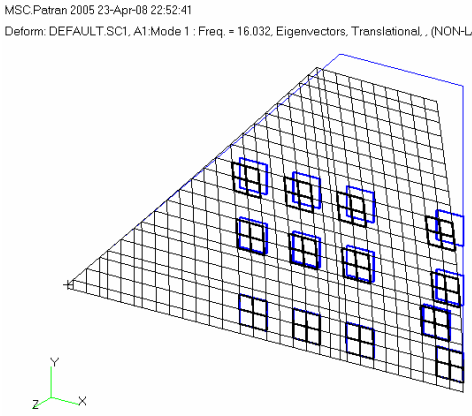

(a) Mode 1 (1st bending)

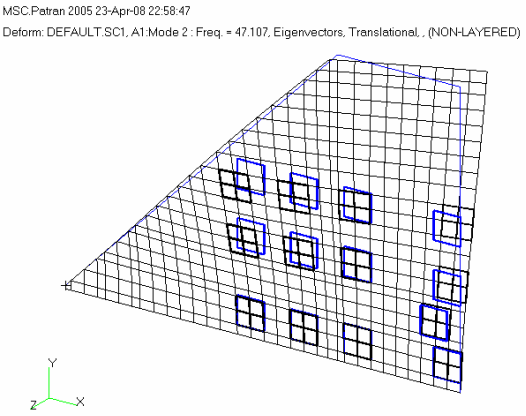

(b) Mode 2 (1st torsional)

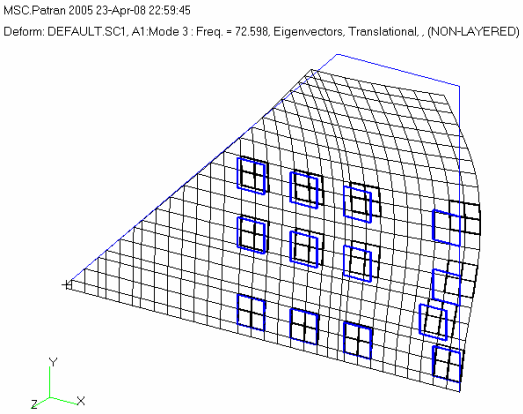

(c) Mode 3 (2nd bending)

Figure 3.18 The first three mode shapes of the smart fin

3.7 Conclusions

In this chapter, different finite element modeling techniques in MSC®/PATRAN were presented for the smart structures and the techniques were verified by using a smart beam. It was shown that the solid-solid modeling, in which the passive and active portions of the smart structure are modeled by solid elements, can be an approach for the simple smart structures, but the increased structural stiffening and computing time limit the potential applications of this approach on realistic aerospace structures. In order to eliminate these difficulties, solid-shell and shell-shell modeling techniques in which the passive portion of the smart structure is modeled by the shell elements, were also developed. These modeling techniques can be used effectively to obtain the finite element model of the smart structures. In this thesis, the structural model of the smart fin is constructed by solid-shell modeling approach.

In order to simulate voltage actuation applied to the piezoelectric actuators of the smart structures in MSC®/NASTRAN, a method based on the analogy between thermal strains and piezoelectric strains was presented. The application of this method was discussed using reference models. The static and dynamic results obtained by the thermal analogy were compared with the reference results computed by three-dimensional piezoelectric finite element formulation and very good agreement was observed. It is concluded that the thermal analogy method can be efficiently used to simulate the voltage actuation in the smart structures. This method will be used later chapters, in obtaining the aeroelastic state-space representation of the smart fin.

CHAPTER 4

STATE-SPACE REPRESENTATION OF THE SMART FIN UNDER UNSTEADY AERODYNAMIC LOADING

4.1 Introduction

This chapter presents a technique for the state-space representation of the aeroelastic model of the smart fin. The technique is based on a rational approximation of the unsteady aerodynamic loads in the Laplace domain, which yields state-space matrix equations of motion with constant coefficients. Figure 4.1 shows the flowchart for the numerical modeling procedure used in the thesis. With given geometry and material properties of the smart structure, the finite element model is formed and the structural matrices and vibration characteristics are obtained by using the finite element analysis. The thermal analogy method, mentioned in the previous chapter, is applied in the finite element analysis in order to obtain piezoelectric actuation properties. The structural and aerodynamic models of the smart structure are connected with splines. This model together with the vibration characteristics are used to obtain the unsteady aerodynamics in tabular form for various airflow parameters. The Roger's approximation and least-square method are applied to convert the unsteady aerodynamics into Laplace domain aerodynamics. A state-space system is constructed by integrating structural matrices, vibration, actuation and sensing characteristics of the smart structure, and the resulting aerodynamics. This chapter outlines these numerical procedures. Then, the state-space approach is verified by performing a flutter analysis of a test case. Finally, the state-space aeroelastic model of the smart fin is constructed and the open loop characteristics are investigated.

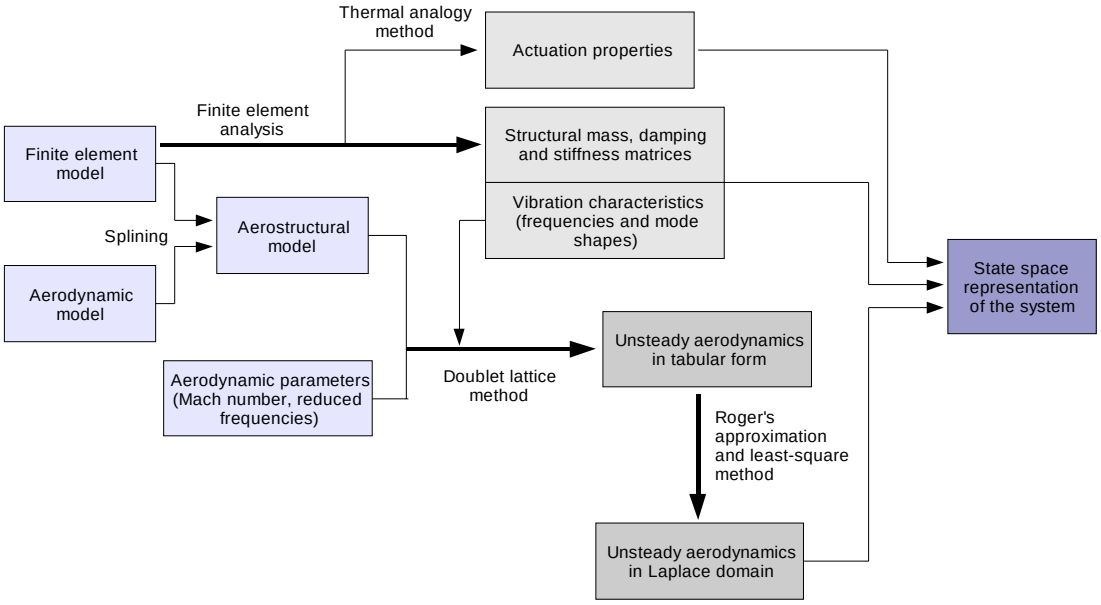

Figure 4.1 Flowchart to obtain the numerical model of smart structures under unsteady aerodynamic loading

4.2 Generalized Aeroelastic Equations of Motion

For a smart structure under aerodynamic loading, the aeroelastic equation of motion can be written as [38,49]:

$$[M]\{\ddot{x}(t)\}+[D]\{\dot{x}(t)\}+[K]\{x(t)\}=\lfloor F_p \rfloor\{u\}+\{F_a(x(t))\} \tag{4.1}$$

where $[M]$, $[D]$ and $[K]$ denote global mass, damping and stiffness matrices, respectively. $\{x(t)\}$ is the structural displacement vector; $\lfloor F_p \rfloor$ is the force matrix due to unit electric voltage. $\{F_a(x(t))\}$ represents aerodynamic force induced by the structural deformation and is a time function of the structural deformation.

Most of the commercially available unsteady aerodynamic packages assume that the structure undergoes harmonic oscillations. Thus, Equation (4.1) can be rewritten in the frequency domain as:

$$(-\omega^2[M]+i\omega[D]+[K])\{x(i\omega)\}=[F_p]\{u\}+\{F_a(x(i\omega))\} \tag{4.2}$$

where ω is the frequency of the excitation.

Aerodynamic forces are the functions of the flight speed and altitude and their calculation heavily relies on the theoretical predictions that require unsteady aerodynamic computations. Unsteady aerodynamic forces acting on the structure of a linear aeroelastic system can be expressed in the frequency domain as [50]:

$$\{F_a(x(i\omega))\}=q_\infty[Q(ik)]\{x(i\omega)\} \tag{4.3}$$

where $q_\infty=\frac{1}{2}\rho V_\infty{}^2$ is the dynamic pressure where ρ is the density of air and V_∞ is the free stream velocity. $[Q(ik)]$ is the aerodynamic influence coefficient matrix and is

complex function of reduced frequency *k* and flight conditions. The reduced frequency is defined as $k = \omega b / 2V_\infty$, where *b* is a reference chord length, and is a measure of the unsteadiness of the flow. A reduced frequency of zero represents the steady case while high values of reduced frequency indicate that unsteady effects are significant. $[Q(ik)]$ is calculated at several reduced frequencies for a given Mach number and air density by using aerodynamic theories such as Doublet Lattice Method (DLM) [24].

By substituting Equation (4.3) into (4.2) yields

$$(-\omega^2[M] + i\omega[D] + [K] - q_\infty[Q(ik)])\{x(i\omega)\} = [F_p]\{u\} \tag{4.4}$$

In order to improve computational efficiency, the system size is usually reduced with the modal approach. In the modal approach the response of the system is described in terms of a linear combination of the lower order natural modes of the system:

$$\{x(i\omega)\} = [\phi]\{\zeta(i\omega)\} \tag{4.5}$$

where $[\phi]$ is the modal matrix and $\{\zeta(i\omega)\}$ is the modal displacement vector.

Substituting Equation (4.5) into (4.4) and pre-multiplying by the transpose of the modal matrix $[\phi]^T$ yields

$$(-\omega^2[\overline{M}] + i\omega[\overline{D}] + [\overline{K}] - q_\infty[\overline{Q}(ik)])\{\zeta(i\omega)\} = [\overline{F}_p]\{u\} \tag{4.6}$$

where $[\overline{M}]$, $[\overline{D}]$, $[\overline{K}]$ and $[\overline{Q}(ik)]$ denote the $n \times n$ modal mass, modal damping, modal stiffness and aerodynamic influence coefficient matrices respectively. *n* represents the number of modes contributing the response. $[\overline{F}_p]$ is the $n \times L$ modal force matrix due to the unit applied voltage, where *L* is the number of the PZT actuators. Those matrices can be defined as:

$$
\begin{aligned}
\left[\overline{M}\right] &= [\phi]^T [M][\phi] \\
\left[\overline{D}\right] &= [\phi]^T [D][\phi] \\
\left[\overline{K}\right] &= [\phi]^T [K][\phi] \\
\left[\overline{Q}(ik)\right] &= [\phi]^T [Q(ik)][\phi] \\
\left[\overline{F}_p\right] &= [\phi]^T \left[F_p\right]
\end{aligned}
\tag{4.7}
$$

Equation (4.6) can also be written in the Laplace domain as:

$$
(s^2\left[\overline{M}\right] + s\left[\overline{D}\right] + \left[\overline{K}\right] - q_\infty\left[\overline{Q}(s)\right])\{\zeta(s)\} = \left[\overline{F}_p\right]\{u\} \tag{4.8}
$$

where $s = i\omega$ is the Laplace variable. Equation (4.8) is the generalized aeroelastic equations of motion in Laplace Domain.

4.3 Unsteady Aerodynamic Force Approximation

A fundamental phenomenon in unsteady subsonic aerodynamics is that the disturbance shed into the flow by the moving structure continues to affect the loads at a later time. Mathematically, this phenomenon results in nonrational expressions for the aerodynamic influence coefficients $\left[\overline{Q}(ik)\right]$ [51]. As mentioned in the previous section, $\left[\overline{Q}(ik)\right]$ is calculated at several discrete reduced frequencies rather than as a continuous function of the Laplace variable *s*. In order to cast the dynamic aeroelastic equation of motion in a state-space form, which can be readily utilized in the modern control theories, the aerodynamic influence coefficients have to be approximated by rational functions of s (namely, fraction of polynomials of *s*).

There are several methods used in approximating unsteady generalized aerodynamic forces using rational functions, such as matrix-Pade approximant technique [26],

Roger's method [25] and the minimum-state method of Karpel [27]. In this thesis the Roger's method is used.

The Roger's approximation to the unsteady aerodynamics is given by [25]:

$$\left[\overline{Q}_{app}(ik)\right] = \left[A_0\right] + \left[A_1\right](ik) + \left[A_2\right](ik)^2 + \sum_{j=3}^{N} \frac{(ik)\left[A_j\right]}{(ik + \gamma_{j-2})} \tag{4.9}$$

where $\left[A_i\right]$ are real coefficient matrices to be determined such that the assumed matrix form approximates the tabulated matrices and γ_{j-2} are the aerodynamic lag parameters which are usually preselected in the range of reduced frequencies of interest. Equation (4.9) includes the noncirculatory static aerodynamic force $\left[A_0\right]$, the aerodynamic damping $\left[A_1\right](ik)$, the apparent aerodynamic mass $\left[A_2\right](ik)^2$, and the circulatory aerodynamic lag terms represented by the summation term.

In order to separate the real and imaginary parts of $\left[\overline{Q}_{app}(ik)\right]$, the summation term in Equation (4.9) can be written under the following form:

$$\sum_{j=3}^{N} \frac{(ik)}{(ik + \gamma_{j-2})}\left[A_j\right] = \sum_{j=3}^{N} \frac{(ik)(\gamma_{j-2} - ik)}{k^2 + \gamma_{j-2}^2}\left[A_j\right] = \sum_{j=3}^{N} \left(\frac{k^2}{k^2 + \gamma_{j-2}^2} + i\frac{k\gamma_{j-2}}{k^2 + \gamma_{j-2}^2}\right)\left[A_j\right] \tag{4.10}$$

Then the real and imaginary parts of $\left[\overline{Q}_{app}(ik)\right]$ can be written as:

$$\begin{aligned} \left[\overline{Q}_{app,R}(ik)\right] &= \left[A_0\right] - \left[A_2\right]k^2 + \sum_{j=3}^{N} \frac{k^2\left[A_j\right]}{k^2 + \gamma_{j-2}^2} && \text{(Real part)} \\ \left[\overline{Q}_{app,I}(ik)\right] &= \left[A_1\right]k + \sum_{j=3}^{N} \frac{\gamma_{j-2}k\left[A_j\right]}{k^2 + \gamma_{j-2}^2} && \text{(Imaginary part)} \end{aligned} \tag{4.11}$$

At each value of the reduced frequency, real and imaginary error functions are determined from Equation (4.11) as:

$$\begin{aligned}\left[E_{R,i}\right] &= \left[\overline{Q}_{R,i}\right] + \left[F_{R,i}\right]\{H\} \\ \left[E_{I,i}\right] &= \left[\overline{Q}_{I,i}\right] + \left[F_{I,i}\right]\{H\}\end{aligned} \tag{4.12}$$

where

$$\left[F_{R,i}\right] = \left[-1 \quad 0 \quad k_i^2 \quad \frac{-k_i^2}{k_i^2 + \gamma_{j-2}{}^2} \quad . \quad . \quad \frac{-k_i^2}{k_i^2 + \gamma_{N-2}{}^2}\right]$$

$$\left[F_{I,i}\right] = \left[0 \quad -k_i \quad 0 \quad \frac{-\gamma_{j-2}k}{k_i^2 + \gamma_{j-2}{}^2} \quad . \quad . \quad \frac{-\gamma_{N-2}k}{k_i^2 + \gamma_{N-2}{}^2}\right]$$

$$\{H\} = \begin{Bmatrix} [A_0] \\ [A_1] \\ . \\ . \\ . \\ [A_N] \end{Bmatrix}$$

i refers to a particular reduced frequency k_i at which aerodynamic influence coefficient matrix is calculated.

Approximation coefficients $[A_0], [A_1], ..., [A_N]$ can be obtained by least square error technique [52]. Defining a complex error function as:

$$\left[E_i\right] = \left[E_{R,i}\right] + i\left[E_{I,i}\right] \tag{4.13}$$

A least-squares fit can be passed through *l* data points by setting

$$\frac{\partial}{\partial\{H\}} \sum_{i=1}^{l} \left(\left[E_i\right] \times \left[E_i'\right]\right) = 0 \tag{4.14}$$

where $[E_i']$ is the complex conjugate of $[E_i]$.

Solving Equation (4.14) for the coefficients of the fit $\{H\}$, one obtains the following:

$$\{H\} = -\left[\sum_{i=1}^{l}([F_{R,i}]^T[F_{R,i}] + [F_{I,i}]^T[F_{I,i}])\right]^{-1}\sum_{i=1}^{l}([\overline{Q}_{R,i}][F_{R,i}]^T + [\overline{Q}_{I,i}][F_{I,i}]^T) \quad (4.15)$$

Substituting $k = \omega b / 2V_\infty$ into Equation (4.9), one obtains the approximated aerodynamic forces in the Laplace domain as:

$$[\overline{Q}(s)] = [A_0] + [A_1](\frac{b}{2V_\infty})s + [A_2](\frac{b}{2V_\infty})^2 s^2 + \sum_{j=3}^{N}\frac{[A_j]}{(s + \frac{2V_\infty}{b}\gamma_{j-2})}s \quad (4.16)$$

Coefficients $[A_0],[A_1],...,[A_N]$ are determined from Equation (4.15). The values of γ are selected to be in the reduced frequency range of interest.

4.4 State-Space Equation of Motion

Substituting approximated aerodynamic forces, Equation (4.16), into the generalized aeroelastic equations of motion, Equation (4.8), results in the following equation:

$$\begin{aligned}&((\overline{[M]} - \frac{1}{8}\rho b^2[A_2])s^2 + (\overline{[D]} - \frac{1}{4}\rho b V_\infty[A_1])s + \overline{[K]} - \frac{1}{2}\rho V_\infty^2[A_0] \\ &- q_\infty\sum_{j=3}^{N}\frac{s}{(s + \frac{2V_\infty}{b}\gamma_{j-2})}[A_j])\{\zeta(s)\} = [\overline{F}_p]\{u\}\end{aligned} \quad (4.17)$$

Defining aerodynamic lag terms as a new augmented state such that

$$\{\zeta_{aj}(s)\} = \frac{s}{(s + \frac{2V_\infty}{b}\gamma_{j-2})}\{\zeta(s)\} \tag{4.18}$$

Making use of Equation (4.18) in Equation (4.17) and writing the resulting equation in the time domain results in the following time domain constant coefficient equation:

$$[\tilde{M}]\{\ddot{\zeta}(t)\} + [\tilde{D}]\{\dot{\zeta}(t)\} + [\tilde{K}]\{\zeta(t)\} - q_\infty\left[\sum_{j=3}^{N}[A_j]\right]\{\zeta_{aj}(t)\} = [\bar{F}_p]\{u\} \tag{4.19}$$

where $[\tilde{M}] = [\bar{M}] - \frac{1}{8}\rho b^2[A_2]$

$$[\tilde{D}] = [\bar{D}] - \frac{1}{4}\rho b V_\infty[A_1]$$

$$[\tilde{K}] = [\bar{K}] - \frac{1}{2}\rho V_\infty^2[A_0]$$

Defining the state vector $\{x\}$ as $\{\zeta \quad \dot{\zeta} \quad \zeta_{a3} \quad \cdots \quad \zeta_{aN}\}^T$, the state-space form of Equation (4.19) can now be written as:

$$\{\dot{x}\} = [A]\{x\} + [B]\{u\} \tag{4.20}$$

where

$$[A] = \begin{bmatrix} [0] & [I] & [0] & \cdots & [0] \\ -[\tilde{M}]^{-1}[\tilde{K}] & -[\tilde{M}]^{-1}[\tilde{D}] & q_\infty[\tilde{M}]^{-1}[A_3] & \cdots & q_\infty[\tilde{M}]^{-1}[A_N] \\ [0] & [I] & -(\frac{2V_\infty}{b})\gamma_1[I] & \cdots & [0] \\ \vdots & \vdots & \vdots & \ddots & \vdots \\ [0] & [I] & [0] & \cdots & -(\frac{2V_\infty}{b})\gamma_{N-2}[I] \end{bmatrix}_{nN\times nN}$$

$$[B]=\begin{bmatrix} [0] \\ [\tilde{M}]^{-1}[\overline{F}_p] \\ [0] \\ \vdots \\ [0] \end{bmatrix}_{nN\times L}$$

The state vector $\{x\}$ consists of the modal displacement $\{\zeta\}$, modal velocity $\{\dot{\zeta}\}$ and the augmented states $\{\zeta_{aj}\}$. $[A]$ describes the system matrix and $[B]$ gives the input matrix. These matrices are real constant matrices. The control input $\{u\}$ is the applied voltages to the PZT actuators. System matrix $[A]$ includes all aerodynamic effects such as apparent mass, aerodynamic damping and stiffness as well as structural mass, damping and stiffness. It should be noted that the system matrix $[A]$ is a function of air speed.

Defining *R* as the number of sensors on the smart structure, the output $\{y\}$ of the system can be written in modal coordinates as follows:

$$\{y\}=[C_q][\phi]\{\zeta\}+[C_v][\phi]\{\dot{\zeta}\} \tag{4.21}$$

where $[C_q]$ and $[C_v]$ give the displacement and velocity output matrices, respectively. The displacement and velocity output matrices represent the finite element nodes where the response is measured. If no measurement is made on a node in the finite element model, its value is set to zero otherwise taken to be unity. In the state-space form Equation (4.21) can be given by

$$\{y\}=[C]\{x\} \tag{4.22}$$

where

$$[C]=\begin{bmatrix}[\overline{C}_q] & [\overline{C}_v] & [0] & \cdots & [0]\end{bmatrix}_{R\times nN}$$

here, $[C]$ defines the output matrix. $[\overline{C}_q] = [C_q][\phi]$ and $[\overline{C}_v] = [C_v][\phi]$ are the modal displacement and velocity output matrices, respectively.

Equations (4.20) and (4.22) give the state-space representation for smart structures under unsteady aerodynamic loading. This state-space form allows the use of control algorithms, and facilitates root-locus analysis, which relies on performing a root-loci analysis to determine the variation of the roots of the system with airspeed, to obtain open loop flutter characteristics of an aeroelastic system.

4.5 Numerical Validation of the State-Space Approach: Open Loop Flutter Estimation of an Aft-Swept Flat-Plate Wing Model

In order to verify the developed state-space approach, an open loop flutter analysis of a test case is performed using root-locus analysis and the results are compared to those obtained by MSC®/NASTRAN/Aeroelasticity I [53]. The case is an aft-swept flat-plate wing model studied by Dansberry *et al*. [54]. The planform geometry of the wing is illustrated in Figure 4.2. The model is a flat-plate semispan wing cut from 3.175 mm-thick aluminum sheet (6061-T6). Material properties are *E* = 69.6 GPa, $\nu = 0.33$ and $\rho = 2712.6$ kg/m3. The wing is cantilevered at the root.

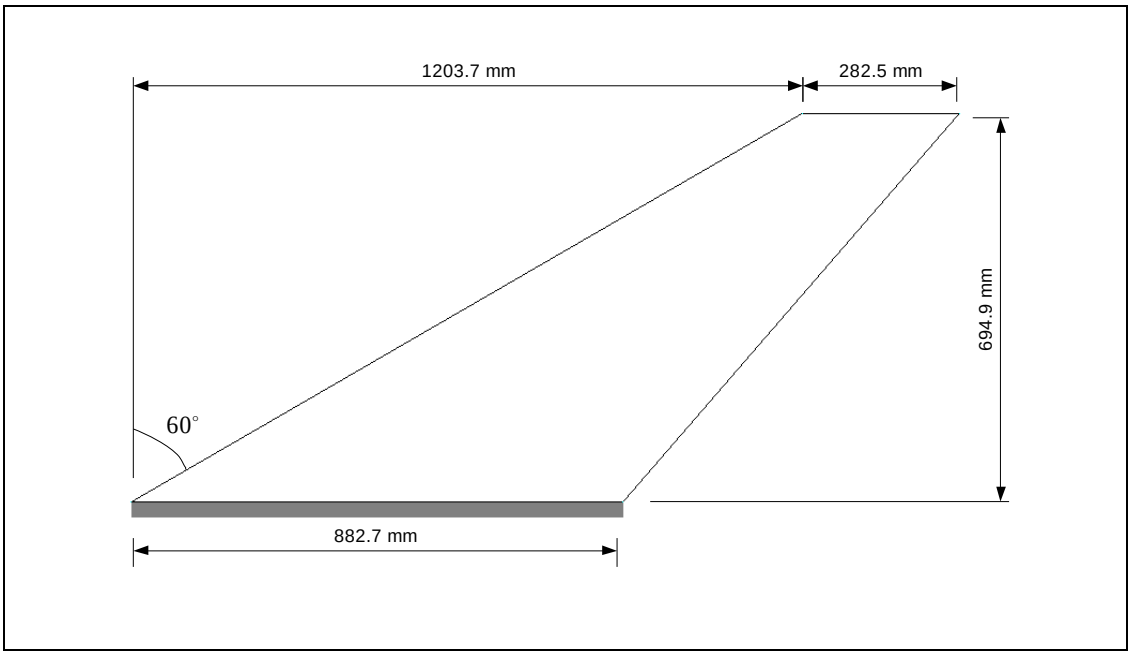

Figure 4.2 Planform geometry of the wing model

The finite element model of the wing is shown in Figure 4.3. The model has a total of 231 nodes and consists of 200 quadrilateral CQUAD4 type shell elements. A free vibration analysis is performed in order to determine the natural frequencies and the mode shapes of the wing. The first four natural frequencies and mode shapes are determined by using the Lanczos method of MSC®/NASTRAN. The natural frequencies of the analysis are compared with experimentally determined ones in Table 4.1. Theoretical and experimental natural frequencies are in very good agreement with each other. Figure 4.4 shows the first four mode shapes of the wing. The first mode can be defined as the first out of plane bending mode, the second mode is predominantly torsional, the third mode is the second out of plane bending mode and the fourth mode is the second torsion mode.

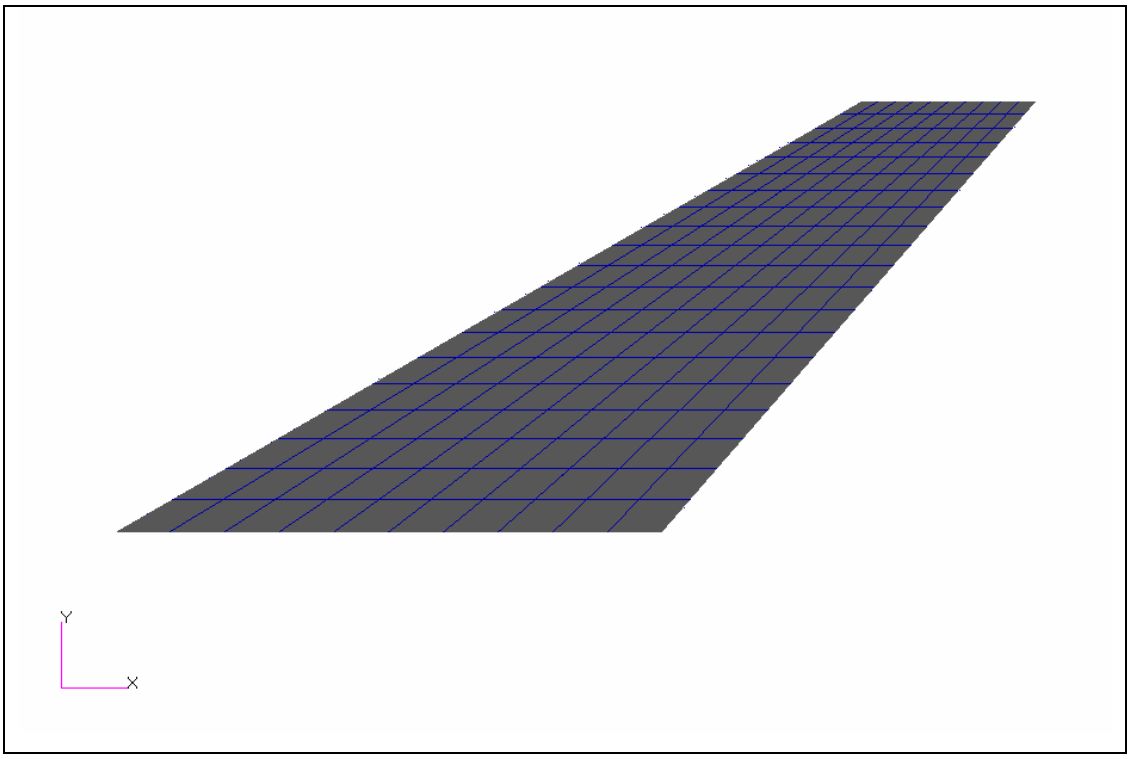

Figure 4.3 Finite element model of the aft-swept wing

Table 4.1 Natural frequencies of the aft-swept flat-plate wing

Mode number	Finite element analysis (Hz)	Experimental (Hz) [54]
1	4.1	4.4
2	16.9	16.7
3	28.3	28.8
4	40.5	40.0

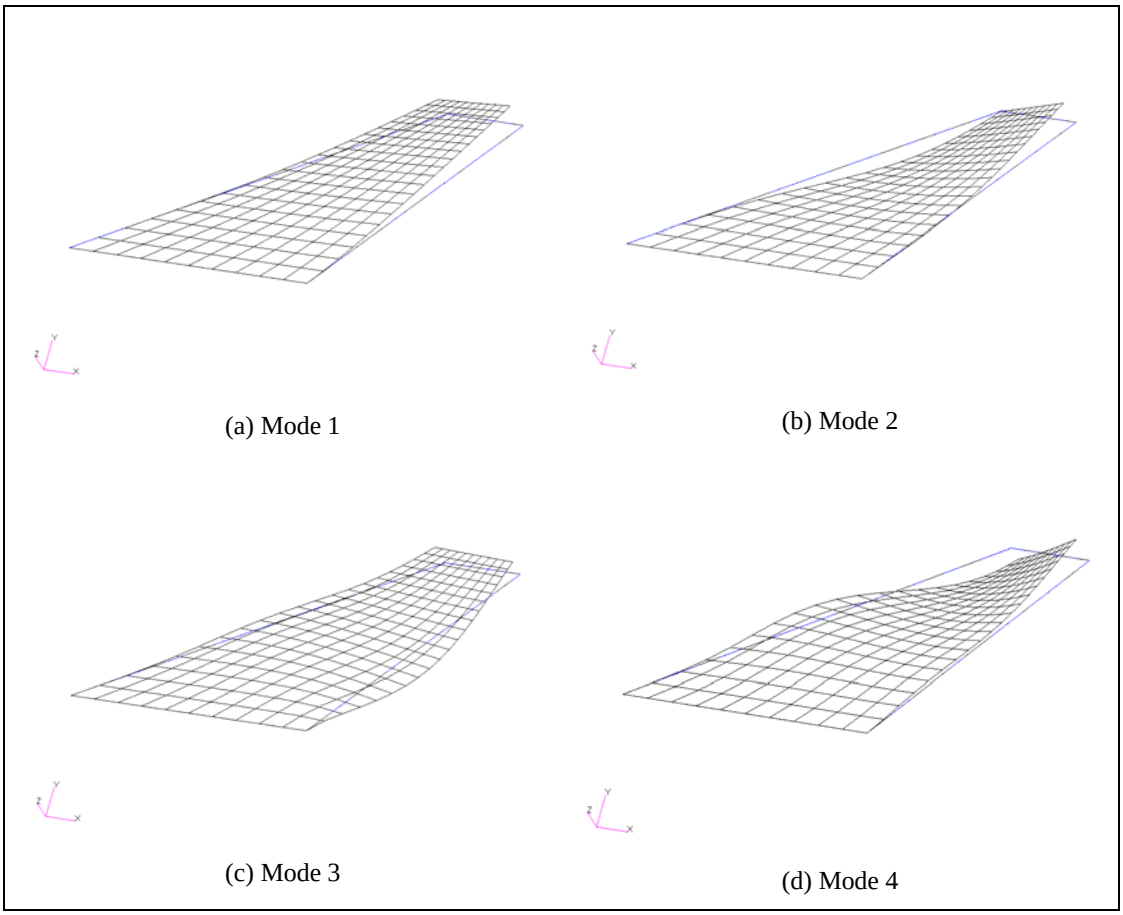

Figure 4.4 The first four theoretical mode shapes of the aft-swept wing

For unsteady aerodynamic force calculation, the wing is modeled as a flat plate lifting surface with 50 aero boxes. The span is divided into 10 and the chord is divided into 5 elements. Figure 4.5 depicts the aerodynamic model of the wing. Structural and aerodynamic models are connected by using finite plate splines (SPLINE4) of MSC®/NASTRAN. The spline elements are used to transform the loads calculated on the aerodynamic mesh onto the structure and interpolate displacements on the aerodynamic mesh using the structural displacements. Figure 4.6 shows both aerodynamic and structural models for the wing. Structural model mesh size is smaller and presented by grey shading while aerodynamic surface mesh is taken slightly bigger with yellow shading.

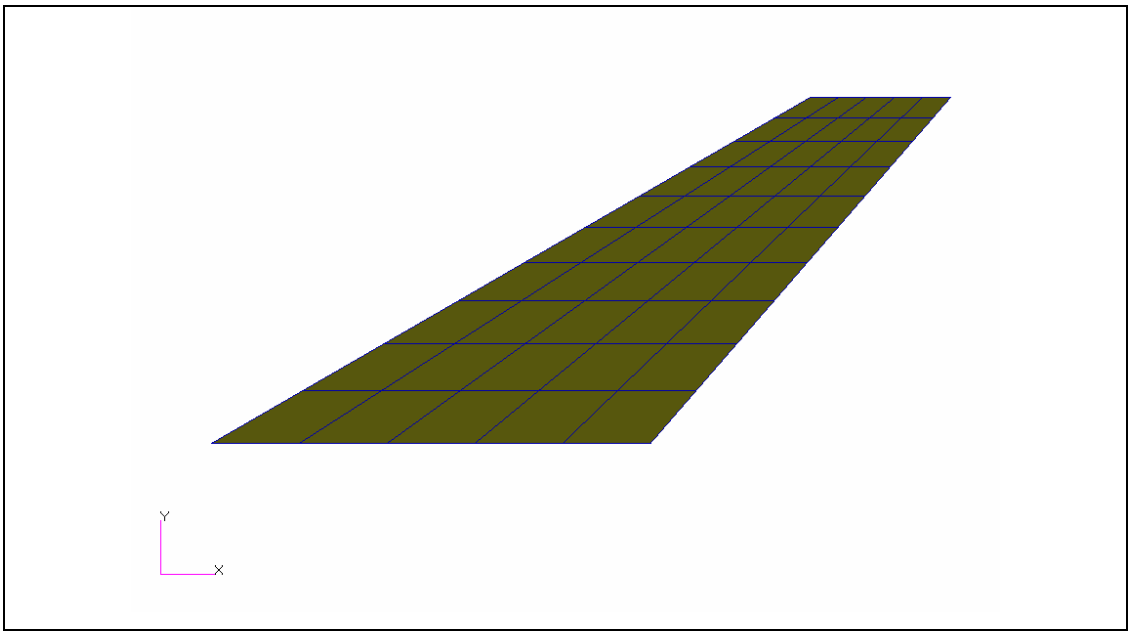

Figure 4.5 Aerodynamic model of the aft-swept wing

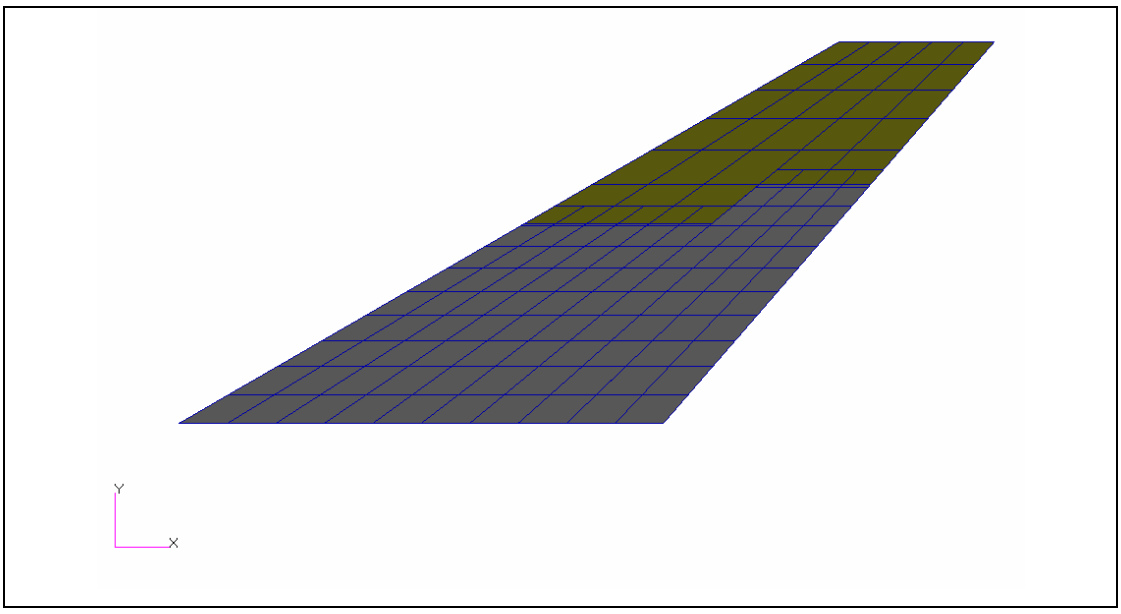

Figure 4.6 Structural and aerodynamic models for the aft-swept wing

The generalized aerodynamic influence coefficient matrices $\left[\overline{Q}(ik)\right]$ in modal domain are calculated by using the DLM in MSC®/NASTRAN for ten values of reduced frequencies (k = 0.01, 0.05, 0.1, 0.15, 0.2, 0.25, 0.3, 0.35, 0.4, 0.5) and extracted utilizing Direct Matrix Abstraction Programme (DMAP) from MSC®/NASTRAN. The flight conditions are an air density of $\rho = 1.1507$ kg/m^3 and low subsonic velocity regime (Mach number, $M_\infty = 0.2$). The first four modes are selected as generalized coordinates. The calculated discrete aerodynamic influence coefficient matrices are then approximated by Roger's approximation and least-squares method with an in-house code developed in MATLAB® [55]. Four aerodynamic lag term coefficients were used in Roger's approximation, which effectively means N=6 in Equation (4.9). The chosen values of lag term coefficients are $\gamma_1 = 0.05$, $\gamma_2 = 0.2$, $\gamma_3 = 0.3$, $\gamma_4 = 0.4$ which are in the reduced frequency range of interest. Figures 4.7 and 4.8 show curve fittings obtained by using Roger's approximation as compared to the tabulated MSC®/NASTRAN DLM data for $\overline{Q}_{11}, \overline{Q}_{12}, \overline{Q}_{21}$ and $\overline{Q}_{22}$ terms of $\left[\overline{Q}(ik)\right]$. Both the calculated and fitted values are in very good agreement with each other.

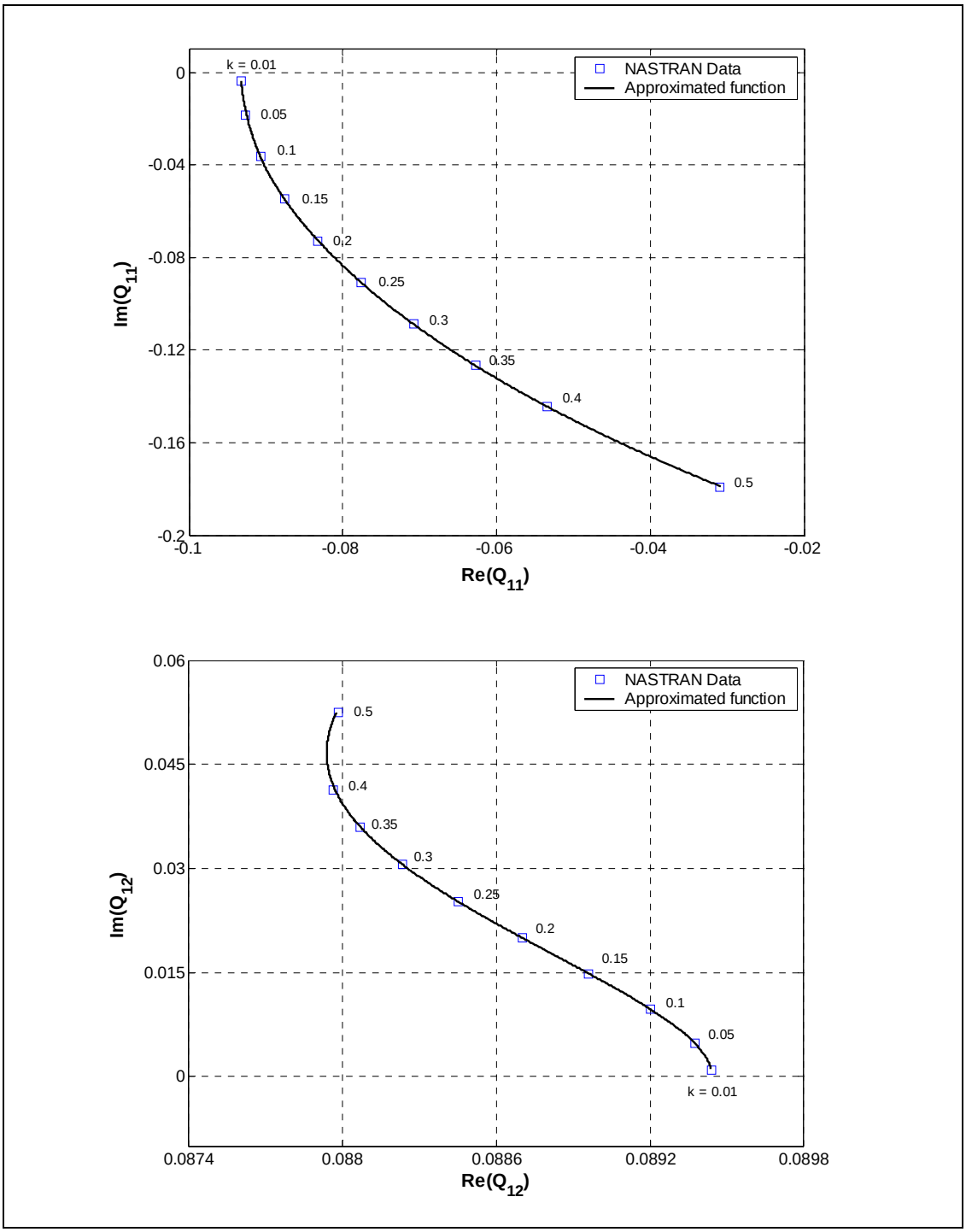

Figure 4.7 Approximation of $\overline{Q}_{11}$ and $\overline{Q}_{12}$ by Roger's approximation and least-squares method for the aft-swept wing ($M_\infty = 0.2$)

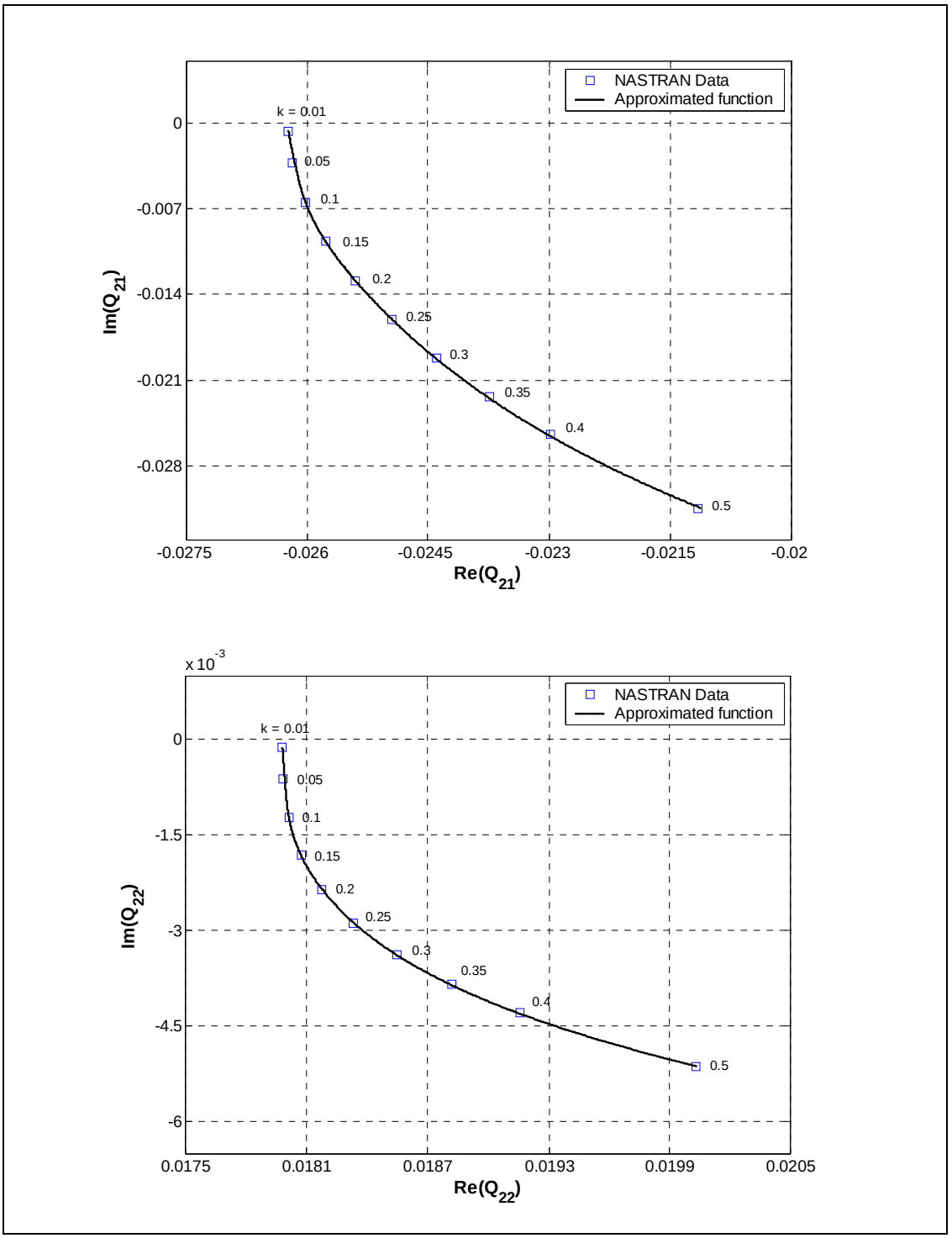

Figure 4.8 Approximation of $\overline{Q}_{21}$ and $\overline{Q}_{22}$ by Roger's approximation and least-squares method for the aft-swept wing ($M_\infty = 0.2$)

Flutter analysis of the wing is then conducted by using the root-locus method. The structural modal mass, damping and stiffness matrices are obtained from MSC®/NASTRAN using DMAP statements. A structural damping ratio of 0.02 is assumed. By using approximated aerodynamic forces along with the structural matrices, system matrix $[A]$ of the wing model is built at a given air density of $\rho = 1.1507$ kg/m^3. Solving Equation (4.20) for flight velocities ranging from 20 m/sec to 90 m/sec, the roots of the aeroelastic system are obtained. Figure 4.9 shows the velocity root-locus plot of the wing model. The plot traces the roots of the system as the flight velocity changes. The horizontal axis is the real part and the vertical axis is the imaginary part of the roots. The imaginary axis represents the point of neutral stability. Flutter is represented on the root-locus plot by a pole crossing this axis into the right half plane. It can be seen from the figure that the frequencies of the first and second aeroelastic modes coalescence as the flow velocity increases and the second mode pole crosses the imaginary axis at a speed of 76.11 m/sec and a frequency of 13.51 Hz which represents the flutter speed and the flutter frequency of the wing respectively. Experimentally determined flutter speed is 78.33 m/sec and the flutter frequency is 13.2 Hz [54], which are very close to ones obtained by state-space approach.

Flutter characteristics of the wing are also determined by the pk-method of MSC®/NASTRAN. The solution is requested for the first four modes and a series of speeds ranging from 20 to 90 m/sec. Figures 4.10 and 4.11 show velocity vs. damping (V-g) and velocity vs. frequency (V-f) curves obtained by pk-method for the first two aeroelastic modes. In the figures, the corresponding curves obtained by the root-locus method are also given. V-g curve for the root-locus method is plotted by utilizing the definition of $g = 2\,\mathrm{Re}(p)/f$ where Re(p) is the real part of the system root obtained by root-locus analysis and f is the frequency [53]. As it can be seen from Figures 4.9 and 4.10, the variations of damping and frequency with the speed for both methods are in very good agreement and V-g curve and V-f curve obtained by pk-method indicate a flutter speed of 76.07 m/sec and a flutter frequency of 13.52 Hz. These flutter speed and frequency results are very close to ones obtained by root-locus analysis of the state-space model. Table 4.2 gives the comparison of the flutter analysis results of state-space

approach with MSC®/NASTRAN analysis. The open loop flutter estimation by state-space approach appears to be reasonable.

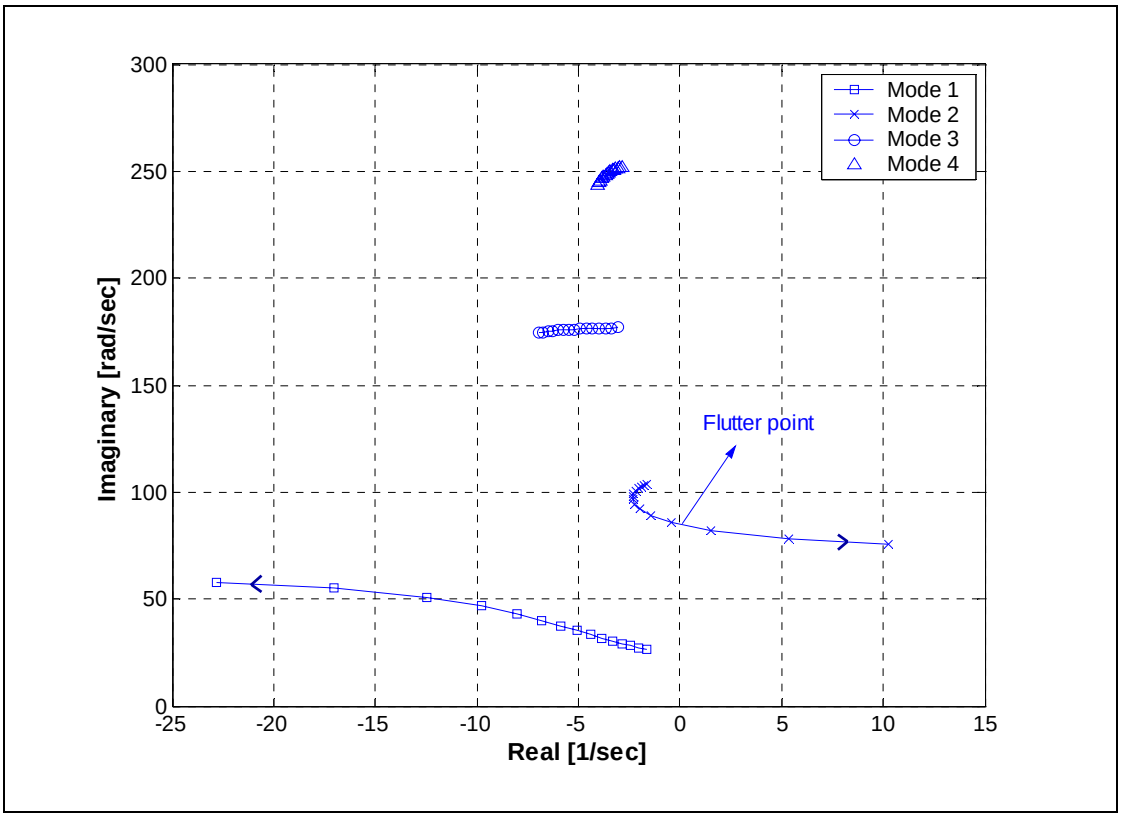

Figure 4.9 Root-locus of the state-space model of the aft-swept wing as a function of the flight speed ($\rho = 1.1507$ kg/m^3)

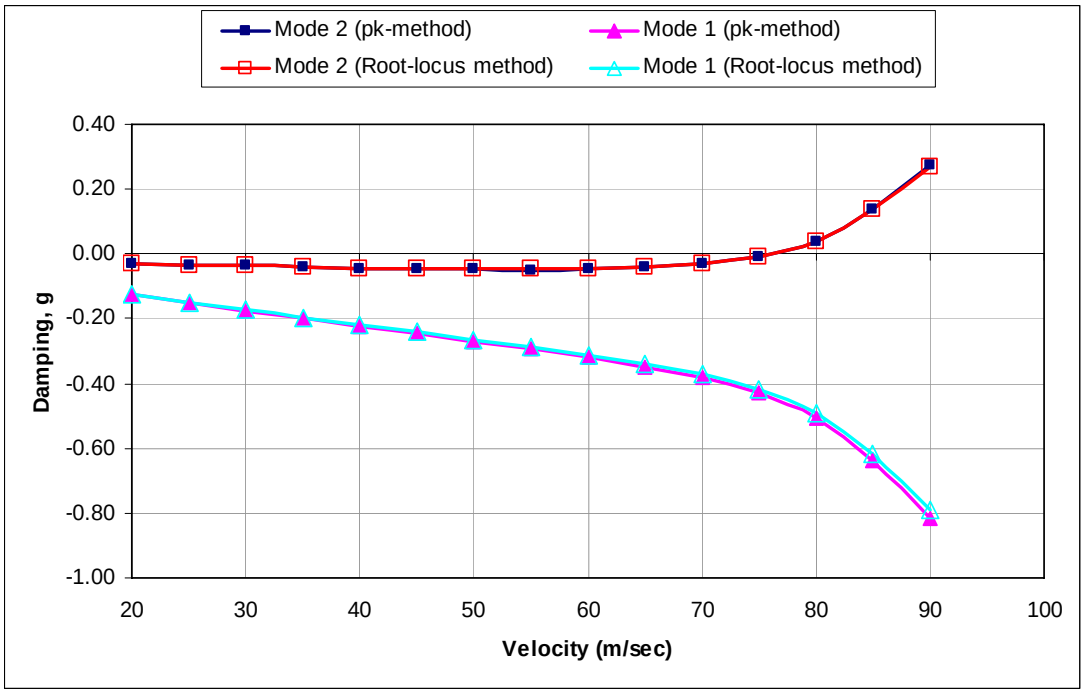

Figure 4.10 Velocity vs. damping plot of the aft-swept wing ($\rho = 1.1507$ kg/m^3)

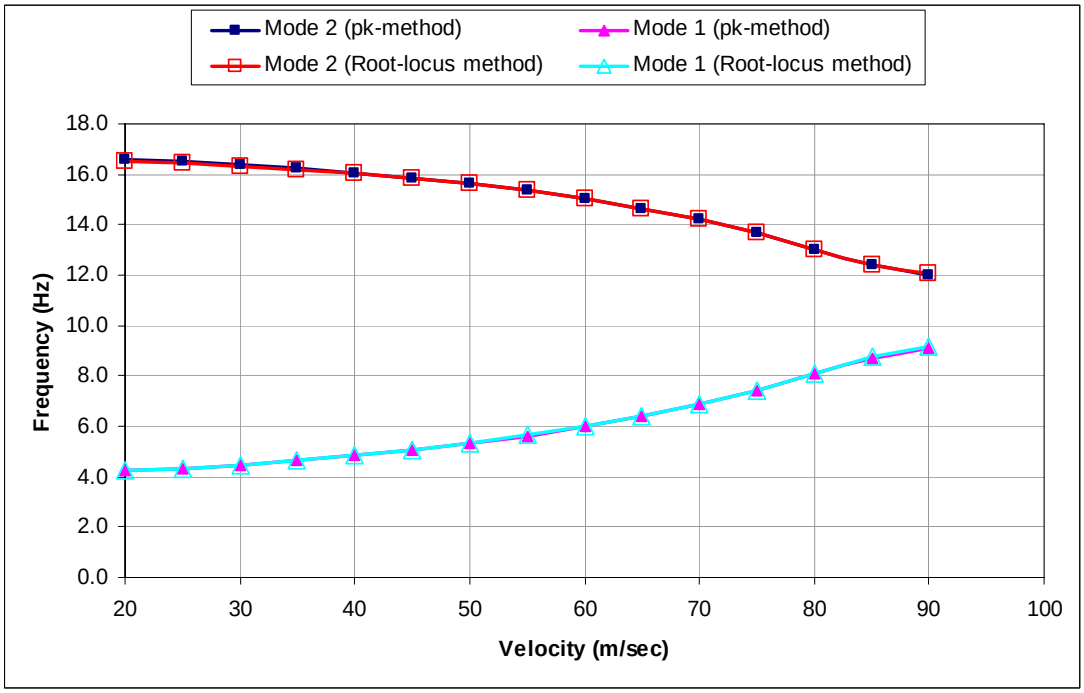

Figure 4.11 Velocity vs. frequency plot of the aft-swept wing ($\rho = 1.1507$ kg/m^3)

Table 4.2 Comparison of the flutter analysis results of the state-space approach with NASTRAN for the aft-swept wing ($\rho = 1.1507$ kg/m^3)

	Flutter velocity (m/sec)	Flutter frequency (Hz)
MSC®/NASTRAN	76.07	13.52
State-Space Approach	76.11	13.51
% Deviation from NASTRAN	0.053	0.074

4.6 State-Space Representation of the Aeroelastic Model of the Smart Fin

In this section, the state-space model of the smart fin is presented. For several flight conditions, the open loop flutter characteristics and the system responses under piezoelectric actuation for the smart fin are given.

For unsteady aerodynamics calculation, an aerodynamic model of the fin is formed. The span is divided into 14 and the chord is divided into 12 elements and Figure 4.12 represents the case. The finite plate splines (SPLINE4) of MSC®/NASTRAN are used in order to connect structural and aerodynamic models. Figure 4.13 shows both aerodynamic and structural models for the smart fin. Structural model mesh size is smaller and presented by grey and green shading while aerodynamic surface mesh is taken slightly bigger with yellow shading. The structural finite element model of the smart fin constructed in Chapter 3 is used as the structural model.

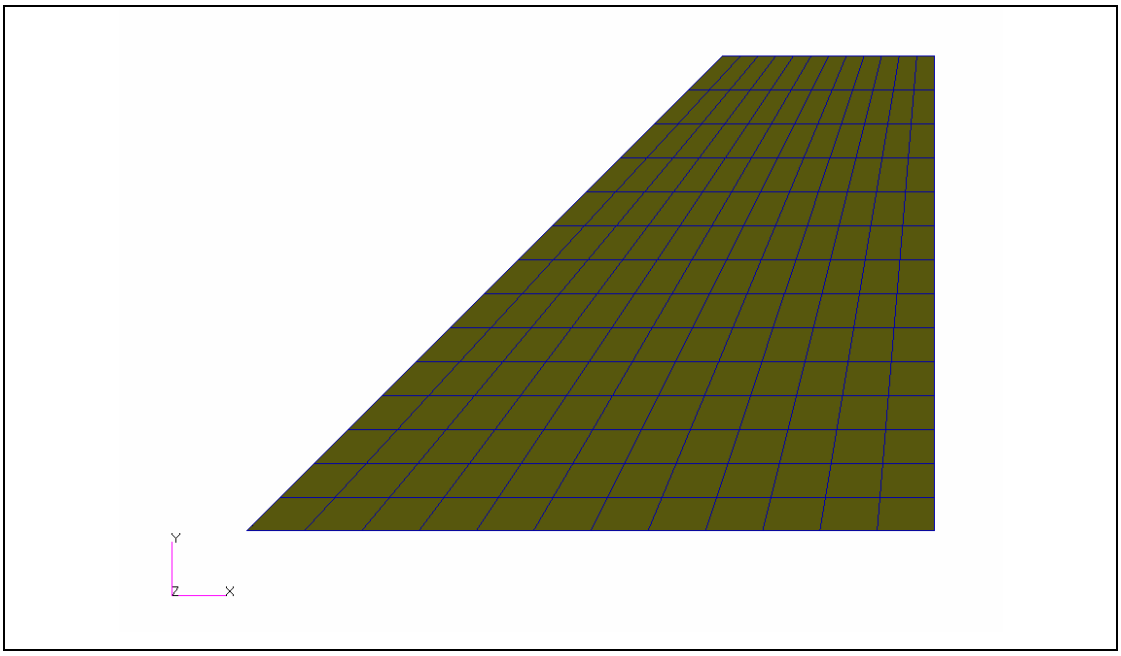

Figure 4.12 Aerodynamic model of the smart fin

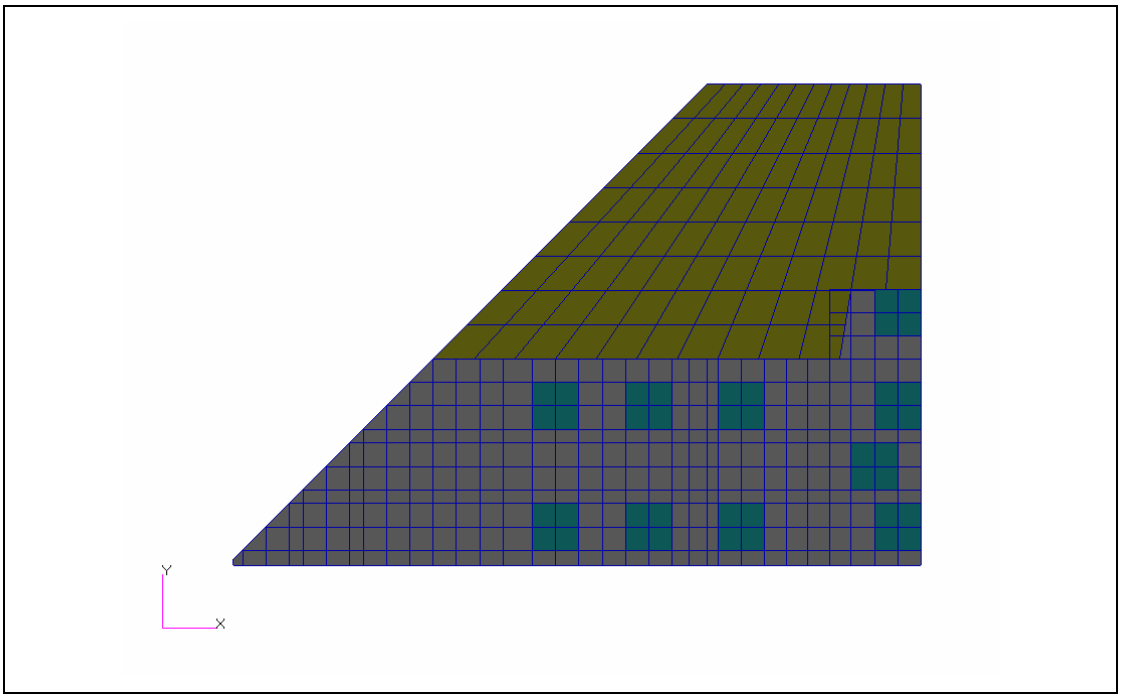

Figure 4.13 Structural and aerodynamic models for the smart fin

The aerodynamic forces are calculated at $M_\infty = 0.2$ for the reduced frequencies of k = 0.01, 0.05, 0.12, 0.15, 0.2, 0.25, 0.3, 0.35, 0.5 by using the DLM in MSC®/NASTRAN. The first four elastic modes are used in the calculation. The loads are then extracted with DMAP from MSC®/NASTRAN and approximated by Roger's approximation and least-squares method. Figures 4.14 and 4.15 show approximated aerodynamic influence coefficient matrices for $\overline{Q}_{11}, \overline{Q}_{12}, \overline{Q}_{33}$ and $\overline{Q}_{34}$ with the tabulated NASTRAN data. The chosen values of lag term coefficients are $\gamma_1 = 0.05$, $\gamma_2 = 0.2$, $\gamma_3 = 0.3$, $\gamma_4 = 0.4$ which are in the reduced frequency range of interest and provide a good curve fitting.

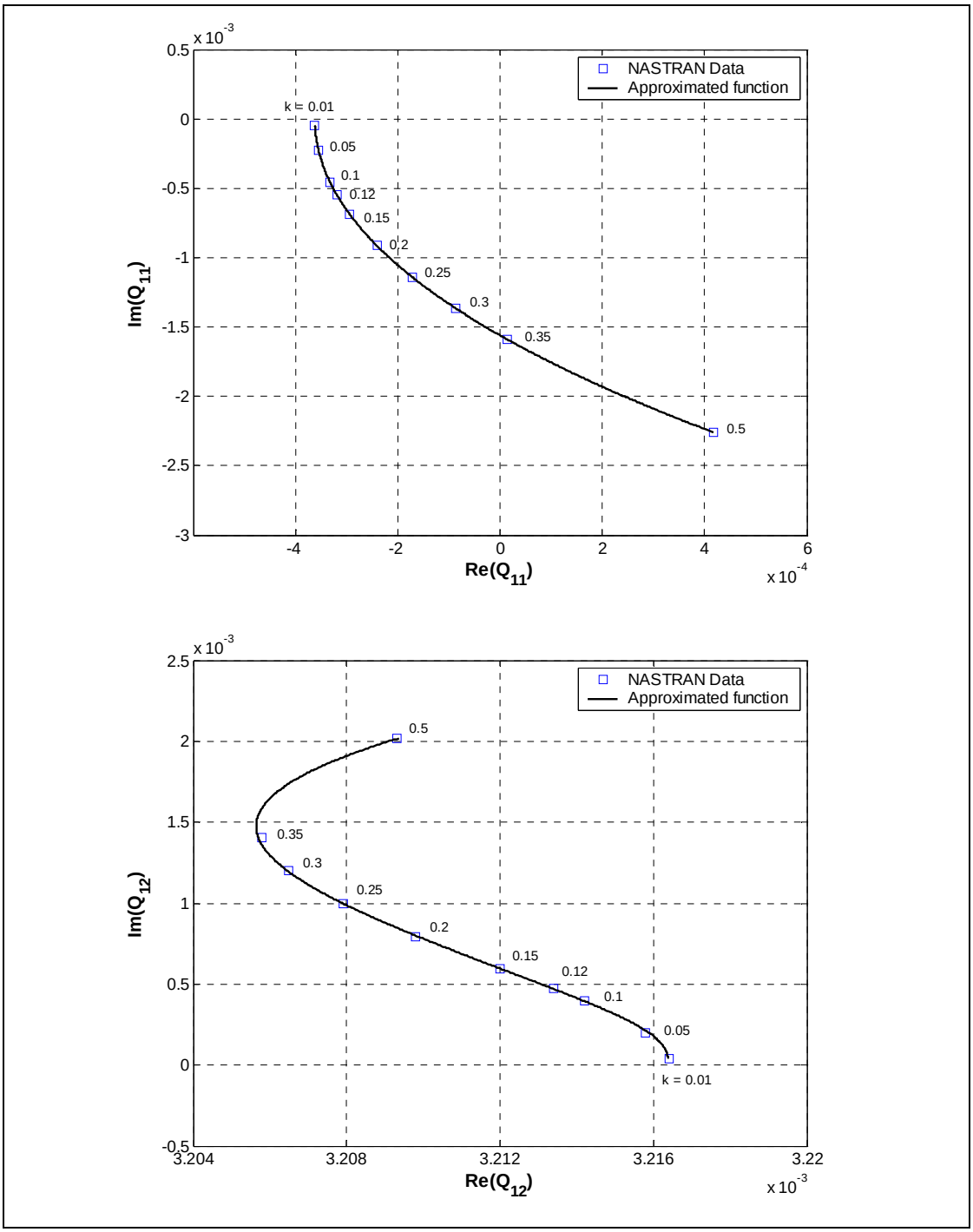

Figure 4.14 Approximation of $\overline{Q}_{11}$ and $\overline{Q}_{12}$ by Roger's approximation and least-squares method for the smart fin ($M_\infty = 0.2$)

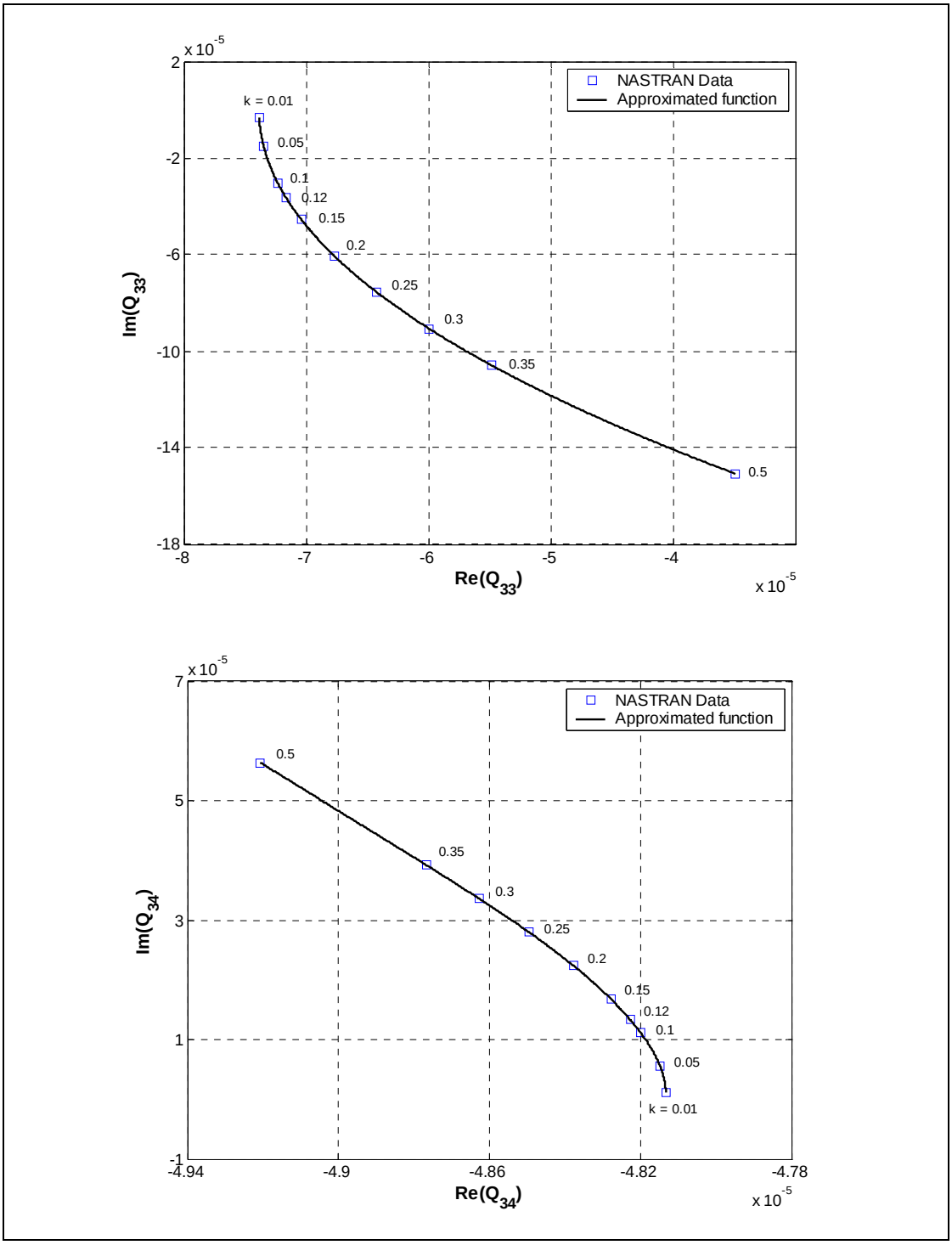

Figure 4.15 Approximation of $\overline{Q}_{33}$ and $\overline{Q}_{34}$ by Roger's approximation and least-squares method for the smart fin ($M_\infty = 0.2$)

The structural modal mass, damping and stiffness matrices of the smart fin are obtained from MSC®/NASTRAN using DMAP statements. By using approximated aerodynamic forces along with the structural matrices, system matrix $[A]$ of the smart fin is formed as a function of air density and flight speed. At sea level density $\rho = 1.225$ kg/m^3, the stability of the system matrix is investigated for several flight velocities: V_∞ as 20, 30, 40, 50, 60, 70, 75, 80, 84, 85, 88, 90 m/sec speeds. Figure 4.16 displays the root-locus plot of the system. The instability is obtained at a speed of 84.10 m/sec and a frequency of 35.69 Hz, which gives the flutter characteristics of the smart fin for the air density of $\rho = 1.225$ kg/m^3.

For the smart fin, flutter boundary is formed by the root-locus analysis of the state-space model. For several air densities, the stability of the system is investigated at different flight velocities. Figure 4.17 shows the flutter boundary of the smart fin. The lines in the figure are constant density ratio lines. The density ratio, m is defined by $m = \rho / \rho_{ref}$ where ρ_{ref} is the reference air density taken as sea level density: $\rho_{ref} = 1.225$ kg/m^3. Each point on the flutter boundary curve gives the dynamic pressure value corresponding to Mach number at which flutter occurs. Unsteady aerodynamic calculations by DLM were made for each density ratio at Mach numbers corresponding to the flutter speeds. The calculated results are matched points in that the flutter speed is consistent with the Mach number for which each individual aerodynamic calculation was made.

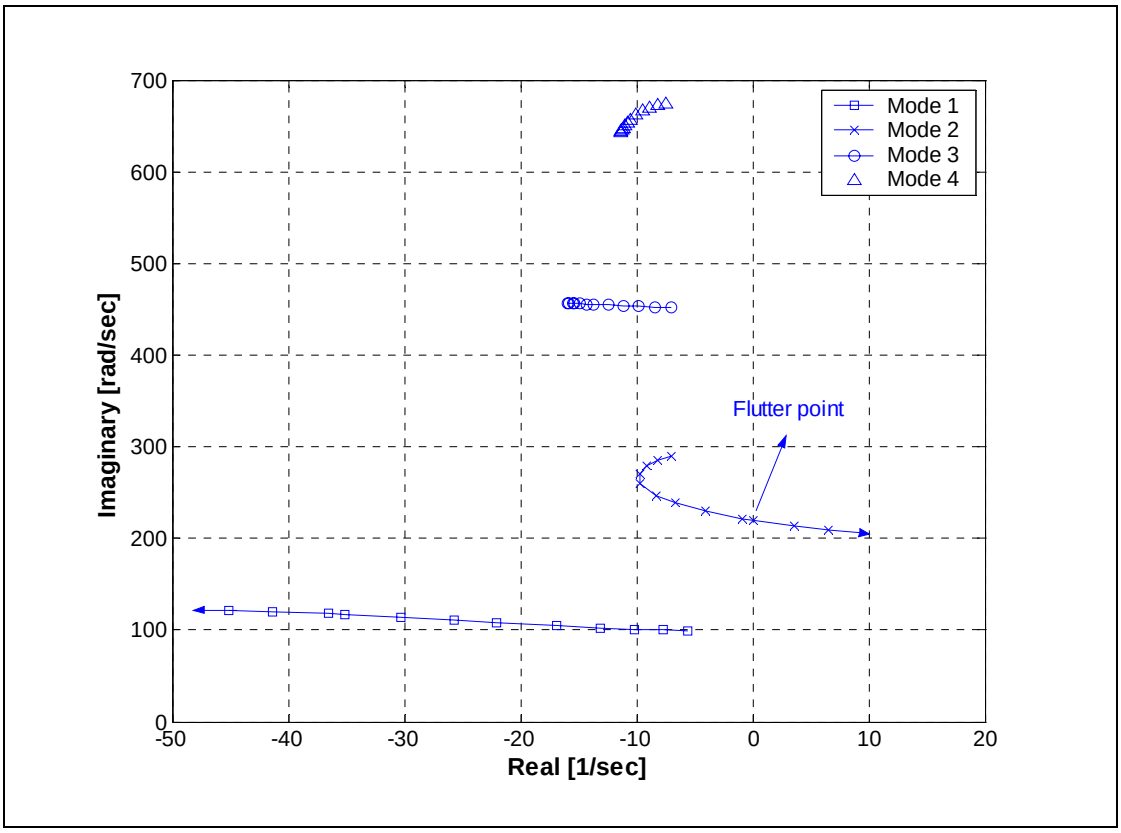

Figure 4.16 Root-locus of the state-space model of the smart fin as a function of the flight speed ($\rho = 1.225$ kg/m^3)

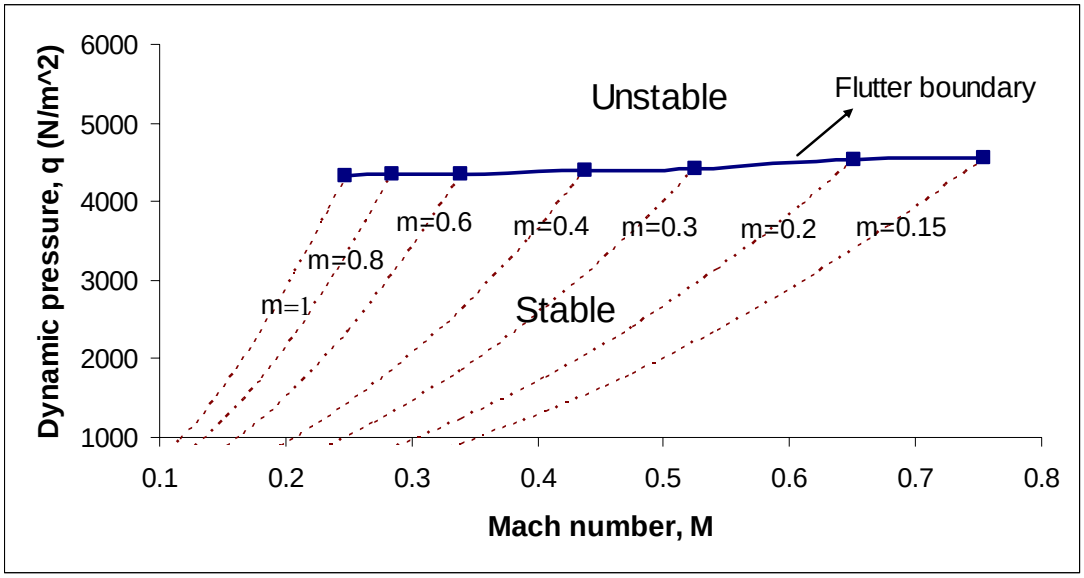

Figure 4.17 Flutter boundary of the smart fin

By using the state-space approach some open-loop system responses of the smart fin are also investigated. The smart fin is excited by using all PZT actuators on one face and the displacement responses of an upper corner point at the trailing edge of the fin is obtained for freestream speeds of $V_\infty = 0$, 50, 84, 90 m/sec at sea level. The displacement output location is shown in Figure 4.18. The unit piezoelectric voltage force vector $\{F_p\}$ was obtained from MSC®/NASTRAN with thermal analogy method by using DMAP. Figure 4.19 shows the time responses of the smart fin to a step input of 1V. As seen from the figure, for the speeds below the flutter speed of 84.10 m/sec the stable behavior is observed, and by increasing the speed the system becomes unstable above the flutter speed.

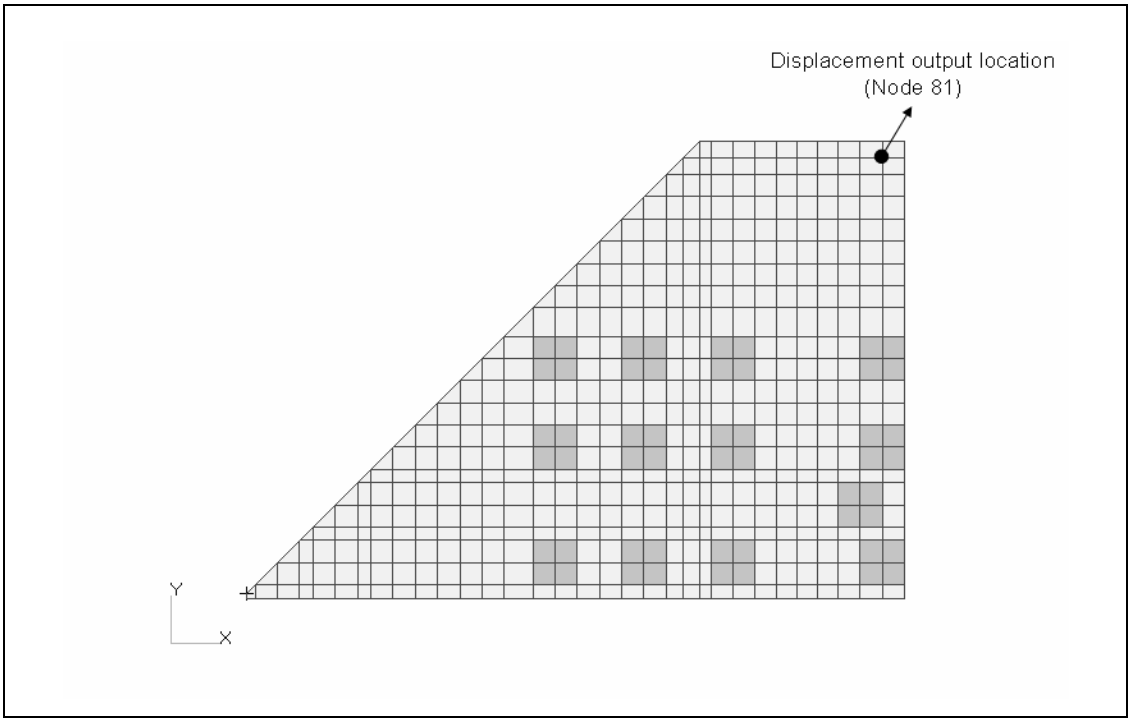

Figure 4.18 Displacement output location on the smart fin

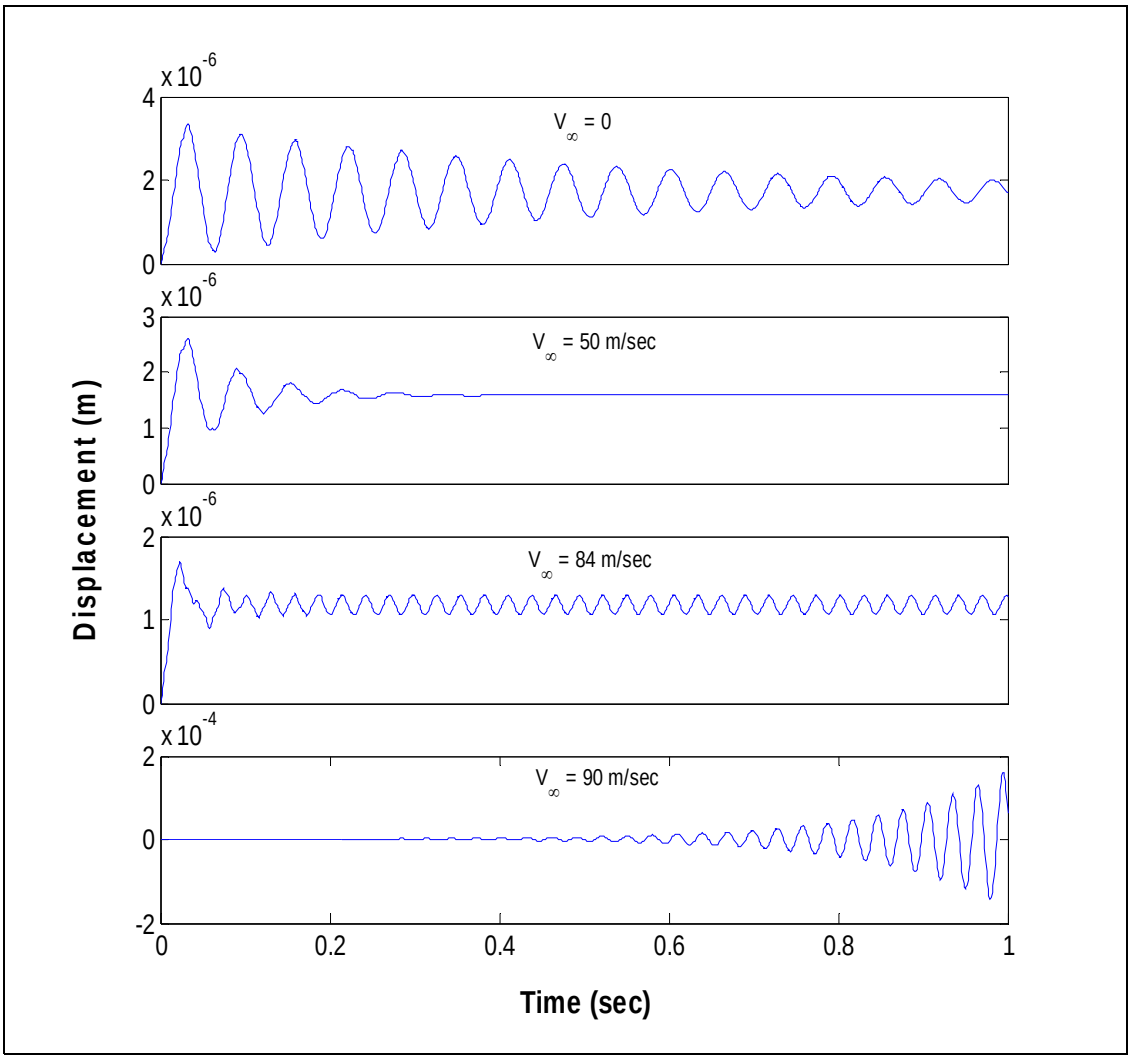

Figure 4.19 Open loop time responses of the smart fin for different flight velocities ($\rho = 1.225$ kg/m^3)

4.7 Conclusions

In this chapter, the mathematical modeling procedure for the smart structures under unsteady aerodynamic loading was presented. Utilizing the finite element method and panel aerodynamic method, and approximating the aerodynamic loads in the complex frequency domain as rational functions, a state-space representation of the aeroelastic model of a smart structure was constructed. The state-space approach was used to predict the flutter characteristics of a swept wing; the results were compared with those obtained from MSC®/NASTRAN/Aeroelasticity solution and a very good agreement was observed. This verifies the state-space approach developed in the thesis.

The state-space representation of the aeroelastic model of the smart fin was constructed and the open-loop system characteristics were also investigated. This state-space model will be used in later chapter, in representing the uncertainties and designing robust controllers for the active flutter suppression of the smart fin.

CHAPTER 5

CONTROLLER DESIGN FOR ACTIVE FLUTTER SUPPRESSION OF THE SMART FIN

5.1 Introduction

This chapter deals with the synthesis of H_∞ controllers for the active flutter suppression of the smart fin. The controllers are designed according to defined performance and uncertainty specifications by considering both SISO (Single-Input Single-Output) and MIMO (Multi-Input Multi-Output) system models which are obtained from the state-space approach developed in Chapter 4. The tip deflections of the smart fin are fed back to derive the piezoelectric actuators. The performances of the controllers in vibration suppression and the enhancement in the flutter boundary of the smart fin are investigated.

5.2 Control Theory

This section describes H_∞ synthesis method and gives the basic definitions and tools used for the formulation of the control problem and robustness analysis of the feedback system.

5.2.1 Basic Definitions and Tools for Control Problem Formulation

Linear Fractional Transformations: Linear fractional transformations (LFTs), as they are currently used in the control literature for analysis and design, were introduced by Doyle [56] and Redheffer [57]. LFTs are powerful and flexible approach to represent uncertainty in matrices and systems. For this reason H_∞ synthesis control problems are formulated in a linear fractional transformation framework. Considering a matrix P of dimension $(n_1 + n_2) \times (m_1 + m_2)$ and partitioning it as follows:

$$P = \begin{bmatrix} P_{11} & P_{12} \\ P_{21} & P_{22} \end{bmatrix} \tag{5.1}$$

and letting the matrices Δ and K have dimensions $(m_1 \times n_1)$ and $(m_2 \times n_2)$, respectively (compatible with the upper and lower partitions of P, respectively), the lower and upper linear fractional transformations can be expressed as:

$$F_l(P,K) = P_{11} + P_{12}K(I - P_{22}K)^{-1}P_{21} \tag{5.2(a)}$$

$$F_u(P,\Delta) = P_{22} + P_{21}\Delta(I - P_{11}\Delta)^{-1}P_{12} \tag{5.2(b)}$$

where subscript l denotes lower and subscript u denotes upper.

Figure 5.1 shows LFT block diagrams. The lower fractional transformation $F_l(P,K)$ is the transfer function resulting from wrapping (positive) feedback K around the lower part of P as illustrated in Figure 5.1(a). To see this, the block diagram in Figure 5.1(a) may be written as:

$$z = P_{11}w + P_{12}u, \quad v = P_{21}w + P_{22}u, \quad u = Kv \tag{5.3}$$

Eliminating v and u from these equations, it is obtained:

$$z = F_l(P,K)w = (P_{11} + P_{12}K(I - P_{22}K)^{-1}P_{21})w \tag{5.4}$$

which implies that the transfer function from w to z can be written as a lower LFT of P in terms of K. Similarly, $F_u(P,\Delta)$ is the transfer function resulting from wrapping (positive) feedback Δ around the upper part of P (Figure 5.1(b)).

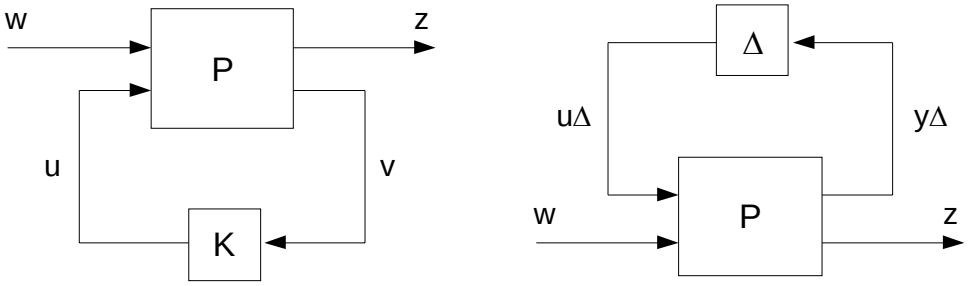

(a) (b)

Figure 5.1 Linear fractional transformation block diagrams
(a) lower LFT (b) upper LFT

H_∞ Norm: The H_∞ norm of a stable system G(s) is given as [58]:

$$\|G(s)\|_\infty = \max_\omega \bar{\sigma}(G(j\omega)) \tag{5.5}$$

here $\bar{\sigma}$ defines the largest singular value. H_∞ norm is the peak value of the Bode magnitude plot of a SISO system.

Uncertainty and Robustness: In any circumstances, the model will only be an approximate representation of the physical process. Therefore, there are unavoidable differences between the mathematical model and the real system and these are referred as model uncertainty. To account for model uncertainty it is necessary to define a set of possible models instead of a fixed model.

Main sources of uncertainty in the plant model can be listed as follows [58]:

i. There are always parameters in the model which are only known approximately or are simply in error.
ii. The parameters in the linear model may vary due to nonlinearities or changes in the operating conditions.
iii. Measurement devices have imperfections. This may even give rise to uncertainty on the manipulated inputs, since the actual input is often measured and adjusted in cascade manner.
iv. At high frequencies even the structure and the model order is unknown, and the uncertainty will always exceed 100% at some frequency.
v. Even when a very detailed model is available, for easiness in the controller design and controller implementation, a simpler (low order) system models are preferred. So the reduction in the order of the system models brings another uncertainty to a nominal system model, which must be accounted for.
vi. The controller implemented may differ from the one obtained by solving the synthesis problem. In this case uncertainty may be included to allow for controller order reduction and implementation inaccuracies.

These uncertainties could be introduced to the system with different types of uncertainty descriptions, which are presented as follows.

Parametric Uncertainty: Parametric uncertainty is due to parameter variation in the coefficients of a state-space model. Parametric uncertainty model which perturbs selected entries in the state-space data, namely in the A matrix was presented by Balas *et al* [59]. Consider a nominal state space model defined by

$$\dot{x} = Ax + Bu$$
$$y = Cx + Du \tag{5.6}$$

Assuming that the system has *n* modes and it is in bi-diagonal form, the system matrix is given by:

$$A = \begin{bmatrix} \begin{bmatrix} \alpha_1 & \beta_1 \\ -\beta_1 & \alpha_1 \end{bmatrix} & & & \\ & \begin{bmatrix} \alpha_2 & \beta_2 \\ -\beta_2 & \alpha_2 \end{bmatrix} & & \\ & & \ddots & \\ & & & \begin{bmatrix} \alpha_n & \beta_n \\ -\beta_n & \alpha_n \end{bmatrix} \end{bmatrix} \tag{5.7}$$

We would like to add uncertainty to the k[th] mode by perturbing the (1,1) element of the k[th] 2×2 block of the *A* matrix. Defining the perturbation as $\overline{\alpha}_k = (1+\delta w)\alpha_k$, where δ is a complex number with $|\delta| < 1$ and *w* is a scalar weight, the k[th] block of the *A* matrix becomes

$$\overline{A}_k = \begin{bmatrix} \alpha_k & \beta_k \\ -\beta_k & \alpha_k \end{bmatrix} + \begin{bmatrix} \delta w \alpha_k & 0 \\ 0 & 0 \end{bmatrix} = \begin{bmatrix} (1+\delta w)\alpha_k & \beta_k \\ -\beta_k & \alpha_k \end{bmatrix} \tag{5.8}$$

In order to represent the perturbation in LFT form, the disturbance, *d* (input to the system) and the error, *e* (output form the system) signals can be defined as follows:

$$e = \begin{bmatrix} 0 & 0 & \cdots & \underbrace{w\alpha_k}_{\text{k-th mode}} & 0 & \cdots & 0 & 0 \end{bmatrix}_{(1\times 2n)} \{x\}$$

$$d = \delta e \tag{5.9}$$

Then the new system with parametric uncertainty is

$$\begin{aligned} \dot{x} &= Ax + Id + Bu \\ y &= Cx + Du \\ e &= Jx \\ d &= \delta e \end{aligned} \tag{5.10}$$

where

$$J = \begin{bmatrix} 0 & 0 & \cdots & \underbrace{w\alpha_k}_{\text{k-th mode}} & 0 & \cdots & 0 & 0 \end{bmatrix}_{(1\times 2n)} \quad \text{and} \quad I = \begin{bmatrix} 0 \\ 0 \\ \vdots \\ 1 \\ 0 \\ \vdots \\ 0 \\ 0 \end{bmatrix}_{(2n\times 1)} \begin{matrix} \\ \\ \\ \} \text{ k-th mode} \\ \\ \\ \\ \\ \end{matrix}$$

A diagram of this standard framework is shown in Figure 5.2.

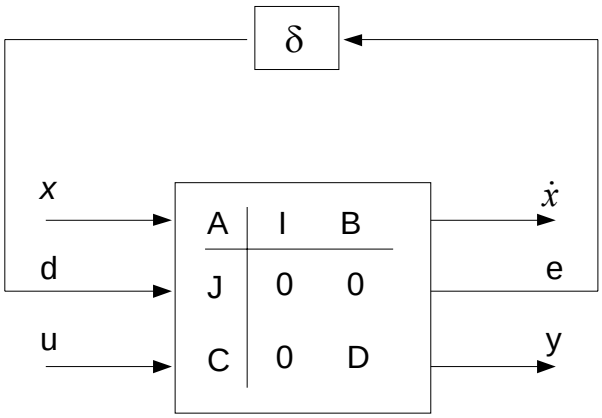

Figure 5.2 Block diagram of state-space parametric uncertainty

The uncertainty of the system is formulated in state-space form by first transforming the *A* matrix into a bidiagonal form then perturbing only first element of each 2x2 natural frequency block. This perturbation is considered as complex uncertainty, resulting in a small change in frequency and a significant change in the damping level of the mode. Thus in the controller design for flutter suppression, the migration of the pole pair toward the right half-plane as the freestream speed increases can be captured via parametric uncertainty [30].

Additive and Multiplicative Uncertainties: Additive and multiplicative uncertainties describe frequency dependent variation, via weighting functions, between the real system and the model. Block diagrams of these perturbations used to represent the model uncertainty are given in Figure 5.3. Here P is the nominal plant model, W is the weighting function which is a stable transfer function and Δ is a norm bounded complex uncertainty satisfying $\|\Delta\|_\infty < 1$.

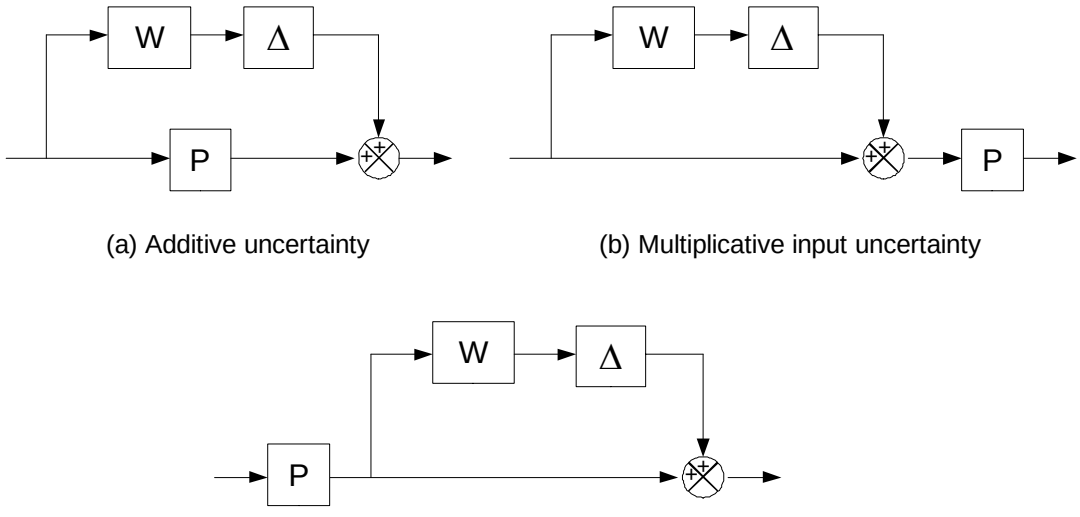

Figure 5.3 Block diagrams of additive and multiplicative uncertainties

The set of perturbed plants described by additive and multiplicative uncertainties are given by

$$\widetilde{P} = P + W\Delta \qquad \text{(Additive uncertainty)} \qquad (5.11)$$

$$\widetilde{P} = P(I + W\Delta) \qquad \text{(Multiplicative input uncertainty)} \qquad (5.12)$$

$$\widetilde{P} = (I + W\Delta)P \qquad \text{(Multiplicative output uncertainty)} \qquad (5.13)$$

In general, additive uncertainty is considered to account for unmodeled dynamics and multiplicative input/output uncertainty descriptions are used to account for relative variations in input/output signals [60].

Stability and Performance Definitions:

Nominal Stability: The nominal plant model has to be stabilized by the controller design. This is a minimum requirement.

Nominal Performance: In addition to nominal stability, the nominal closed-loop response should satisfy some performance requirements. In the synthesis problem, performance is defined in terms of the weighted H_∞ norms for the closed-loop system transfer function between the exogenous inputs (disturbances) and errors signals.

Robust Stability: The closed-loop system must remain stable for all possible plants as defined by the uncertainty descriptions.

Robust Performance: The closed-loop system must satisfy the performance requirements for all possible plants as defined by the uncertainty descriptions.

Up to now, the definitions and the necessary tools to form the H_∞ control problem were presented. Once the appropriate uncertainty descriptions and performance characteristics are chosen, the H_∞ control problem can be formed.

5.2.2 H_∞ Synthesis

The general framework for controller synthesis is shown in Figure 5.4. Interconnection of inputs, outputs and commands along with perturbations and a controller can be viewed in this diagram. *P* represents the system interconnection structure, Δ the uncertainties and *K* the control law. *w* is a vector of weighted exogenous inputs such as disturbances, noise and reference input; *z* is a vector of weighted exogenous outputs to be minimized, *v* is a vector of sensor measurements and *u* is a vector of control signals.

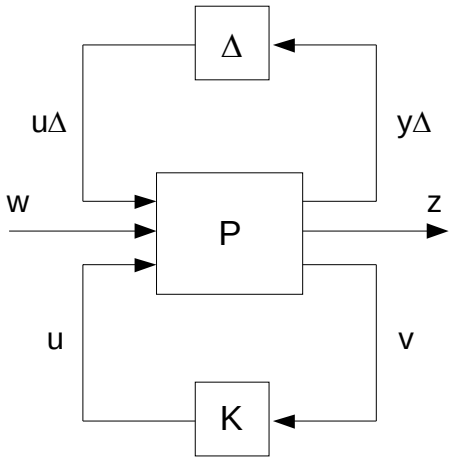

Figure 5.4 General interconnection structure

Eliminating Δ block, the standard closed-loop architecture for H_∞ synthesis is obtained, as shown in Figure 5.5. The input-output map from $[u\Delta\ w]^T$ to $[y\Delta\ z]^T$ is expressed in lower linear fractional transformation form, $F_l(P,K)$ as follows:

$$\begin{bmatrix} y\Delta \\ z \end{bmatrix} = F_l(P,K)\begin{bmatrix} u\Delta \\ w \end{bmatrix} \tag{5.14}$$

where $F_l(P,K) = (P_{11} + P_{12}K(I - P_{22}K)^{-1}P_{21})$

The plant P is partitioned according to the dimensions of the control, measurement, disturbance and error signals as

$$P = \begin{bmatrix} P_{11} & P_{12} \\ P_{21} & P_{22} \end{bmatrix} \tag{5.15}$$

The objective of the H_∞ control problem is to find a stabilizing controller K which minimizes $\|F_l(P,K)\|_\infty$ [58,61].

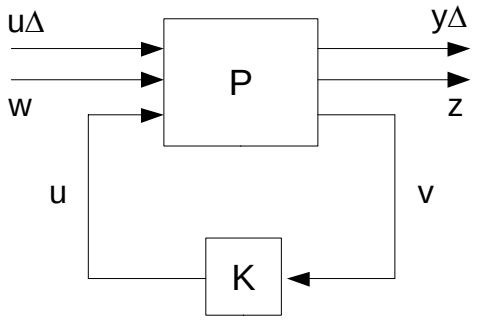

Figure 5.5 H_∞ synthesis problem

5.2.3 Structured Singular Value μ

In H_∞ controller design, the uncertainties are considered as unstructured, that is the structure of the uncertainty block Δ is not taken into account. Thus, for multiple uncertainties at different locations in the plant, an H_∞ design is too conservative which considers all the uncertainties as one full block. In order to avoid this conservatism in analyzing the stability and performance of uncertain systems, structured singular value concept was introduced [61,62].

Assuming that Δ belongs to the set of block diagonal matrices defined by

$$\underline{\Delta} = \left\{ diag(\delta_1^c I_{q1}, \ldots, \delta_n^c I_{qn}, \Delta_1, \ldots, \Delta_F) : \delta_i^c \in C, \Delta_j \in C^{m_j \times m_j} \right\} \tag{5.16}$$

This $\underline{\Delta}$ block representation involves the full blocks Δ_j, the repeated real and complex scalars δ_i^c. The repeated real scalars allow the representation of the parametric uncertainties, whereas full complex blocks allow the representation of the additive or multiplicative uncertainties.

For a given complex matrix $M \in C^{n \times n}$, the structured singular value μ is defined by

$$\mu_\Delta(M) = \frac{1}{\min\{\overline{\sigma}(\Delta) : \Delta \in \underline{\Delta}, \det(I - M\Delta) = 0\}} \tag{5.17}$$

if no $\Delta \in \underline{\Delta}$ makes $(I - M\Delta)$ singular then $\mu_\Delta = 0$.

The structured singular value μ is used for the robustness analysis of a linear system having structured uncertainty.

5.2.4 Robustness Analysis

Robust Stability: The inclusion of the controller into the plant reduces the general interconnection structure in Figure 5.4 to that in Figure 5.6, which is the general framework for system analysis.

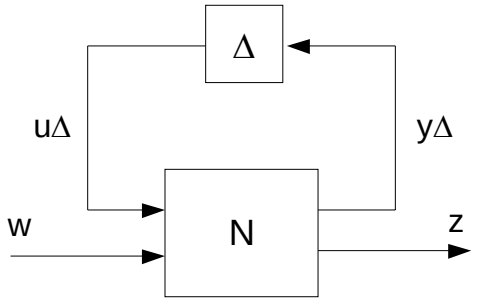

Figure 5.6 General framework for system analysis

The transfer function from *w* to *z* is given by

$$F_u(N,\Delta) = N_{22} + N_{21}\Delta(I - N_{11}\Delta)^{-1}N_{12}, \quad N = \begin{bmatrix} N_{11} & N_{12} \\ N_{21} & N_{22} \end{bmatrix} \tag{5.18}$$

$F_u(N,\Delta)$ is stable for all perturbations with $\bar{\sigma}(\Delta) \le 1$ if and only if

$$\mu_\Delta(N_{11}(j\omega)) < 1, \quad \forall \omega \tag{5.19}$$

This theorem provides a test for the stability of the system shown in Figure 5.6. Equation (5.19) reduces to $\bar{\sigma}(N_{11}(j\omega)) < 1$ when Δ is a full block, unstructured uncertainty. Hence the connection with the H_∞ norm. When Δ has structure, the H_∞ norm provides an upper bound which is a more conservative measure of robustness [60].

However, usually stability is not the only condition that must be satisfied for a feedback system. Since in most of the cases, before the onset of instability, the closed-loop performance degrades significantly when the nominal plant is perturbed. A robust performance test is necessary to indicate the worst case level of performance associated with a given level of perturbations.

Robust Performance: The robust performance problem can be formulated as a robust stability problem by defining a fictitious full block of uncertainty Δ_p with the performance inputs and outputs (Figure 5.7). Δ_p is of size number of inputs *w* by number of outputs *z*.

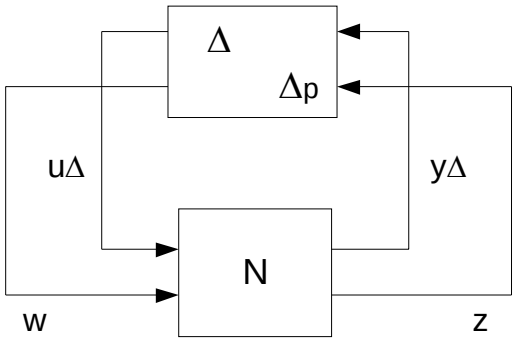

Figure 5.7 Block diagram for robust performance analysis

Theorem for the robust performance states that $F_u(N,\Delta)$ is stable and $\|F_u(N,\Delta)\|_\infty < 1$ if and only if

$$\mu_{\hat{\Delta}}(N(j\omega)) < 1, \quad \forall \omega \tag{5.21}$$

where μ is computed with respect to the structure

$$\hat{\Delta} = \begin{bmatrix} \Delta & \\ & \Delta_p \end{bmatrix} \tag{5.20}$$

This theorem implies that performance robustness of a closed-loop system can be evaluated by a μ test across all frequencies.

5.3 Control System Design

This section deals with the design of the controllers via H_∞ synthesis by using the state-space model constructed in Chapter 4, for the flutter suppression of the smart fin. In designing a control algorithm for flutter suppression, two objectives are important. The first is to extend the flutter boundary, i.e., to use feedback control to stabilize the smart fin over a larger region of operating conditions. The second is to attenuate vibrations in the operating region where the smart fin is open-loop stable.

Figure 5.8 shows the block diagram of the interconnection structure used for controller design of the smart fin. In the controller design of the smart fin, both single-input single-output (SISO) and multi-input multi-output (MIMO) system models are considered and controllers are designed based on these models.

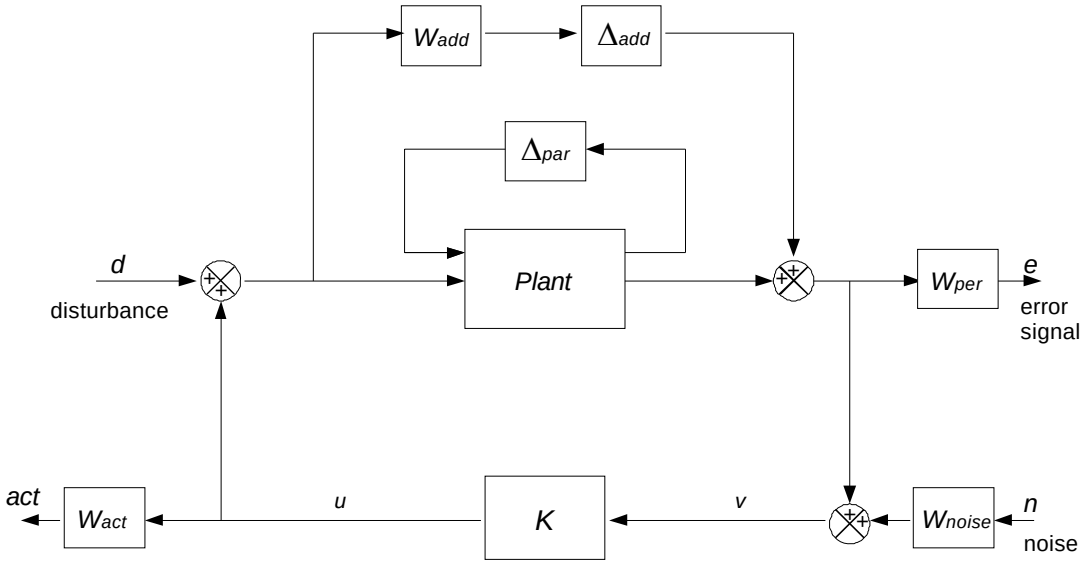

Figure 5.8 Control design block diagram for the smart fin

In Figure 5.8, *Plant* block represents the SISO or MIMO identified nominal system model. W_{per} symbolizes the performance weight applied to output channels and ask for a reduction of the maximum singular values from all inputs (disturbance, uncertainty and noise) to the outputs. Additive uncertainty weight W_{add} and the uncertainty set Δ_{add} represent additive uncertainty which is used to account for model variations in the low frequencies and unmodeled dynamics at higher frequencies. In addition to the additive uncertainty, parametric uncertainty Δ_{par} is added to the system to account for the movement of the pole of the dominant aeroelastic mode from stable to unstable as flight speed increases. Additive and parametric uncertainties provide that the closed-loop system meets the stability objectives, increasing the flutter boundary above its open-loop value while maintaining stability for lower velocities. W_{act} is the actuator weight which defines the actuator limitation. W_{noise} represents the signal to noise ratio at each sensor measurement and states that the measured system response is affected by noise.

For the controller design, performance criteria and uncertainty characteristics of the identified models and the actuator limitations are determined. Inserting the values of different weights in the general block diagram, robust H_∞ controllers are designed and open loop and closed loop frequency responses of the smart fin are analyzed. In the frequency response analysis, it is assumed that the smart fin is disturbed from its equilibrium position by the disturbance given from PZT actuators.

5.3.1 Controller Design for Single-Input Single-Output System Model

In the SISO case, the smart fin is excited by using all the PZT actuators on one face and the control input is selected as the displacement of an upper corner point at the trailing edge of the fin. The control input is designated as Sensor 1 in Figure 5.9.

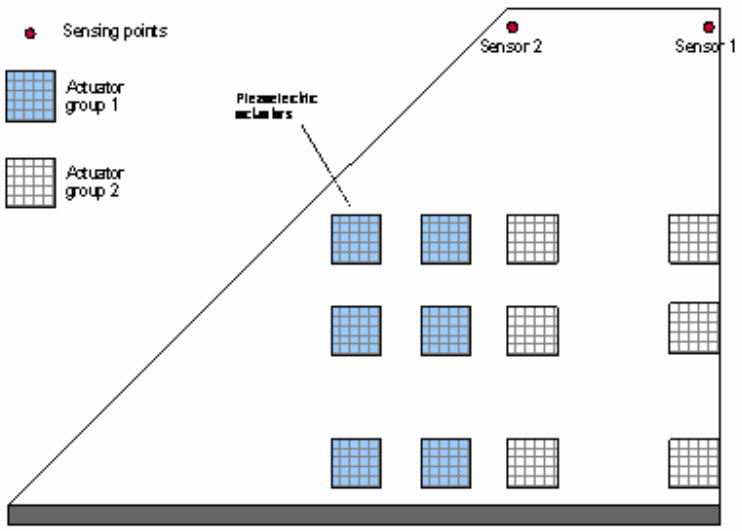

Figure 5.9 Configuration of the smart fin showing the PZT actuator groups and sensing points

The nominal plant model for the smart fin is obtained at the flight speed of 83 m/sec, which is quite close to the flutter boundary (84.1 m/sec at sea level, $\rho = 1.225$ kg/m^3) from the state-space model developed in Chapter 4. The system model has 24-states: eight states correspond to the four aeroelastic modes and sixteen states are associated with aerodynamic lag terms. For controller synthesis, the order of the nominal plant is reduced from 24-state to 8-state to keep the controller order minimum. The states in the reduced-order model correspond to the four aeroelastic modes of the smart fin. State-space equations for full and reduced order models are given in Appendix B. Figure 5.10 shows the full and reduced order system models at $V_\infty = 83$ m/sec and $\rho = 1.225$ kg/m^3. Transfer functions of the full and reduced order models at this flight condition are also given in Appendix B. From Figure 5.10, it is seen that the smart fin can be well represented by a reduced-order model. It can also be stated that the truncation of the sixteen states from the model has little effect on the dynamics of the system.

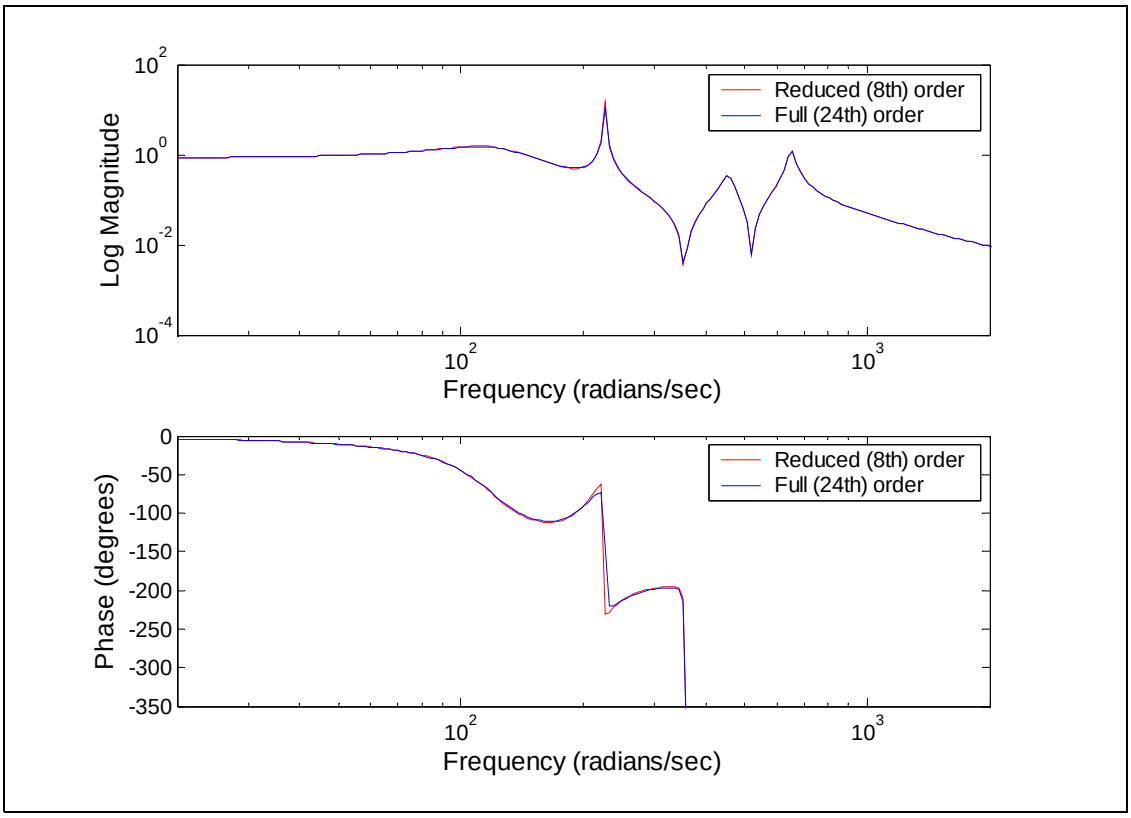

Figure 5.10 Full and reduced order models for the smart fin at $V_\infty = 83$ m/sec and $\rho = 1.225$ kg/m^3 (input: actuation of all the PZTs on one face, output: sensor 1 displacement)

The selected additive uncertainty weight W_{add} and the reduced-order plant models for the minimum (70 m/sec) and maximum (83 m/sec) speeds at which the smart fin is identified are shown in Figure 5.11. The level of the additive uncertainty at low frequencies (below the flutter frequency) is selected to cover the differences between the nominal model and the open-loop models. At high frequencies, the level of the uncertainty is selected to include the high-frequency dynamics and to induce the controller to roll off at those frequencies. Additive uncertainty also covers the uncertainty introduced by model reduction. Parametric uncertainty is added to the design model to account for the variation of the real part of a complex-conjugate pole pair at the flutter frequency (35.7 Hz). Since the damping value of the flutter mode (torsion branch)

varies significantly without the frequency change near the flutter point, the system matrix is transformed into bi-diagonal form and only the damping term is treated as the parametric uncertainty, as explained in Section 5.2.1.

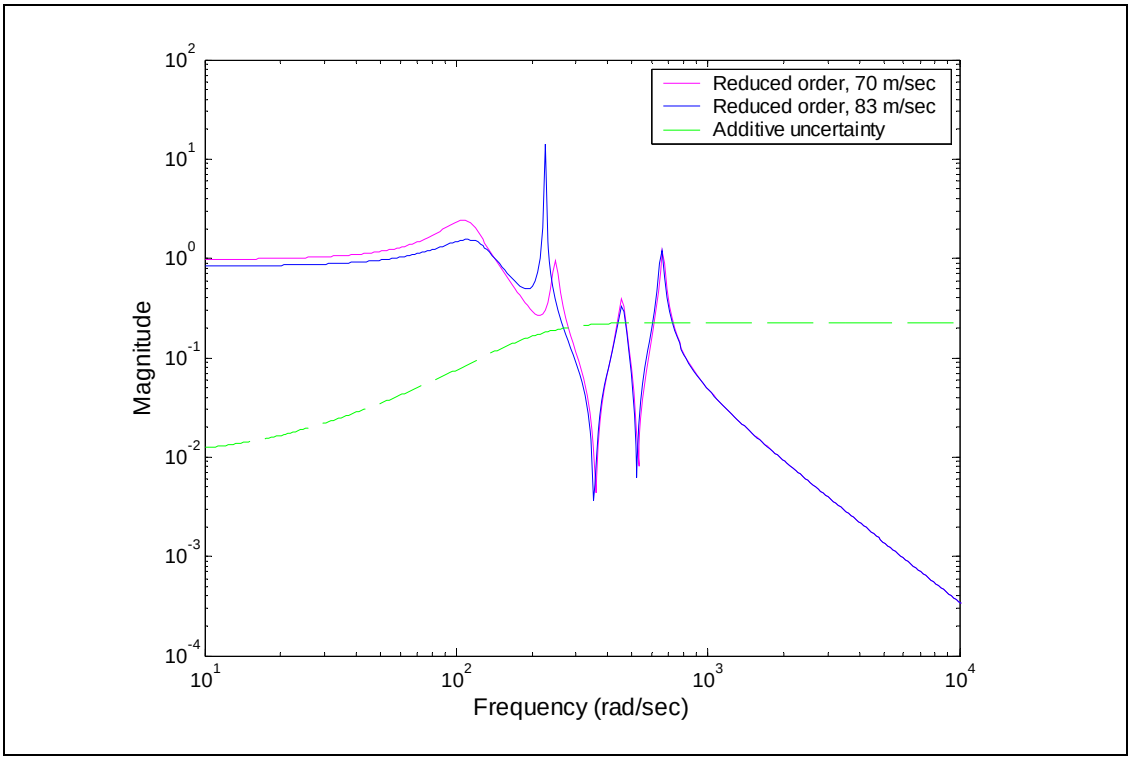

Figure 5.11 Additive uncertainty weight and the system models for the flight velocities of 70 m/sec and 83 m/sec (SISO model)

The performance objective is captured by the performance weight W_{per} shown in Figure 5.12. The chosen performance weight means that good vibration suppression is required only in low-frequency region, especially around the flutter frequency.

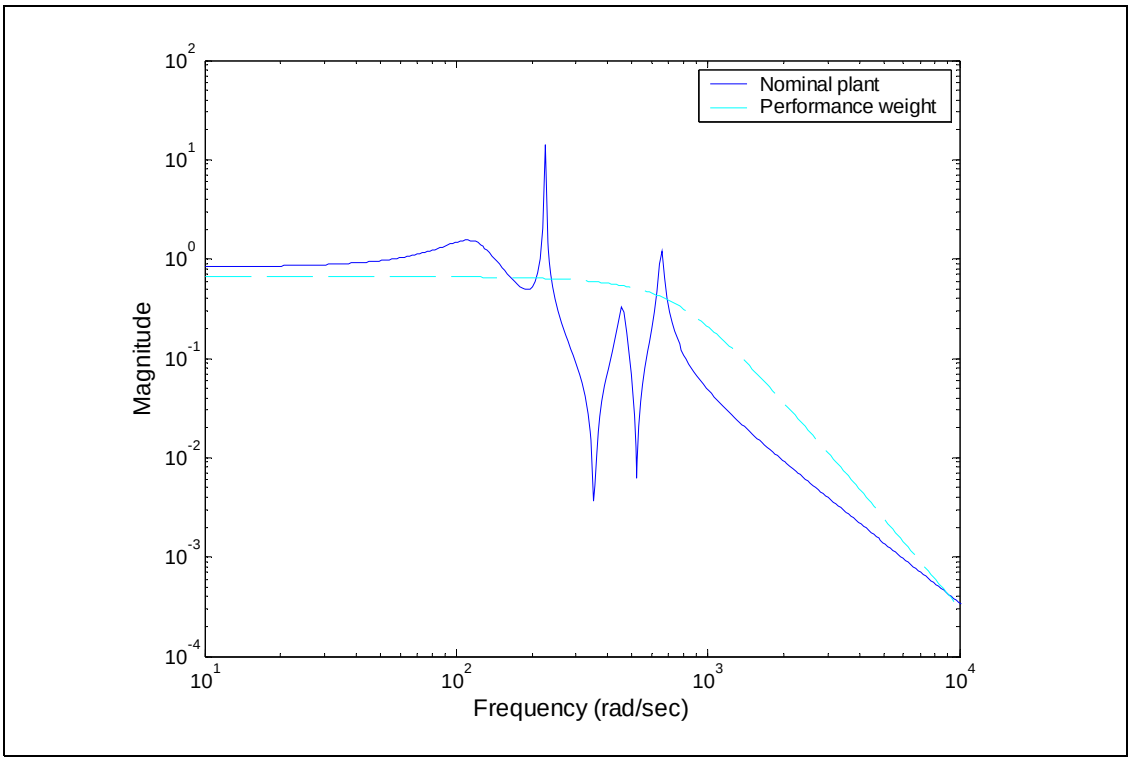

Figure 5.12 Performance weight (SISO model)

The actuator weight $W_{act} = 0.01$ is chosen to limit the voltage applied on the piezoelectric actuators. Sensor noise $W_{noise} = 0.1$ is added to the feedback signals to corrupt the measurements.

H_∞ controller is designed according to defined performance and uncertainty specifications by using MATLAB® Robust Control Toolbox [63]. Figure 5.13 gives the bode diagram of the resulting H_∞ controller.

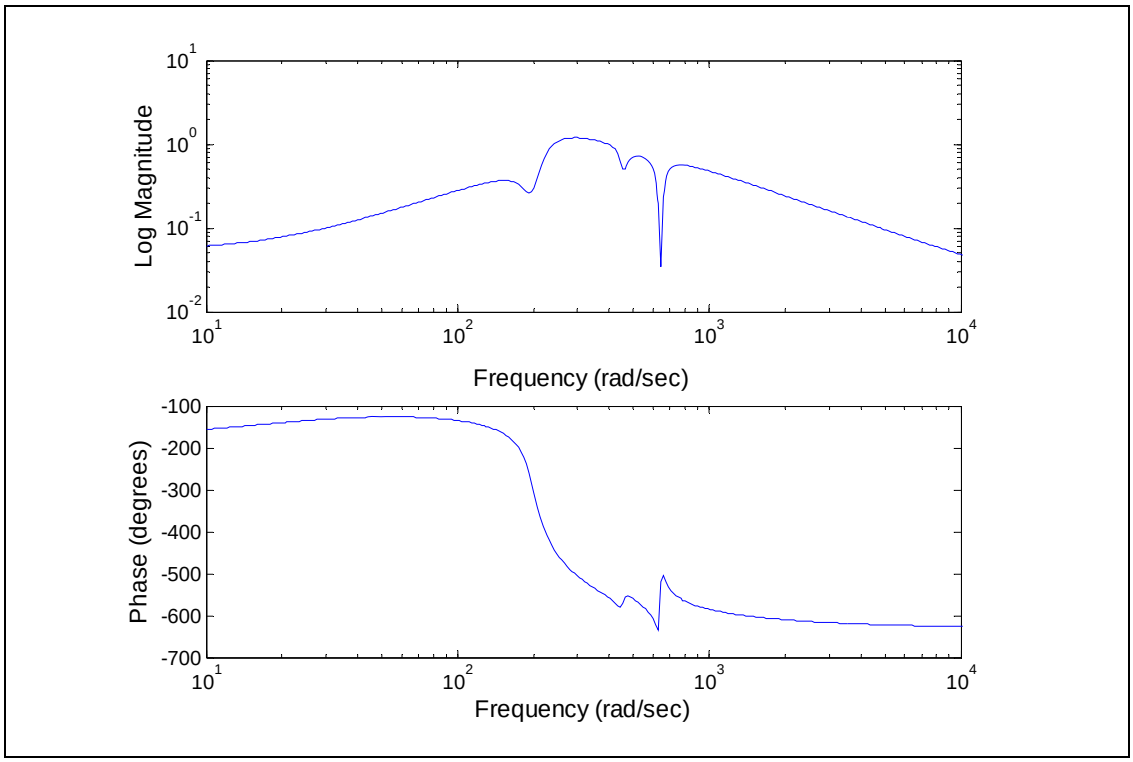

Figure 5.13 The H_∞ controller designed for the SISO model of the smart fin

μ-analysis is done for the closed-loop system to test the robustness of the H_∞ controller. The calculated structured singular values for robust performance, robust stability and nominal performance are given in Figure 5.14. μ-analysis results give the structured singular values less than unity, thereby indicating that the designed controller is admissible according to μ-analysis.

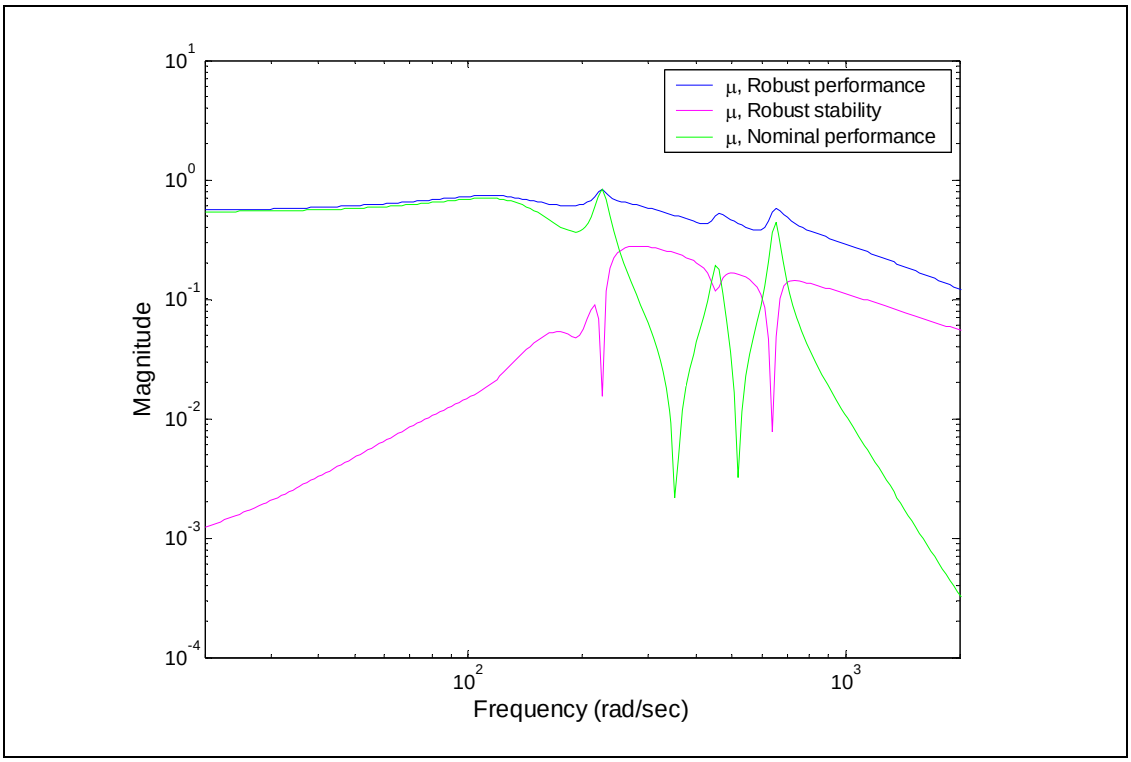

Figure 5.14 μ-analysis results of the closed-loop system for the SISO model

The controller is tested on the full-order (24th) system models for four different flow speeds of 70, 75, 80, and 83 m/sec. Figure 5.15 displays the comparison of the open-loop and closed-loop frequency responses of the smart fin. It can be seen from the figures that controller successfully suppress the vibrations at the flutter mode.

In order to determine the enhancement in flutter velocity, the root-locus of the closed-loop system is plotted for the flight velocities from 83 m/sec to 95 m/sec (Figure 5.16). It is seen that the closed-loop system becomes unstable at higher velocities. The system looses stability at a speed of 88.6 m/sec. Thus, 5.4% flutter enhancement is obtained.

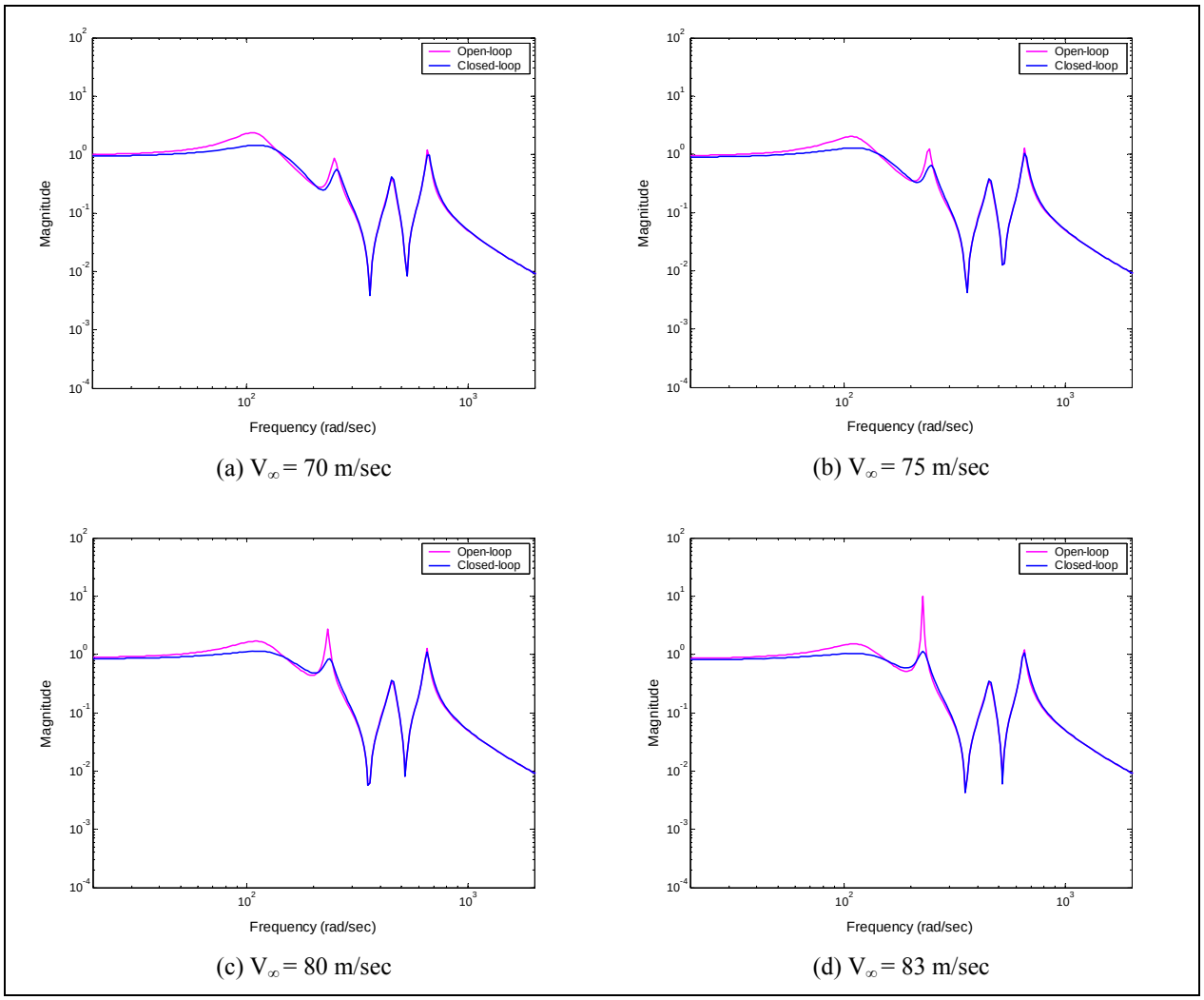

(a) $V_\infty = 70$ m/sec

(b) $V_\infty = 75$ m/sec

(c) $V_\infty = 80$ m/sec

(d) $V_\infty = 83$ m/sec

Figure 5.15 Comparison of the open-loop and closed-loop frequency responses of the smart fin for the SISO model for 70, 75, 80, and 83 m/sec

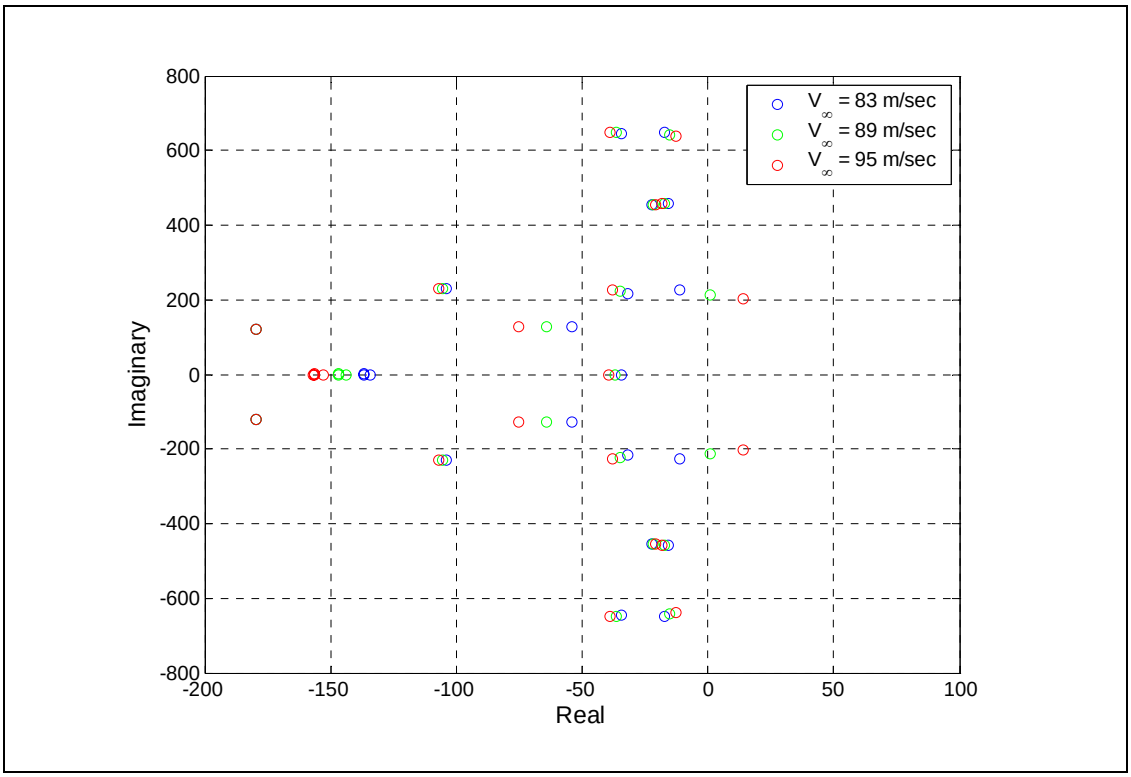

Figure 5.16 Root-locus of the closed-loop system for 83, 89 and 95 m/sec (SISO model)

5.3.2 Controller Design for Multi-Input Multi-Output System Model

In MIMO system model, PZT actuators are grouped into two actuator sets; actuator group 1 and group 2 as seen in Figure 5.9. These actuator groups are effective for torsion mode actuation of the smart fin, thus better control actuation at the flutter mode is achieved. The controller inputs are taken as the displacements of two points at the upper two corners of the smart fin given as Sensor 1 and Sensor 2 in Figure 5.9.

2-input 2-output reduced (8th) order system model at $V_\infty = 83$ m/sec and $\rho = 1.225$ kg/m^3 is used as the nominal plant. The magnitude plots of the selected additive and performance weighting functions are presented in Figure 5.17. The same scales are used

for two channels of weights W_{add} and W_{per}. In addition to the additive uncertainty, parametric uncertainty is added to the system to take into account the movement of the dominant pole as flight speed increases. Also the constant actuator weight $W_{act} = diag(0.01, 0.01)$ and noise weight $W_{noise} = diag(0.05, 0.05)$ are chosen.

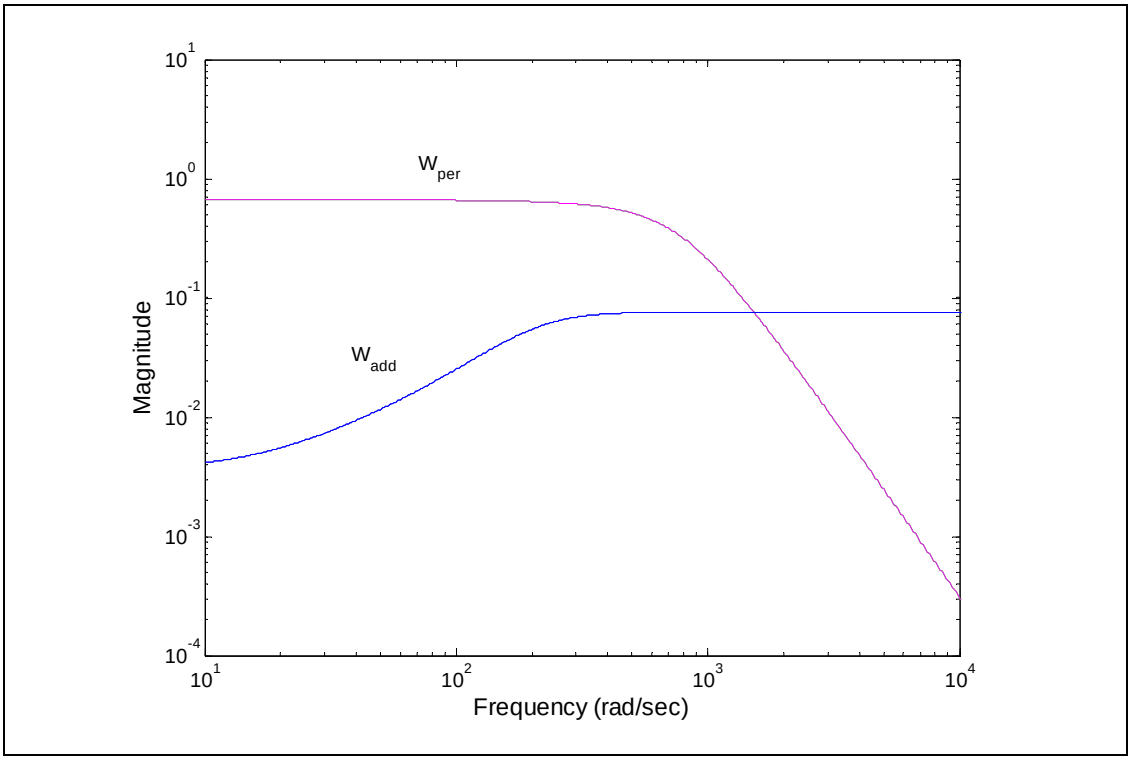

Figure 5.17 Additive and performance weights (MIMO model)

H_∞ controller is designed according to the defined performance and uncertainty specifications, and a 18th-order controller is obtained. A balanced realization of the controller is then obtained, and the 9 states are truncated from the system. The resulting 9-state controller differs in H_∞ norm from the full-order controller by less than 1%.

Figure 5.18 gives the μ bounds for robust performance, robust stability and nominal stability of the designed controller. Since the structured singular values are less than unity, the stability and the performance specifications are satisfied in the presence of the uncertainties defined.

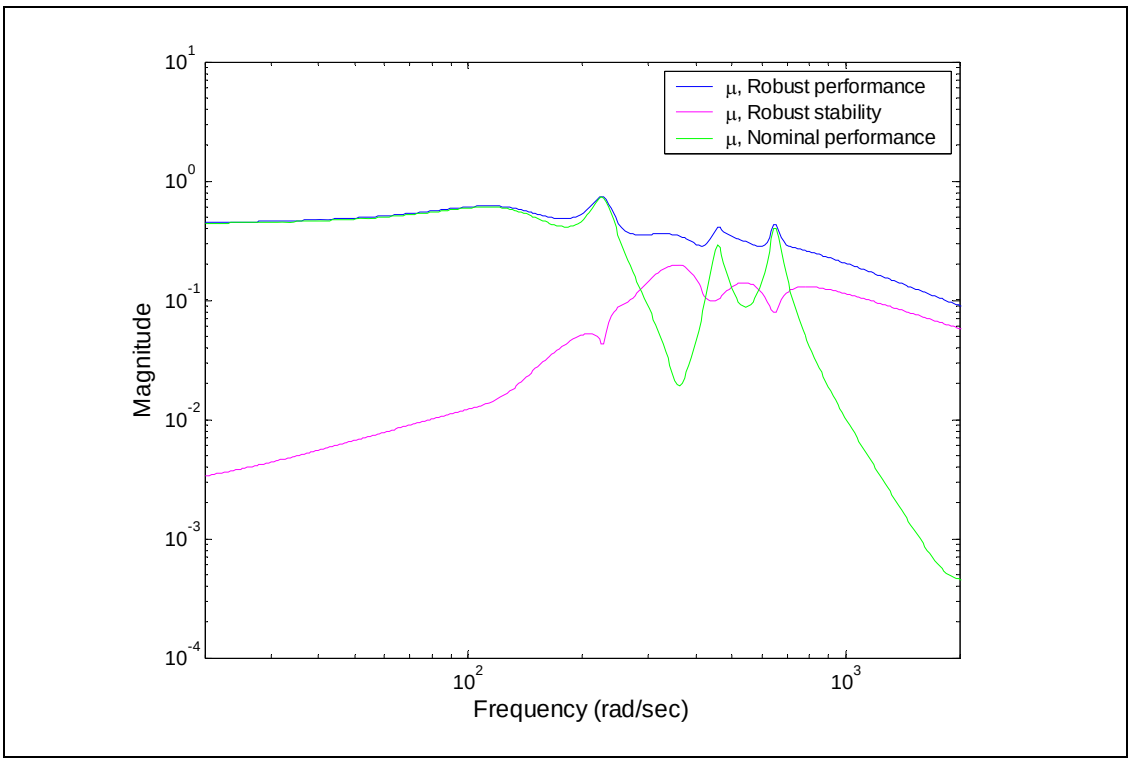

Figure 5.18 μ-analysis results of the closed-loop system for the MIMO model

The comparison of the frequency responses at the flow velocity of 83 m/sec for both uncontrolled and controlled cases is given in Figure 5.19. The controller is simulated on the full-order (24th order) system model. It can be seen that application of H_∞ controller is successful in eliminating vibrations at the first two aeroelastic modes, especially at the flutter mode. Figure 5.20 shows the open and closed-loop magnitude plots at 70 m/sec, which is quite below the flutter speed. The closed-loop system results in a successful suppression of the oscillations at a speed lower than the flutter speed, too.

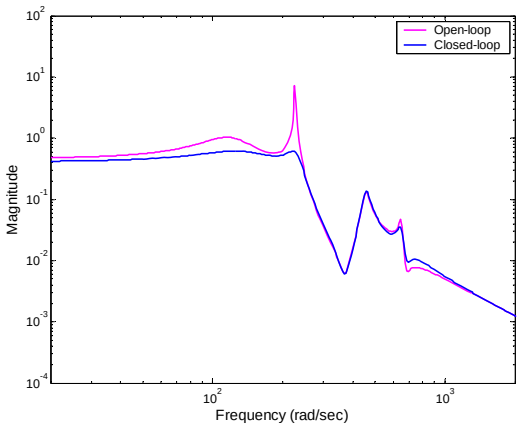

(a)

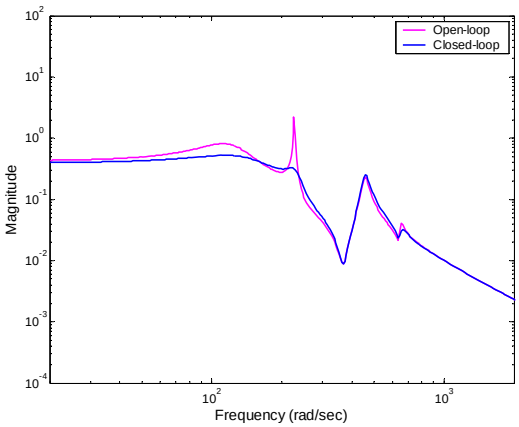

(b)

Control signal is from PZT actuator group 1

Controller input is from (a) Sensor 1 signals (b) Sensor 2 signals

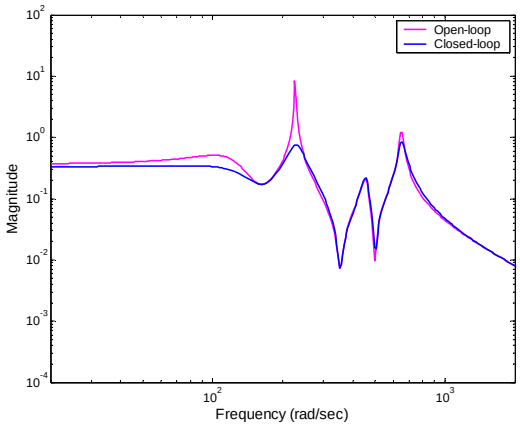

(c)

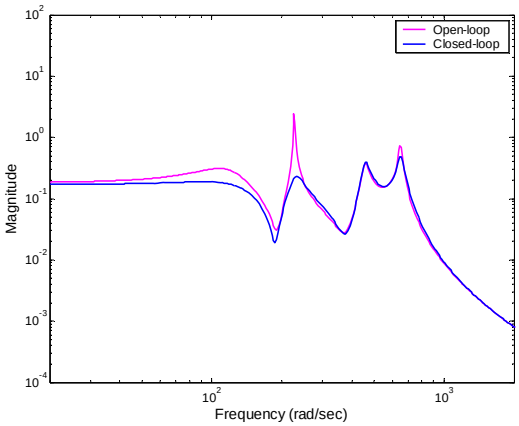

(d)

Control signal is from PZT actuator group 2

Controller input is from (c) Sensor 1 signals (d) Sensor 2 signals

Figure 5.19 Comparison of the open-loop and closed-loop frequency responses of the smart fin for the MIMO model at the flow velocity of 83 m/sec

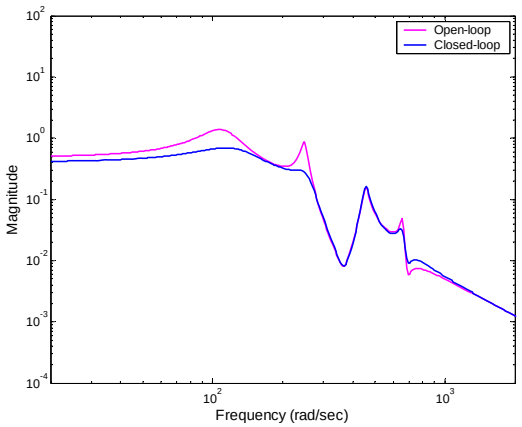

(a)

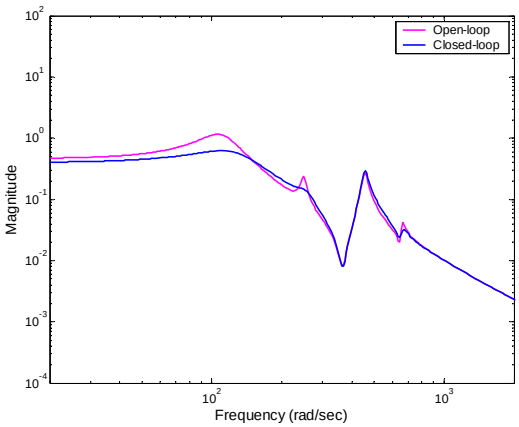

(b)

Control signal is from PZT actuator group 1

Controller input is from (a) Sensor 1 signals (b) Sensor 2 signals

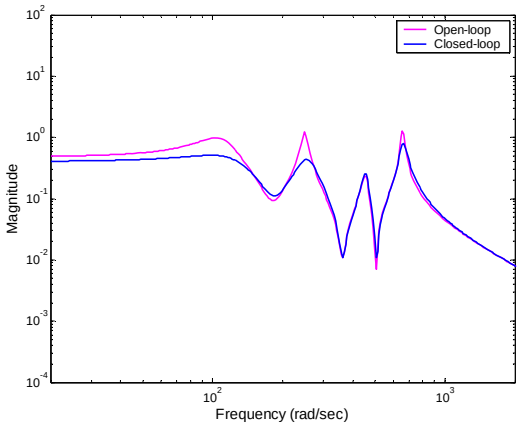

(c)

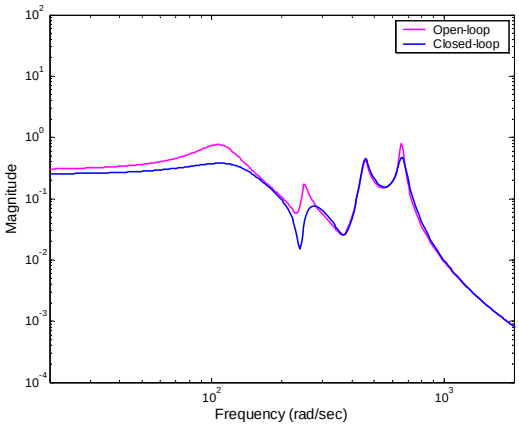

(d)

Control signal is from PZT actuator group 2

Controller input is from (c) Sensor 1 signals (d) Sensor 2 signals

Figure 5.20 Comparison of the open-loop and closed-loop frequency responses of the smart fin for the MIMO model at the flow velocity of 70 m/sec

In order to determine the enhancement in flutter velocity, the root-locus of the closed-loop system is plotted for the flight velocities from 83 m/sec to 100 m/sec. Figure 5.21 shows the root-locus plot. The closed-loop system becomes unstable at a speed of 93.7 m/sec. Thus, the flutter speed can be increased from 84.1 m/sec to 93.7 m/sec (11.4% enhancement in the flutter boundary) for the MIMO model by using H_∞ controller.

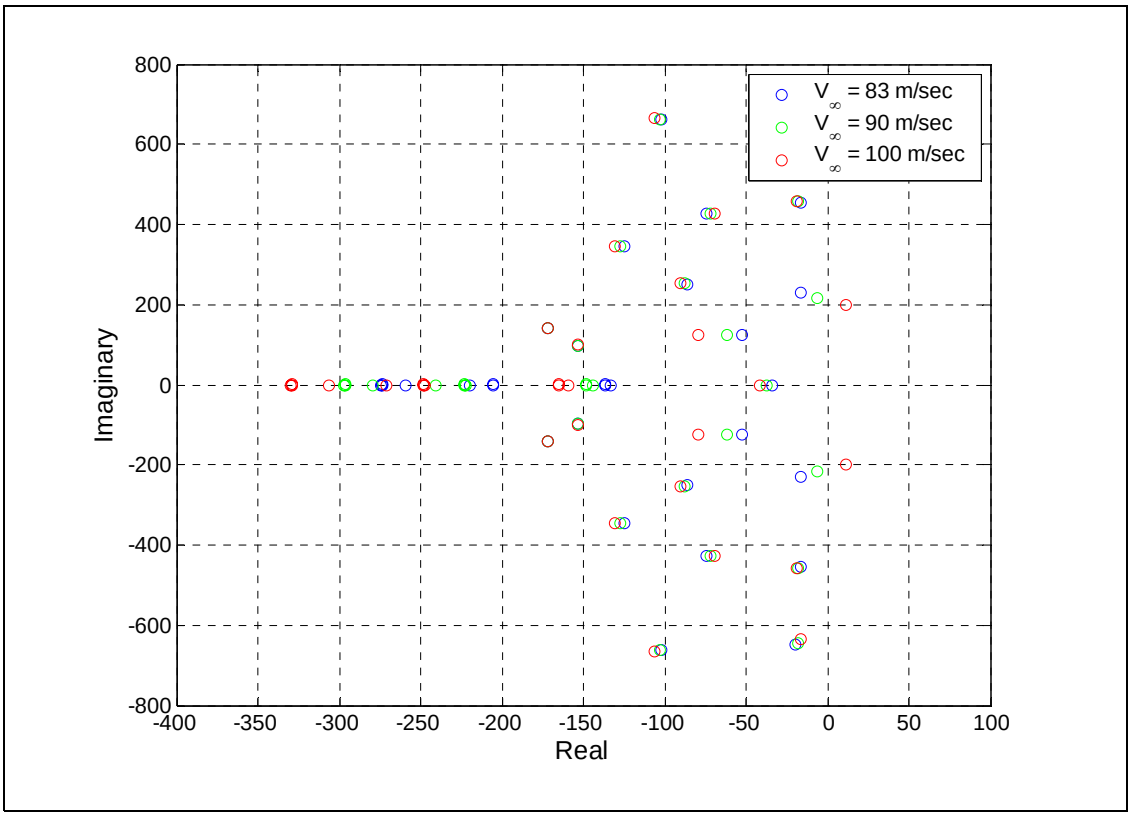

Figure 5.21 Root-locus of the closed-loop system for 83, 90 and 100 m/sec (MIMO model)

5.4 Conclusions

This chapter focused on the design of the H_∞ controllers for the flutter suppression of the smart fin based on SISO and MIMO system models.

In the controller design, the additive uncertainty was used to cover the differences between the system models in the low frequencies and unmodeled dynamics at higher frequencies. The parametric uncertainty model was used to take into account the system changes with respect to varying airspeed.

The designed H_∞ controllers showed improved behavior over a wide flow speed range. The controllers provided good suppression of the fluttering vibrations and improved the flutter speed of the fin. It was found that the flutter speed could be shifted to 88.6 m/sec for SISO model, and shifted to 93.7 m/sec for MIMO model by using the developed H_∞ controllers. The reason for the lower performance in the SISO model is due to the lack of the control force, especially in torsion direction. To give the same control signal to all of the PZTs is not very effective. In order to further enhance the control performances, more effective torsional actuation mechanisms are requested.

CHAPTER 6

CONCLUSIONS

6.1 General Conclusions

This study aimed to present a numerical approach to develop an active flutter suppression methodology for a smart fin. The smart fin was a cantilever aluminum plate-like structure with surface bonded piezoelectric (PZT, Lead- Zirconate-Titanate) patches. The surface bonded PZT patches were used as actuators.

The first part of the study was dedicated to the general structural modeling of smart structures. Different finite element based modeling techniques were presented by using MSC®/PATRAN, and the effects of different finite element types were investigated. Although the modeling of the passive portions of the smart structures by using solid elements is known to be a general approach for the simple smart structures; the difficulties in the modeling of the irregular geometries by using solid elements and the increased computational time limit their potential applications on real aerospace structures. In order to eliminate these difficulties, the techniques in which the passive portion of the smart structure was modeled by shell elements were also developed, and the effectiveness of the multipoint constraints to connect the active and passive portions of the smart structures was shown.

A thermal analogy method for the purpose of modeling of piezoelectric actuators in MSC®/NASTRAN based on the analogy between thermal strains and piezoelectric strains was given. The static and dynamic behavior of some reference models were obtained by using this thermal analogy method. The results obtained by the thermal

analogy were compared with the reference results computed by piezoelectric finite element formulation and very good agreement was observed. It is concluded that the use of the thermal analogy method to simulate the static and dynamic behavior of smart structures with piezoelectric actuators leads to promising results. This method can assist in obtaining the dynamic behavior of piezoelectric structures in the design and manufacture of smart structures, as requested for control applications, it can further reduce cost, as well as shorten design cycle time for smart structures.

The second part of the study focused on the state-space representation of the aeroelastic model of the smart fin. Approximating the unsteady aerodynamic loads in the Laplace domain as rational functions by using Roger's method, a state-space model for the smart structures was constructed for unsteady aerodynamic loading. The state-space approach was verified by performing an open loop flutter analysis of an aft-swept wing by using root-locus analysis. The flutter results were compared to those obtained by MSC®/NASTRAN *pk*-solution, and very good concurrence was observed. It can be stated that the developed state-space model can be used in modern control applications and also in obtaining the open loop flutter characteristics of an aeroelastic system.

The resulting state-space model from the Roger's aerodynamic approximation technique includes augmented states that represent the aerodynamic lags. The number of aerodynamic augmented states increase the order of the aeroelastic system, hence the order of the controller. In order to keep the controller order minimum, model reduction is needed, or instead of Roger's method, the minimum-state method which yields relatively low number of states can be used in unsteady aerodynamic approximation.

Even though the approximation of aerodynamic loads with Roger's method yields very satisfactory results for the simple structures such as the ones considered in the thesis: the aft-swept wing and the smart fin; it should be noted that in Roger's approximation, sometimes, good or even acceptable fits for unsteady aerodynamics may be difficult to obtain or, in some cases, non-existent for complex aircraft configurations and mode shapes.

In the third part of the thesis, H_∞ robust controllers were designed for the flutter suppression of the smart fin. Flutter control was performed in order to stabilize the system over a wide range of operating conditions and to attenuate disturbances throughout the operation envelope. The controllers were designed by considering both SISO and MIMO system models.

In the controller design, a parametric uncertainty model was used to characterize the system changes with respect to varying airspeed. Thus, the migration of the poles of the aeroelastic system toward the right half-plane as the freestream speed increases could be captured via parametric uncertainty. Also, the differences between the system models at low frequencies and the high-frequency unmodeled dynamics were taken into account by the additive uncertainty description.

It was shown that the designed H_∞ controllers guarantied the robust performance in the presence of uncertainties. The controllers successfully suppressed the fluttering vibrations and improved the flutter speed of the fin significantly. It was found that the closed loop system showed a transition from a stable state to unstable state beyond 88.6 m/s for SISO model (5.4 % enhancement), and 93.7 m/s for MIMO model (11.4 % enhancement). Since in the SISO case the same control signal was given to all of the PZTs, and hence no control force was generated in existed torsional direction; as expected, less performance was obtained in the SISO model.

6.2 Recommendations for Future Work

In this thesis unsteady aerodynamic loads were approximated by using Roger's approximation method. The other approximation methods such as the minimum-state or Matrix Pade method can be employed and the effectiveness of these methods can be investigated.

The locations of the piezoelectric actuators affect the overall control performance significantly. No formal optimization procedure was performed to determine the actuator locations on the smart fin for flutter suppression in the study. As a future work, the optimal pattern of the actuators can be found by using proper genetic algorithms to enhance controllability.

This thesis only numerically showed the effectiveness of the actively controlled piezoelectric actuators on the flutter suppression. The wind tunnel applications of the designed controllers may be performed for the experimental demonstrations.

REFERENCES

1. Vinson, J.R., "Plate and Panel Structures of Isotropic, Composite and Piezoelectric Materials, Including Sandwich Construction", Springer Netherlands, 2005.

2. Vincent, P., "Finite Element Modeling of Piezoelectric Active Structures", PhD Thesis, ULB, 2000.

3. Ikeda, T., "Fundamentals of Piezoelectricity", Oxford University Press, 1996.

4. Aldraihem, O.J., Wetherhold, T. and Singh, T., "Distributed Control of Laminated Beams: Timoshenko vs. Euler-Bernoulli Theory", *Journal of Intelligent Materials Systems and Structures,* Vol. 8, p: 149-157, 1997.

5. Abramovich, H., "Deflection Control of Laminated Composite Beam with Piezoceramic Layers – Closed Form Solutions", *Composite Structures,* Vol. 43, p: 217-231, 1998.

6. Fernandes, A. and Pouget, J., "Structural Response of Composite Plates Equipped with Piezoelectric Actuators", *Computers and Structures,* p: 1459-1470, 2006.

7. Sekouri, E.M., Hu, Y. and Ngo, A.D., "Modeling of a Circular Plate with Piezoelectric Actuators", *Mechatronics,* p: 1007-1020, 2004.

8. Allik, H., Webman, K.M. and Hunt, J.T., "Vibrational Response of Sonar Transducers Using Piezoelectric Transducers", *Journal of Acoustic Society of America*, Vol. 56, p: 1782-1791, 1974.

9. Varadan, V.V., Chin, L.C. and Varadan, V.K., “Finite-element Modeling of Flextensional Electroacoustic Transducers”, *Smart Materials and Structures,* Vol. 2, p: 201-207, 1993.

10. Tzou, H.S. and Tseng, C.I., “Distributed Piezoelectric Sensor/Actuator Design for Dynamic Measurement/Control of Distributed Parameter Systems: A Piezoelectric Finite Element Approach”, *Journal of Sound and Vibration*, Vol. 18, p: 17-34, 1990.

11. Ha, S.K., Keilers, C. and Chang, F.K., “Finite Element Analysis of Composite Structures Containing Distributed Piezoelectric Sensors and Actuators”, *AIAA Journal*, Vol. 30, p:772-780, 1992.

12. Lam, K.Y., Peng, X.Q., Liu, G.R. and Reddy, J.N., “A Finite-Element Model for Piezoelectric Composite Laminates”, *Smart Materials and Structures*, Vol. 6, p: 583-591, 1997.

13. Koko, T.S., Orisamolu, I.R., Smith, M.J. and Akpan, U.O., “Finite Element Based Design Tool for Smart Composite Structures”, *Proc. SPIE Conf. Smart Materials and Structures*, Vol. 3039, p: 125-134, 1997.

14. Yaman, Y., Çalışkan, T., Nalbantoğlu, V., Waechter, D. and Prasad, E., “Active Vibration Control of a Smart Beam”, *CanSmart Workshop Smart Materials and Structures*, p: 137-147, Montreal, 2001.

15. Hauch, R.M., “ABAQUS Smart Structure Modeling Methods”, AMS-TN-95-02, 1995.

16. Freed, B.D. and Babuska, V., “Finite Element Modeling of Composite Piezoelectric Structures with MSC/NASTRAN”, *SPIE 4th Annual Symposium on Smart Structures and Materials*, San Diego, 1997.

17. Dong, X.J. and Meng, G., “Dynamic Analysis of Structures with Piezoelectric Actuators Based on Thermal Analogy Method”, *International Journal of Advanced Manufacturing Technology*, Vol. 27, p: 841-844, 2006.

18. Eversman, W. and Tewari, A., “Modified Exponential Series Approximation for the Theodorsen Function”, *Journal of Aircraft*, Vol. 28, 1991.

19. Theodorsen, T., “General Theory of Aerodynamic Instability and the Mechanism of Flutter”, NACA Report 496, 1949.

20. Jones, R.T., “The Unsteady Lift of a Wing of Finite Aspect Ratio”, NACA Report 681, 1940.

21. Jones, W.P., “Aerodynamic Forces on Wings in Non-Uniform Motion”, R. & M. No. 2117, British A.R.C., 1945.

22. Watkins, C.E., Woolston, D.S. and Cunningham, H.J., “A Systematic Kernel Function Procedure for Determining Aerodynamic Forces on Oscillating or Steady Finite Wings at Subsonic Speeds”, NASA TR-48, 1959.

23. Cunningham, A.M., “Unsteady Subsonic Collocation Method for Wings with and without Control Surfaces”, *Journal of Aircraft*, Vol. 9, p: 413-419, 1972.

24. Albano, E. and Rodden, W. P., “A Doublet-Lattice Method for Calculating Lifting Disturbances on Oscillating Surfaces in Subsonic Flows”, *AIAA Journal*, Vol. 7, p: 279-285, February 1969.

25. Roger, K.L., “Airplane Math Modeling and Active Aeroelastic Control Design”, AGARD-CP-228, p: 4.1– 4.11, 1977.

26. Vepa, R., “Finite State Modeling of Aeroelastic Systems”, NASA CR-2779, 1977.

27. Karpel, M. and Tiffany, S.H., "Aeroservoelastic Modeling and Applications Using Minimum-State Approximations of the Unsteady Aerodynamics", NASA TM-101574, April 1989.

28. Waszak, M.R. and Srinathkumar, S., "Design and Experimental Validation of a Flutter Suppression Controller for the Active Flexible Wing", NASA TM-4381, 1992.

29. Mukhopadhyay, V., "Flutter Suppression Digital Control Law Design and Testing for the Active Flexible Wing Wind Tunnel Model", *AIAA Paper*, p: 156-161, 1992.

30. Vipperman, J.S., Barker, J.M., Clark, R.L., and Balas, G.J., "Comparison of μ - and H_2-Synthesis Controllers on an Experimental Typical Section", *Journal of Guidance, Control and Dynamics*, Vol. 22, p: 278-285, 1999.

31. Barker, J.M., Balas, G.J. and Blue, P.A., "Gain-Scheduled Linear Fractional Control for Active Flutter Suppression", *Journal of Guidance, Control and Dynamics*, Vol. 22, p: 507-512, 1999.

32. Lazarus, K.B., Crawley, E.F., and Lin, C.Y., "Fundamental Mechanisms of Aeroelastic Control with Control Surface and Strain Actuation", *AIAA/ASME/ASCE/AHS/ASC 32nd Structures, Structural Dynamics and Materials Conference*, p: 1817-1831, April 1991.

33. Moses, R.W., "Vertical Tail Buffeting Alleviation Using Piezoelectric Actuators-Some Results of the Actively Controlled Response of Buffet-Affected Tails (ACROBAT) Program", NASA TM-110336, 1997.

34. Moses, R.W., "Active Vertical Tail Buffeting Alleviation on an F/A-18 Model in a Wind Tunnel", *Second Joint NASA/FAA/DOD Conference on Aging Aircraft*, Williamsburg, VA, 1998.

35. Sheta, E.F., Moses, R.W. and Huttsell, L.J., "Active Smart Material Control System for Buffet Alleviation", *Journal of Sound and Vibration*, Vol. 292, p: 854-868, 2006.

36. Suleman, A., Costa, A.P., Crawford, C., and Sedaghati, R., "Wind Tunnel Aeroelastic Response of Piezoelectric and Aileron Controlled 3-D Wing" *CanSmart Workshop Smart Materials and Structures,* 1998.

37. Fazelzadeh, S.A. and Jafari S.M., "Active Control Law Design for Flutter Suppression and Gust Alleviation of a Panel with Piezoelectric Actuators", *Smart Materials and Structures,* Vol. 17, 2008.

38. Heeg, J., "Analytical and Experimental Investigation of Flutter Suppression by Piezoelectric Actuation", NASA TP 3241, 1993.

39. Döngi, F., Dinkler, D., and Kröplin, B., "Active Panel Flutter Suppression Using Self-Sensing Piezo Actuators", *AIAA Journal*, Vol. 34, p: 1224-1230, 1996.

40. Han, J.H., Tani, J., and Qiu, J., "Active Flutter Suppression of a Lifting Surface Using Piezoelectric Actuation and Modern Control Theory", *Journal of Sound and Vibration*, Vol. 291, p: 706-722, 2006.

41. Auld, B.A., "Acoustic Fields and Waves in Solids", Vol. I, Wiley, New York, 1973.

42. Bandyopadhyay, B., Manjunath, T.C., Umapathy, M., "Modeling, Control and Implementation of Smart Structures: A FEM–State Space Approach", Springer, Berlin Heidelberg, 2007.

43. Çalışkan, T., "Smart Materials and Their Applications in Aerospace Structures", PhD Thesis, Middle East Technical University, September 2002.

44. Sensor Technologies Limited, *Product Data Sheets*, 2002.

45. MSC/NASTRAN, "Quick Reference Guide", MSC.Software Corporation, 2003.

46. Kim, J., Varadan, V.V., Varadan, V.K., "Finite Element Modeling of Structures Including Piezoelectric Active Devices", *International Journal for Numerical Methods in Engineering*, Vol. 40, p: 817-832, 1997.

47. Lim, S.M., Lee, S., Park, H.C., Yoon, K.J., Goo, N.S., "Design and Demonstration of a Biomimetic Wing Section Using a Lightweight Piezo-composite Actuator (LIPCA)", *Smart Materials and Structures*, Vol. 14, p: 496-503, 2005.

48. Cote, F., Masson, P., Mrad, N., Cotoni, V., "Dynamic and Static Modeling of Piezoelectric Composite Structures Using a Thermal Analogy with MSC/NASTRAN", *Composite Structures*, p: 471-484, 2004.

49. Nam, C., Kim, Y. and Weisshaar, T.A., "Optimal Sizing and Placement of Piezo-actuators for Active Flutter Suppression", *Smart Materials and Structures*, Vol. 5, p: 216-224, 1996.

50. ZAERO, "Theoretical Manual", Version 8.0, ZONA Technology Incorporation, July 2007.

51. Karpel, M., "Design for Active Flutter Suppression and Gust Alleviation Using State-Space Aeroelastic Modeling", *Journal of Aircraft*, Vol. 19, p: 221-227, March 1982.

52. Abel, I., "An Analytical Technique for Predicting the Characteristics of a Flexible Wing Equipped with an Active Flutter Suppression System and Comparison with Wind Tunnel Data", NASA TP-1367, February 1979.

53. Rodden, W.P. and Johnson, E.H., “MSC/NASTRAN Aeroelastic Analysis User’s Guide”, V68, The MacNeal-Schwendler Corporation, 1994.

54. Dansberry, B.E., Rivera, J.A. and Farmer, M.G., “An Experimental Study of Tip Shape Effects on the Flutter of Aft-Swept, Flat-Plate Wings”, NASA TM-4180, June 1990.

55. MATLAB, “User’s Manual”, Version 6.5, The MathWorks Inc., 2003.

56. Doyle, J.C., “Lecture Notes on Advances in Multivariable Control”, *ONR/Honeywell Workshop*, Minneapolis, 1984.

57. Redheffer, R.M., “On a Certain Linear Fractional Transformation”, *J. Math and Phys.*, Vol. 39, p: 269-286, 1960.

58. Skogestad, S. and Postlethwaite, I., “Multivariable Feedback Control”, John Wiley and Sons, Inc., 1997.

59. Balas, G.J., Wolodkin, G., Nalbantoğlu, V. and Lim, K.B., “Application of Parametric Uncertainty Modeling to a Flexible Structure”, *ASME Design Engineering Technical Conferences*, California, 1997.

60. Balas, G.J., “Robust Control of Flexible Structures: Theory and Experiments”, PhD Thesis, California Institute of Technology, 1990.

61. Balas, G.J., Doyle, J.C., Glover, K., Packard, A. and Smith, R., “μ-Analysis and Synthesis Toolbox User’s Guide”, MUSYN Inc. and The MathWorks Inc., 1998.

62. Zhou, K., Doyle, J.C. and Glove, K., “Robust and Optimal Control”, Prentice Hall, New Jersey, 1996.

63. Balas, G.J., Chiang, R., Packard, A. and Safonov, M., “Robust Control Toolbox User’s Guide”, The MathWorks Inc., 2006.

APPENDIX A

ELECTROMECHANICAL AND MATERIAL PROPERTIES OF BM500 TYPE PZT PATCHES

Piezoelectric Stress Constant Matrix:

$$[e] = \begin{bmatrix} 0 & 0 & 0 & 0 & 0 & 12.3 \\ 0 & 0 & 0 & 0 & 12.3 & 0 \\ -5.4 & -5.4 & 15.1 & 0 & 0 & 0 \end{bmatrix} \text{ (Coulomb/m}^2\text{)}$$

Elastic Stiffness Coefficient Matrix:

$$[c] = \begin{bmatrix} 12.1 & 7.54 & 7.52 & 0 & 0 & 0 \\ 7.54 & 12.1 & 7.52 & 0 & 0 & 0 \\ 7.52 & 7.52 & 11.1 & 0 & 0 & 0 \\ 0 & 0 & 0 & 2.11 & 0 & 0 \\ 0 & 0 & 0 & 0 & 2.26 & 0 \\ 0 & 0 & 0 & 0 & 0 & 2.26 \end{bmatrix} \times 10^{10} \text{ (N/m}^2\text{)}$$

Density:

$\rho = 7650 \text{ kg/m}^3$

APPENDIX B

FULL AND REDUCED ORDER MODELS FOR THE SMART FIN

Full (24th) Order Model:

$$\{\dot{x}\} = [A]\{x\} + [B]\{u\}, \quad \{y\} = [C]\{x\} \tag{B.1}$$

where

$$[A] = \begin{bmatrix} [0] & [I] & [0] & [0] & [0] & [0] \\ -[\tilde{M}]^{-1}[\tilde{K}] & -[\tilde{M}]^{-1}[\tilde{D}] & q_\infty[\tilde{M}]^{-1}[A_3] & q_\infty[\tilde{M}]^{-1}[A_4] & q_\infty[\tilde{M}]^{-1}[A_5] & q_\infty[\tilde{M}]^{-1}[A_6] \\ [0] & [I] & -(\frac{2V_\infty}{b})\gamma_1[I] & [0] & [0] & [0] \\ [0] & [I] & [0] & -(\frac{2V_\infty}{b})\gamma_2[I] & [0] & [0] \\ [0] & [I] & [0] & [0] & -(\frac{2V_\infty}{b})\gamma_3[I] & [0] \\ [0] & [I] & [0] & [0] & [0] & -(\frac{2V_\infty}{b})\gamma_4[I] \end{bmatrix}_{24\times 24}$$

$$[B] = \begin{bmatrix} [0] \\ [\tilde{M}]^{-1}[\bar{F}_p] \\ [0] \\ [0] \\ [0] \\ [0] \end{bmatrix}_{24\times L}, \quad [C] = \begin{bmatrix} [\bar{C}_q] & [0] & [0] & [0] & [0] & [0] \end{bmatrix}_{R\times 24}$$

Equation B.2 gives the transfer function of the 24th order system model for $V_\infty = 83$ m/sec and $\rho = 1.225$ kg/m^3:

$$G(s) = \frac{-4.093\text{e-}012\,s^{23} + 3.455\text{e}004\,s^{22} + 9.243\text{e}007\,s^{21} + 1.294\text{e}011\,s^{20} + 1.27\text{e}014\,s^{19}}{s^{24} + 2716\,s^{23} + 4.108\text{e}006\,s^{22} + 4.506\text{e}009\,s^{21} + 3.856\text{e}012\,s^{20} + 2.663\text{e}015\,s^{19}}$$

$$\frac{+9.65\text{e}016\,s^{18} + 5.918\text{e}019\,s^{17} + 2.996\text{e}022\,s^{16} + 1.272\text{e}025\,s^{15} + 4.565\text{e}027\,s^{14}}{+1.52\text{e}018\,s^{18} + 7.267\text{e}020\,s^{17} + 2.932\text{e}023\,s^{16} + 1.002\text{e}026\,s^{15} + 2.909\text{e}028\,s^{14}}$$

$$\frac{+1.389\text{e}030\,s^{13} + 3.581\text{e}032\,s^{12} + 7.792\text{e}034\,s^{11} + 1.422\text{e}037\,s^{10} + 2.158\text{e}039\,s^{9}}{+7.196\text{e}030\,s^{13} + 1.518\text{e}033\,s^{12} + 2.722\text{e}035\,s^{11} + 4.129\text{e}037\,s^{10} + 5.26\text{e}039\,s^{9}}$$

$$\frac{+2.683\text{e}041\,s^{8} + 2.687\text{e}043\,s^{7} + 2.12\text{e}045\,s^{6} + 1.281\text{e}047\,s^{5} + 5.74\text{e}048\,s^{4}}{+5.573\text{e}041\,s^{8} + 4.847\text{e}043\,s^{7} + 3.398\text{e}045\,s^{6} + 1.871\text{e}047\,s^{5} + 7.81\text{e}048\,s^{4}}$$

$$\frac{+1.821\text{e}050\,s^{3} + 3.827\text{e}051\,s^{2} + 4.743\text{e}052\,s + 2.609\text{e}053}{+2.354\text{e}050\,s^{3} + 4.774\text{e}051\,s^{2} + 5.772\text{e}052\,s + 3.122\text{e}053} \qquad \text{(B.2)}$$

Reduced (8th) Order Model:

$$\{\dot{x}\} = [A]\{x\} + [B]\{u\}, \quad \{y\} = [C]\{x\} \qquad \text{(B.3)}$$

where

$$[A] = \begin{bmatrix} [0] & [I] \\ -[\tilde{M}]^{-1}[\tilde{K}] & -[\tilde{M}]^{-1}[\tilde{D}] \end{bmatrix}_{8\times 8}$$

$$[B] = \begin{bmatrix} [0] \\ [\tilde{M}]^{-1}[\bar{F}_p] \end{bmatrix}_{8\times L}, \quad [C] = \begin{bmatrix} [\bar{C}_q] & [0] \end{bmatrix}_{R\times 8}$$

Equation B.4 gives the transfer function of the 8th order system model for $V_\infty = 83$ m/sec and $\rho = 1.225$ kg/m^3:

$$G(s) = \frac{1.421\text{e-}013\,s^7 + 3.455\text{e}004\,s^6 + 2.549\text{e}006\,s^5 + 1.529\text{e}010\,s^4}{s^8 + 114.3\,s^7 + 6.998\text{e}005\,s^6 + 6.336\text{e}007\,s^5 + 1.312\text{e}011\,s^4} \qquad \text{(B.4)}$$

$$\frac{+ 9.719\text{e}011\,s^3 + 1.803\text{e}015\,s^2 + 8.214\text{e}016\,s + 5.413\text{e}019}{+ 8.728\text{e}012\,s^3 + 6.27\text{e}015\,s^2 + 2.951\text{e}017\,s + 6.477\text{e}019}$$